

MORPHOLOGY AND OPTICAL PROPERTIES OF ULTRATHIN TELLURIUM-DOPED
GALLIUM PHOSPHIDE NANOWIRES

MORPHOLOGY AND OPTICAL PROPERTIES OF ULTRATHIN TELLURIUM-
DOPED GALLIUM PHOSPHIDE NANOWIRES

By ETHAN DIAK, B.A.Sc.

A Thesis Submitted to the School of Graduate Studies in Partial Fulfillment of the
Requirements for the Degree of Master of Applied Science

McMaster University © Copyright by Ethan Diak June 5, 2024

McMaster University

Master of Applied Science (2024)

Hamilton, Ontario (Department of Engineering Physics)

TITLE: Morphology and Optical Properties of Ultrathin Tellurium-Doped Gallium
Phosphide Nanowires

AUTHOR: Ethan Diak, B.A.Sc. (Queen's University)

SUPERVISOR: Dr. Ray LaPierre

NUMBER OF PAGES: xv, 111

Lay Abstract

A nanowire (NW) is a tiny rod with a length on the order of one millionth of a meter and diameter on the order of one billionth of a meter. We made gallium phosphide (GaP) NWs by stacking gallium and phosphorus atoms in a column. The NWs were separated by a constant distance. In some cases, we also added beryllium and tellurium atoms to our NWs. The addition of tellurium caused our NWs to grow into extremely sharp points, which we measured with a microscope that uses electrons instead of light. The microscope images also revealed that the arrangement of the atoms in the NW changes along its length. By detecting the light emission from the NWs, it was possible to distinguish between two unique arrangements. Overall, the small dimensions of our GaP NWs make them interesting for applications that require the emission or detection of single particles of light.

Abstract

The high degree of control over the morphology and optoelectronic properties of semiconductor nanowires (NWs) makes them attractive for applications such as thermoelectrics, quantum emitters, and photodetectors. However, NW growth is still not fully understood as many parameters play a role in the determination of NW morphology and crystal structure, which in turn governs resulting optoelectronic properties. We report tellurium-doped GaP NWs with positive tapering and radii measuring as low as 5 nm grown by the self-assisted vapor–liquid–solid mechanism using selective-area molecular beam epitaxy. The occurrence of ultrathin nanoantenna showed a dependence on pattern pitch (separation between NWs) with a predominance at 600 nm pitch, and exhibited radius oscillations that correlate with polytypic zincblende (ZB)/wurtzite (WZ) segments. A growth model explains the positive tapering of the NW leading to an ultrathin tip from the suppression of surface diffusion of Ga adatoms on the NW sidewalls by Te dopant flux. The model also provides a relationship between the radius modulations and the oscillations of the droplet contact angle, predicting the quasi-periodic radius oscillations and corresponding crystal phase transitions. Photoluminescence and cathodoluminescence at 10 K reveal distinct spectra corresponding to either the ZB or WZ phase. Emission above and below ~ 2.15 eV are associated with ZB and WZ, respectively. The characteristic WZ spectrum arises from a bound exciton and its phonon replicas, consistent with published results. The origin of emission in the ZB regime is less conclusive, but may originate from the splitting of a bound exciton by the field of an axial defect. The results presented in this

thesis establish a link between NW growth, morphology, and optoelectronic properties to inform future work involving ultrathin NWs.

Acknowledgements

First of all, a big thank you is warranted to my supervisor Ray LaPierre for guiding me through my master's degree and ensuring I got to the point where I have a completed thesis in my hands. Ray has provided me with many practical learning opportunities including participation at conferences in Clermont, FR, and Atlanta, USA, which I am very grateful for. He has been wonderful to work with these past two years.

I would also like to thank other excellent researchers at McMaster. Thank you to Nebile Isik Goktas for teaching me about photoluminescence measurements. Your patience with my is greatly appreciated. Thank you to Carmen Andrei and Natalie Hamada for teaching me how to operate a transmission electron microscope. It is truly amazing to explore the world at the atomic scale. I also want to thank my fellow graduate students Amanda Thomas and Spencer McDermott who have taught me so many things about nanowires. Amanda's peculiar nanowire growths form the basis of this thesis, which deserves a significant acknowledgement.

Finally, thank you to my parents for always supporting my studies in so many ways. Thanks for always getting me more and more books to read as a kid. Thanks for the constant encouragement. Thanks as well to my brothers Callum, Avery, and Kepler. You guys can always motivate me to do anything. Lastly, thank you to Cecilia for your love and unconditional support. Thanks for always believing in me and being proud of me. I love you all.

Contents

Lay Abstract	iii
Abstract	iv
Acknowledgements	vi
List of Figures	ix
List of Tables	xii
List of Abbreviations	xiii
Declaration of Academic Achievement	xv
Chapter 1 : Introduction	1
1.1 Engineering with Semiconductor Nanowires	1
1.2 Thesis Outline	6
Chapter 2 : Nanowire Growth and Quantum Confinement	7
2.1 Theory of III-V Nanowire Growth by the Vapor-Liquid-Solid Mechanism	7
2.1.1 Growing Nanowires	8
2.1.2 Crystal Structure of III-V Nanowires	15
2.2 Chemically Defined Axial Quantum Dots in III-V Nanowires	21
2.2.1 Quantum Confinement	24
2.2.2 Nanowire Quantum Dots in Literature	26
Chapter 3 : Characterizing Nanowires	31
3.1 Structural Characterization by Electron Microscopy	31
3.1.1 Theory of Scanning Electron Microscopy	34
3.1.2 Theory of Transmission Electron Microscopy	39
3.2 Optical Characterization Techniques	45
3.2.1 Theory of Photoluminescence	46
3.2.2 Theory of Cathodoluminescence	48
3.2.3 Theory of Raman Spectroscopy	49
Chapter 4 : Experimental Methods	51
4.1 Nanowire Growth	51
4.1.1 Substrate Preparation	51
4.1.2 Growth by Molecular Beam Epitaxy	53

4.2 Structural Characterization Methods	55
4.2.1 Scanning Electron Microscopy	56
4.2.2 Transmission Electron Microscopy	56
4.3 Optical Characterization Methods	56
4.3.1 Photoluminescence	57
4.3.2 Cathodoluminescence	57
4.3.3 Raman Spectroscopy	57
Chapter 5 : Ultrathin Te-Doped GaP Nanoantenna with Crystal Phase Transitions	58
5.1 Introduction	58
5.2 Structural Characterization	60
5.3 Growth Model	65
Chapter 6 : Optical Study of Ultrathin Te-Doped GaP Nanoantenna	80
6.1 Introduction	80
6.2 Optical Characterization	81
6.3 Proposed Model	87
Chapter 7 : Conclusions	94
References	96
Appendix A: Structural Characterization Data	104

List of Figures

Figure 1.1: Images of nanowires (NWs).....	1
Figure 1.2: Engineering a nanowire single photon source.....	4
Figure 1.3: Visualization of GaP nanowires (NWs) exhibiting crystal phase transitions and strong positive tapering.	5
Figure 2.1: Overview of a process to transfer a pattern onto a substrate.....	10
Figure 2.2: Depiction of GaP nanowire vapor-liquid-solid growth by molecular beam epitaxy.....	11
Figure 2.3: Modelling the self-catalyzed vapor-liquid-solid growth of a III-V nanowire (NW).	12
Figure 2.4: Steady state droplet shape parameter ηsr as a function of the effective V/III flux ratio $F5/F3$ for a fixed nanowire radius rt expressed relative to a weighted diffusion length λ	14
Figure 2.5: Simple cubic unit cell with the (100) plane highlighted.....	16
Figure 2.6: Visualization of the wurtzite (WZ) and zincblende (ZB) crystal structures. .	17
Figure 2.7: Energy band diagram comparing the allowed energies of a free electron versus an electron in a weak periodic potential as a function of the wave vector $\mathbf{k} - \mathbf{K1}$	20
Figure 2.8: Depiction of the energy bands for a metal, a semiconductor, and an insulator.	21
Figure 2.9: Chemical versus crystal phase defined quantum dot (QD).	23
Figure 2.10: Illustration of spatial confinement leading to 2D (quantum well), 1D (quantum wire), and 0D (quantum dot) structures.....	24
Figure 2.11: Visualization of allowed transitions amongst the lowest energy quantum dot states.....	26
Figure 2.12: Measuring the interface abruptness of a GaAs/ $Al_xGa_{1-x}As$ /GaAs heterostructure in a nanowire (NW).....	27
Figure 3.1: Types of electron scattering.	33
Figure 3.2: Scanning electron microscope image of a square array of GaP nanowires....	35
Figure 3.3: Fundamental components of a scanning electron microscope.	36
Figure 3.4: Operating principle of an electromagnetic lens.....	38
Figure 3.5: Selecting the imaging mode of a transmission electron microscope.....	40
Figure 3.6: Comparison of bright field (BF) and dark field (DF) intensities for an inhomogeneous sample.	42
Figure 3.7: Visualization of the transfer function of a phase contrast transmission electron microscope image.	45
Figure 3.8: Fundamental radiative transitions in a semiconductor.	47
Figure 4.1: The electron beam lithography pattern consists of six 1 mm ² nanowire (NW) pads and a larger TEM pad.	52

Figure 5.1: Scanning electron microscope (SEM) images (2 kV, 30° tilt) of GaP nanowires.	63
Figure 5.2: Transmission electron microscope (TEM) images of GaP nanowires (NWs).	64
Figure 5.3: Radius of two NWs (NW1 and NW2) versus the length of Te-doped segments (symbols), with the polytypic ZB/WZ regions highlighted in red.	66
Figure 5.4: Mean radii R^* versus the length of Te-doped NW segment obtained from Equation 5.1 with $R^*0 = 74.2$ nm and $\varepsilon(F53 - 1) / F53 = 0.215$, corresponding to NW2 in Figure 5.3, and different R s shown in the legend.	68
Figure 5.5: Growth model results.	72
Figure 6.1: Unmodified (red) and background subtracted (blue) photoluminescence spectra	82
Figure 6.2: Background subtracted and individually normalized photoluminescence spectra (10 K) for the Be-doped (red) and Be+Te-doped (blue) GaP nanowires.	83
Figure 6.3: Spatially resolved cathodoluminescence measurements (10 K) of (a) Be+Te-doped and (b) Be-doped GaP nanowires.	85
Figure 6.4: Spatially resolved Raman data from a Be+Te-doped GaP nanowire.	86
Figure 6.5: Origin of photoluminescence (PL) peaks from wurtzite (WZ) GaP nanowires.	88
Figure 6.6: Origin of exciton peak in wurtzite (WZ) GaP.	89
Figure 6.7: Comparison of photoluminescence spectra (10 K) of undoped (blue) and Be+Te-doped (red) GaP nanowires.	90
Figure 6.8: Origin of photoluminescence (PL) peaks from zincblende (ZB) GaP nanowires.	91
Figure 6.9: Exciton binding energies for the N, O, and P peaks obtained by fitting the Arrhenius equation to temperature dependent photoluminescence data (10 K).	91
Figure 6.10: Origin of exciton peak in zincblende (ZB) GaP.	93
Figure A.1: High resolution transmission electron microscope images (300 kV) showing the transition from wurtzite (WZ) to mixed WZ/zincblende (ZB) at progressively higher magnification at positions indicated by the color-coded boxes.	105
Figure A.2: High resolution transmission electron microscope images (300 kV) showing the wurtzite (WZ) structure at the transition region at progressively higher magnification at the indicated positions.	106
Figure A.3: High resolution transmission electron microscope images (300 kV) showing the wurtzite (WZ) structure after the transition region at progressively higher magnification at the indicated positions.	107
Figure A.4: High resolution transmission electron microscope images (300 kV) showing the transition from a polytypic region (mixed wurtzite (WZ)/zincblende (ZB)) to WZ at progressively higher magnification at positions indicated by the color coded boxes.	108

Figure A.5: High resolution transmission electron microscope images (300 kV) showing the wurtzite (WZ) structure near the tip at progressively higher magnification at the indicated positions. 109
Figure A.6: Structural characterization of a nanowire (NW) tip. 110
Figure A.7: Mapping nanowire (NW) diameter oscillations. 111

List of Tables

Table 2.1: Summary of recent chemically defined axial III-V nanowire quantum dots in literature with reported interface widths.	29
Table 3.1: Experimentally measured Raman shift of characteristic phonon modes of wurtzite (WZ) and zincblende (ZB) GaP nanowires.	50
Table 4.1: Molecular beam epitaxy growth protocol of the Be+Te-doped GaP nanowire sample.	54
Table 4.2: Molecular beam epitaxy growth protocol of the Be-doped GaP nanowire sample.	55
Table 4.3: Molecular beam epitaxy growth protocol of the undoped GaP nanowire sample.	55

List of Abbreviations

ALD	Atomic Layer Deposition
BF	Bright Field
BSE	Backscattered Electron
CCD	Charge-Coupled Device
CCEM	Canadian Centre for Electron Microscopy
CL	Cathodoluminescence
CVD	Chemical Vapor Deposition
DF	Dark Field
EBL	Electron Beam Lithography
EDX	Energy Dispersive X-Ray
EELS	Electron Energy Loss Spectroscopy
FEG	Field Emission Gun
FWHM	Full Width Half Maximum
HAADF	High-Angle Annular Dark Field
HRTEM	High Resolution Transmission Electron Microscope
HVPE	Hydride Vapor Phase Epitaxy
LO	Longitudinal Optical
MBE	Molecular Beam Epitaxy
ML	Monolayer
MOCVD	Metal Organic Chemical Vapour Deposition
NW	Nanowire
NWQD	Nanowire Quantum Dot

PL	Photoluminescence
QD	Quantum Dot
RIE	Reactive Ion Etching
SAE	Selective Area Epitaxy
SE	Secondary Electron
SEM	Scanning Electron Microscope
SK	Stranski-Kastranov
SO	Surface Optical
SPS	Single Photon Source
STEM	Scanning Transmission Electron Spectroscopy
TA	Transverse Acoustical
TEM	Transmission Electron Microscope
TO	Transverse Optical
TSL	Twinning Superlattice
VLS	Vapor-Liquid-Solid
VS	Vapor-Solid
WZ	Wurtzite
ZB	Zincblende

Declaration of Academic Achievement

I, Ethan Diak, declare that this thesis titled “Interpreting the Morphology and Optical Properties of Ultrathin Tellurium-Doped Gallium Phosphide Nanowires” is my own work. All references to other works are clearly cited and contributions by others are always acknowledged. In particular:

- Amanda Thomas is acknowledged for substrate preparation and growth of the Be-doped and Be+Te-doped nanowire samples as well as scanning electron microscope imaging.
- Spencer McDermott is acknowledged for the growth of the undoped nanowire sample.
- Alex Tsukernik is acknowledged for performing electron beam lithography.
- Carmen Andrei and Natalie Hamada are acknowledged for their help with transmission electron microscope imaging.
- Chris Butcher is acknowledged for help with scanning electron microscope imaging.
- Jonas Lähnemann and Kasigo Loeto are acknowledged for cathodoluminescence measurements.
- Alain Moréac is acknowledged for Raman measurements.
- Vladimir Dubrovskii is acknowledged for the growth model in Section 5.3.

Chapter 1: Introduction

1.1 Engineering with Semiconductor Nanowires

Semiconductor nanowires (NWs) are pseudo one-dimensional crystals and exhibit physical properties that often deviate from their bulk semiconductor counterparts, which has motivated their intense study over the past couple of decades. Figure 1.1a shows a scanning electron microscope (SEM) image of an array of GaP NWs grown on a silicon substrate. Figure 1.1b shows a transmission electron microscope (TEM) image of a single GaP NW. A typical NW has a diameter on the order of 10-100 nm and a length on the order of 1-10 μm .

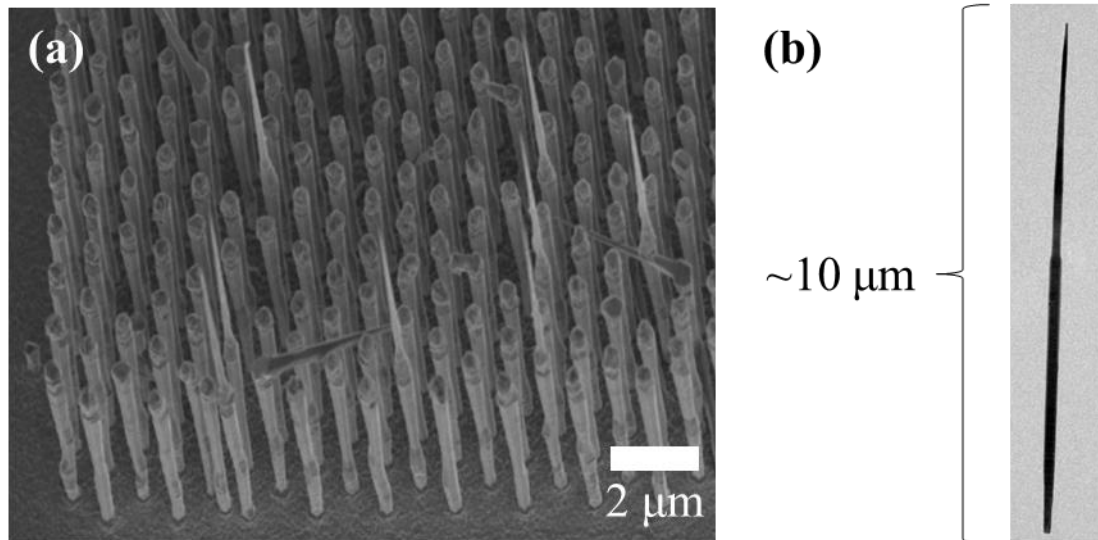


Figure 1.1: Images of nanowires (NWs). (a) Scanning electron microscope image (2 kV, 30° tilt) of an array of GaP NWs. (b) Bright field transmission electron microscope image (120 kV) of a single GaP NW.

NWs have a wide range of application areas including energy production [1], infrared imaging [2], and quantum photonics [3]. Their dimensions (length and diameter), material composition, and even crystal phase can be controlled during growth; therefore, their optoelectronic properties can be engineered for specific applications. NWs can be grown epitaxially like semiconductor thin films. Their high surface area to volume ratio allows NWs to relieve strain when lattice mismatched materials are combined [4] and enables, for example, group III-V semiconductor NWs to be grown on a silicon substrate without producing dislocations [5]. Comparatively, a thin film must be lattice-matched to its substrate to preserve crystal quality.

When it comes to engineering with NWs, an ideal process is as follows. First, required NW properties are identified for a desired application. Next, NW morphology is envisioned according to the specific properties that must be realized. Lastly, a growth recipe is devised to produce NWs with the correct morphology. The NWs are finally grown according to the recipe, ready to be tested.

While ideal steps for engineering with NWs can be simply described, there is a large amount of underlying knowledge required to link each step. A NW's morphology governs its optoelectronic properties; thus, determining a morphology to yield the desired properties requires studying a large parameter space that includes the dimensions, material composition, and crystal structure of the NW. Growing the correct morphology presents another challenge. As will be further discussed in Chapter 2, NW growth is not perfectly understood. Growth parameters such as temperature and incident material flux strongly

influence morphology; therefore, the influence of each growth parameter on the resulting NW morphology must be understood.

The previous discussion may be aided by the following example. Consider a NW single photon source (SPS), which requires a NW to emit single indistinguishable photons on-demand [3]. A candidate for a single photon emitter is a quantum dot (QD) embedded in a NW—called a nanowire quantum dot (NWQD)—shown schematically in Figure 1.2a. QD size and composition control the energy of emitted photons; thus, a relationship between the NWQD morphology and photon energy must be described, representing the required knowledge link between morphology and optoelectronic properties.

The next link to establish in the NW engineering design process is a relationship between growth and morphology. Continuing with the preceding example, a NWQD can be grown by briefly switching the material being supplied during epitaxial NW growth, forming a NWQD along the growth axis as illustrated in Figure 1.2b. Growing a NWQD with a specific morphology requires understanding how growth parameters impact the dimensions of this axial heterostructure; for example, the NWQD height depends on the growth time during which the NW material is switched and the corresponding impingement rate. In summary, designing a NW device requires an interrelated understanding of NW growth, morphology, and optoelectronic properties.

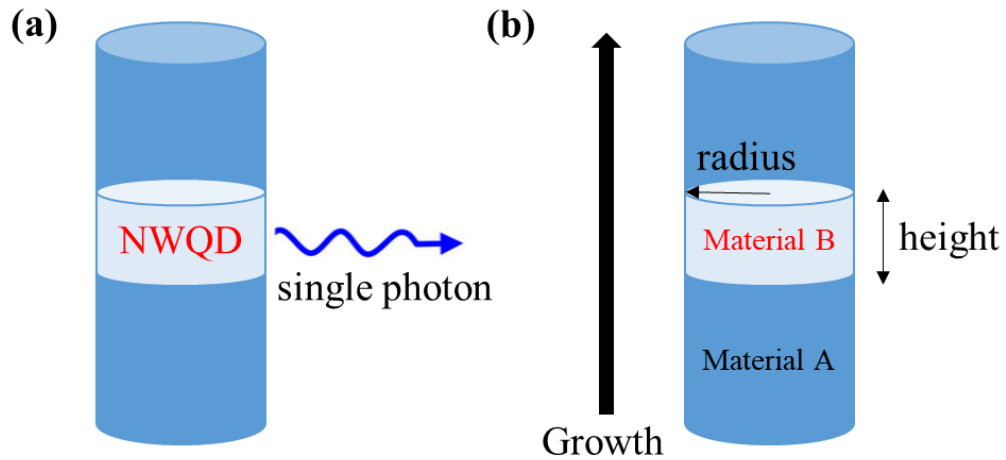


Figure 1.2: Engineering a nanowire single photon source. (a) A nanowire quantum dot (NWQD) can emit single photons. (b) A NWQD can be grown as an axial heterostructure by briefly switching from Material A to Material B.

The work presented in this thesis contributes to the present knowledge of NW growth, morphology, and optoelectronic properties through the study of GaP NWs. The GaP NWs in question were selected for study because of their unique morphology, namely, the occurrence of crystal phase transitions that coincide with strong positive tapering to radii as low as 5 nm—a record for III-V NWs grown using the vapor-liquid-solid (VLS) mechanism by molecular beam epitaxy (MBE) [6]. The positive tapering is considered to be instigated by the incorporation of a Te dopant since no positive tapering is achieved without Te-doping. Figure 1.3a represents the peculiar morphology of our NWs. A Be dopant (10^{19} cm^{-3}) is incorporated during the first growth step, yielding the NWs shown in Figure 1.3c, while the incorporation of a Te dopant ($5 \times 10^{18} \text{ cm}^{-3}$) during the second growth step results in crystal phase transitions and positive tapering, identifiable as spikes (or nanoantenna) in Figure 1.3b.

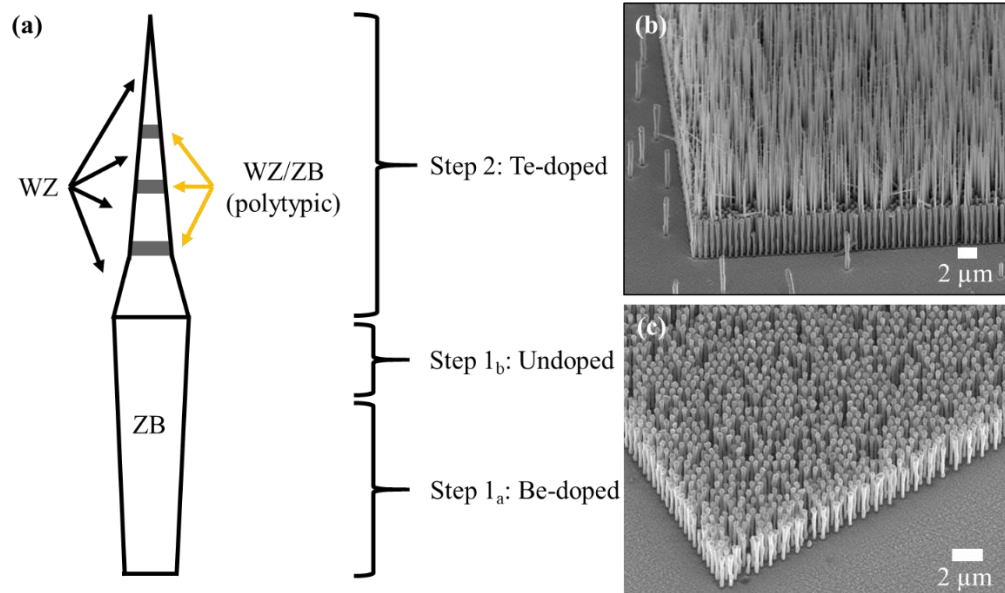


Figure 1.3: Visualization of GaP nanowires (NWs) exhibiting crystal phase transitions and strong positive tapering. (a) Schematic of a GaP NW. Only the incorporation of a Te dopant in the second growth step yields crystal phase transitions between zincblende (ZB) and wurtzite (WZ) coinciding with strong positive tapering. (b) Scanning electron microscope (2 kV, 30° tilt) image of GaP NWs with Te dopant incorporation. (c) Scanning electron microscope (2 kV, 30° tilt) image of GaP NWs without Te dopant incorporation.

The unique morphology of our NWs is attractive for quantum photonics [3] and thermoelectric [7] applications, for example, wherein ultrathin NWs are desired to leverage quantum confinement effects. Strong positive tapering coinciding with crystal phase transitions has not been previously reported for III-V NWs grown by MBE. In this thesis we explain the occurrence of our ultrathin NWs and characterize their optoelectronic properties. Therefore, this thesis serves as starting point for engineering with ultrathin NWs by addressing fundamental issues of NW growth, morphology, and optoelectronic properties.

1.2 Thesis Outline

The remainder of this thesis is divided into six chapters. In Chapter 2 we describe the epitaxial growth of NWs; in particular, we discuss VLS NW growth by MBE as it applies to the GaP NWs of interest. A brief review of existing NWQDs is also provided, motivated by possible quantum confinement applications for our ultrathin NWs. In Chapter 3 we discuss structural and optical characterization techniques. Structural characterization of our NWs is achieved using electron microscopy and so relevant theory pertaining to SEM and TEM techniques is supplied. Optical characterization of our NWs is carried out using photoluminescence (PL), cathodoluminescence (CL), and Raman techniques, which are also explained. In Chapter 4 we outline the experimental methods used to grow and characterize our NWs. The structural characterization of our NWs is used to inform a growth model in Chapter 5, which we propose to explain the unique morphology of our GaP NWs. In Chapter 6 we study the optoelectronic properties of our NWs and demonstrate distinct crystal phase dependent responses. Finally, Chapter 7 speaks to how this work can be used to inform future efforts towards engineering with ultrathin NWs.

Chapter 2: Nanowire Growth and Quantum

Confinement

2.1 Theory of III-V Nanowire Growth by the Vapor-Liquid-Solid Mechanism

III-V NWs can be fabricated using a variety of techniques. There are two classes of methods: a top-down approach and a bottom-up approach. The top-down approach involves removing material from a thin film to define NWs. This method facilitates a simple way to control NW dimensions; however, there are higher risks of surface defects owed to etching [8]. Growing a thin film also negates the advantageous strain relaxation mechanism of bottom-up NWs, which enables NW growth on a lattice mismatched substrate. Nevertheless, a top-down approach may be favoured because of its easy integration with established thin film growth techniques; for example, etched InSb NWs have been proposed for multispectral infrared imaging [9].

In contrast, bottom-up NWs are grown via an additive process such as epitaxy. One bottom-up approach known as selective area epitaxy (SAE) employs a patterned substrate mask to encourage localized vapor-solid (VS) growth at openings in the mask. NWs can form from these openings under optimized growth conditions [10]. Alternatively, NW growth can be initiated by a liquid metal catalyst droplet, typically either Au or the group III constituent of the NW (e.g. a Ga droplet is used to seed the growth of a GaP NW). Catalyzed NW

growth occurs by the VLS mechanism, which was first reported by Wagner and Ellis [11]. VLS NW growth is possible in a variety of environments such as the metal-organic vapor phase epitaxy (MOCVD) [12], hydride vapor phase epitaxy (HVPE) [13], and MBE [14] reactors. The present discussion of NW growth will be restricted to VLS growth by MBE because this is the growth mode of the GaP NWs of interest. An overview of relevant NW growth processes including some quantitative descriptions of the VLS mechanism will be provided in Section 2.1.1. The crystal structure of III-V NWs and its relation to optoelectronic properties will then be discussed in Section 2.1.2.

2.1.1 Growing Nanowires

A suitable substrate must be prepared before attempting NW growth. A Si substrate is a popular choice because it is cost-effective and facilitates NW device integration with existing Si-based electronics. Selecting the orientation of the substrate is also important. III-V NWs grow preferentially in the $\langle 111 \rangle_A$ or $\langle 111 \rangle_B$ direction [15]; thus, a Si wafer with its (111) plane exposed leads to NWs oriented vertically with respect to the substrate. While Si(111) wafers are commonly selected for NW growth it is acknowledged that the use of other substrate materials and orientations is possible [16].

After choosing a substrate, it must be processed and made ultraclean. An advantage of bottom-up growth is the ability to control the location of each NW by transferring a pattern onto the substrate, as illustrated in Figure 2.1. First, the substrate is uniformly covered by a thin (~30 nm) oxide layer (Step 1-2) using a process such as chemical vapor deposition (CVD) or atomic layer deposition (ALD). Next, a resist is spun onto the wafer (Step 2-3).

The resist is made of a material with a solubility that is altered when it is exposed to an electron beam. In this example, a positive resist is illustrated, meaning it becomes soluble to a certain solvent when exposed to an electron beam. Conversely, a negative resist is one that becomes insoluble to a certain solvent when exposed to an electron beam. The electron beam traces a predefined pattern on the wafer, illuminating only certain areas of the surface (Step 3-4). The process of defining a pattern with an electron beam is known as electron beam lithography (EBL). Since the electron beam changes the solubility of the resist, the exposed parts of the resist can then be removed with a suitable solvent (Step 4-5). Finally, the original substrate can be selectively revealed where the resist has been removed by etching the oxide with a process such as reactive ion etching (RIE) and then dissolving the excess resist (Step 5-6). In this toy example, a pattern consisting of two holes separated by a distance λ_p has been transferred onto the substrate. Holes in the oxide layer determine the locations of NWs. The size of the holes generally dictates NW diameter while the separation between holes plays a role in optoelectronic performance [17] and growth dynamics [6]. If the holes are arranged in a regular grid with a constant distance between nearest neighbours, then the NW array is said to have a constant pitch equal to the nearest neighbour spacing.

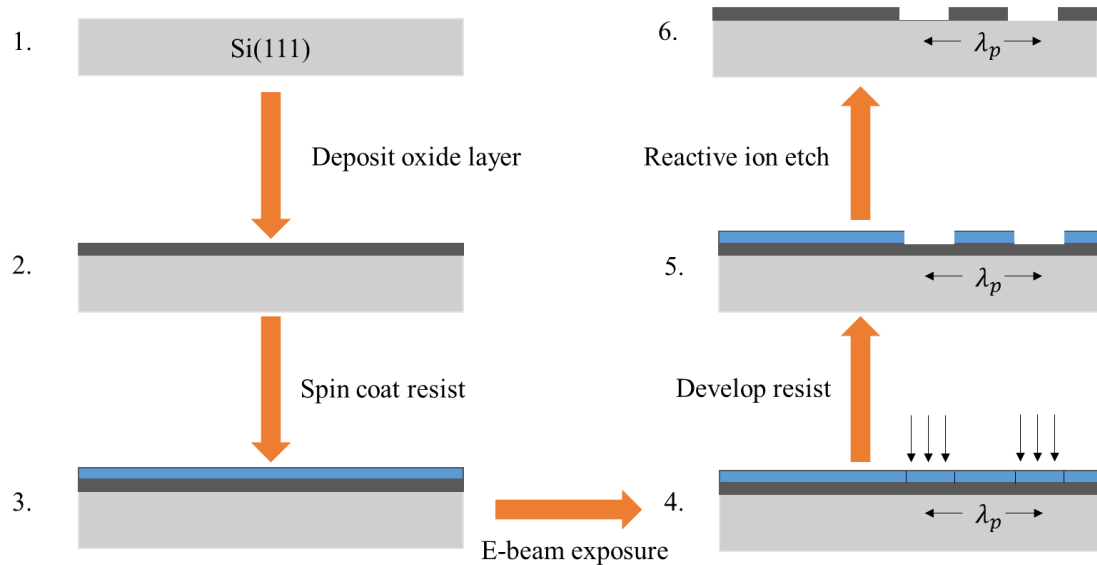


Figure 2.1: Overview of a process to transfer a pattern onto a substrate. The pattern is defined in an oxide layer using electron beam lithography and reactive ion etching and consists of two holes separated by a distance λ_p .

Once a substrate has been prepared, it can be moved into the MBE chamber in preparation for NW growth. A thin (~ 2 nm) native oxide will quickly accumulate in the holes and so an HF acid etch must be performed immediately before transferring the substrate into the MBE chamber's ultrahigh vacuum (UHV) environment. An UHV environment describes a pressure below 10^{-6} Pa, which corresponds to a mean free path around 70 km and thus ensures the free molecular flow of gasses and low levels of contamination within the chamber. By heating the substrate in the chamber it is possible to cause the desorption of lingering contaminants such as water, which will be removed over time by the reactor's vacuum pumps.

Figure 2.2 depicts the basic steps of NW VLS growth by MBE for the example case of GaP NWs. Step 1 shows the patterned substrate ready for deposition. Next, the liquid catalyst droplets are prepared by depositing Ga (Step 2). As previously mentioned, NW growth can also be seeded by Au droplets; however, there follows a risk of Au incorporation into the NW accompanied by an undesired alteration of physical properties. The Ga droplets serve as collectors of incoming material—in this case Ga and P₂ vapor fluxes as shown in Step 3. Nucleation of crystalline GaP NWs occurs at a liquid-solid interface beneath the droplet as verified by in situ observations [18], [19], [20]; hence, the droplet volume (initially determined by the hole size from the EBL pattern) correlates with the resulting NW diameter. The nucleation of a solid phase culminates the VLS process, which is driven by the difference in chemical potential between the vapor (μ_V), liquid (μ_L), and solid (μ_S) phases, namely, $\mu_V > \mu_L > \mu_S$ [21]. Vertical growth will continue as long as the droplet is intact and so the growth process is usually terminated by consuming the group III droplet with an excess group V flux. Once NW growth is complete, the substrate can be removed from the chamber and relevant device processing steps may begin.

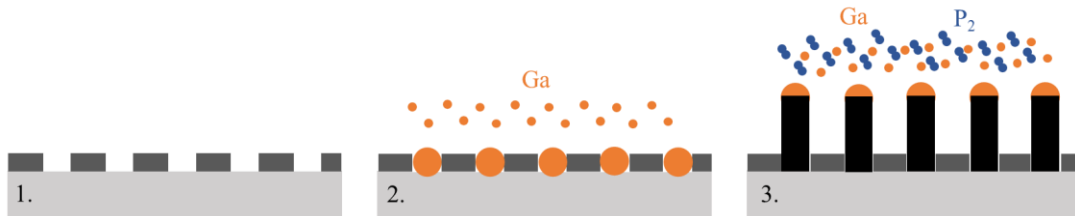


Figure 2.2: Depiction of GaP nanowire vapor-liquid-solid growth by molecular beam epitaxy. Ga droplets deposited on a patterned substrate collect incoming Ga and P₂ vapor fluxes. Supersaturation of the droplet leads to the nucleation of solid GaP nanowires.

NW growth by the VLS mechanism is not perfectly understood despite large efforts to describe the process [21]. Practical models have relied on simplifying geometries and assumptions. Tersoff [22] developed a model to predict the self-stable NW radius for a given V/III flux ratio. The model consists of the elements depicted in Figure 2.3. The NW is considered to be cylindrical with tip radius r_t and the droplet is assumed to be a truncated sphere with height h_L . In reality, III-V NWs are usually bounded by low energy (110) and (112)-type facets and exhibit a hexagonal cross-section [23]. The contact angle β is the angle the droplet makes with the NW top facet and plays a significant role in the determination of a NW's crystal phase, as will be further discussed in Section 2.1.2.

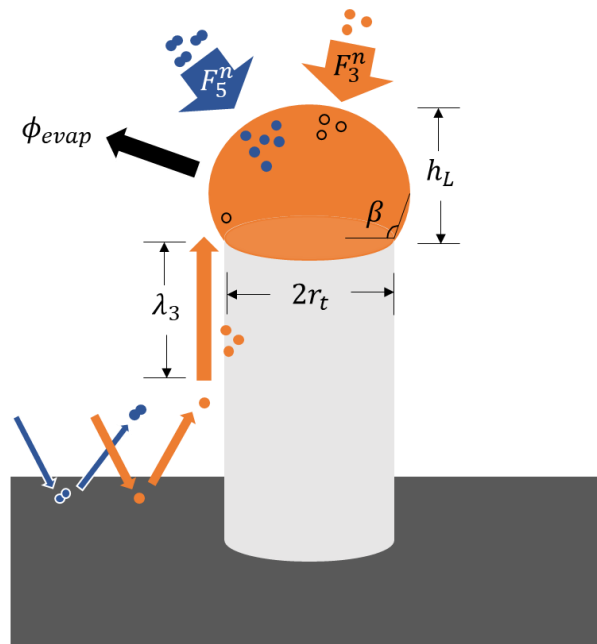


Figure 2.3: Modelling the self-catalyzed vapor-liquid-solid growth of a III-V nanowire (NW). The NW is cylindrical with tip radius r_t and the droplet is a truncated sphere with height h_L . The droplet forms an angle β with the NW top facet. Nominal group III (F_3^n) and group V (F_5^n) vapor fluxes are incorporated into the droplet through different processes. Group III adatoms can also diffuse along the NW sidewalls with a diffusion length λ_3 . The model also considers an evaporation flux ϕ_{evap} from the droplet.

During growth, the operator of the MBE reactor can choose nominal group III and group V vapor fluxes written as F_3^n and F_5^n , respectively. Ideally, the gasses incorporate perfectly into the liquid droplet, leading to nucleation along the liquid-solid interface; however, a more realistic picture considers additional processes. Tersoff accounts for the diffusion of group III adatoms along the NW sidewalls with a diffusion length λ_3 . Group V diffusion and any reactions along the sidewalls leading to sidewall growth is neglected. Group III and group V species may also reach the droplet after being re-emitted by the oxide mask. ϕ_{evap} describes the evaporation flux from the droplet. Since r_t depends on the volume of the liquid catalyst it is useful to write the time evolution of the droplet volume V_L :

$$\frac{dV_L}{dt} = 2\pi r_t \lambda_3 k_{3S} F_3^n \Omega_L + k_{3L} A_{VL} F_3^n \Omega_L - \phi_{evap} A_{VL} \Omega_L - k_{FL} A_{VL} F_5^n \Omega_L . \quad (2.1)$$

The first term of Equation 2.1 describes the increase in droplet volume due to a group III diffusion flux. k_{3S} is the sticking probability of the group III species to the NW sidewalls and Ω_L is the volume per atom in the liquid. The second term considers non-diffusive group III contributions to the droplet where k_{3L} is the sticking probability and A_{VL} is the area of the vapor-liquid interface. The third term accounts for a decrease in droplet volume due to evaporation while the last term describes the decrease in droplet volume when group V atoms incorporate into the droplet with probability k_{FL} , leading to nucleation of a solid phase. Many of these parameters are temperature dependent and thus the growth kinetics have an inherent dependence on temperature. Equation 2.1 can be re-written as

$$\frac{dV_L}{dt} = \pi r_t^2 \Omega_L [2r_t^{-1} \lambda_3 k_{3S} F_3^n + (1 + \eta^2)(F_3 - F_5)], \quad (2.2)$$

where $\eta \equiv h_L/r_t$, $F_3 \equiv k_{3L}F_3^n - \phi_{evap}$, and $F_5 \equiv k_{FL}F_5^n$. By invoking the steady-state condition $dV_L/dt = 0$, Tersoff derives an expression for the steady-state droplet shape parameter η_{sr} , namely,

$$\eta_{sr} = \left(\frac{\lambda}{r_t} \left(\frac{F_5}{F_3} - 1 \right)^{-1} - 1 \right)^{\frac{1}{2}}, \quad (2.3)$$

where $\lambda \equiv 2\lambda_3 k_{3S}/k_{3L}$. Figure 2.4 shows the dependence of η_{sr} on the effective V/III ratio for fixed values of r_t/λ . A stable droplet shape implies a stable NW diameter. At low V/III ratios the droplet exhibits unbounded growth because of the influx of group III atoms. At higher V/III ratios the droplet is consumed by the influx of group V atoms and the NW diameter tends to zero.

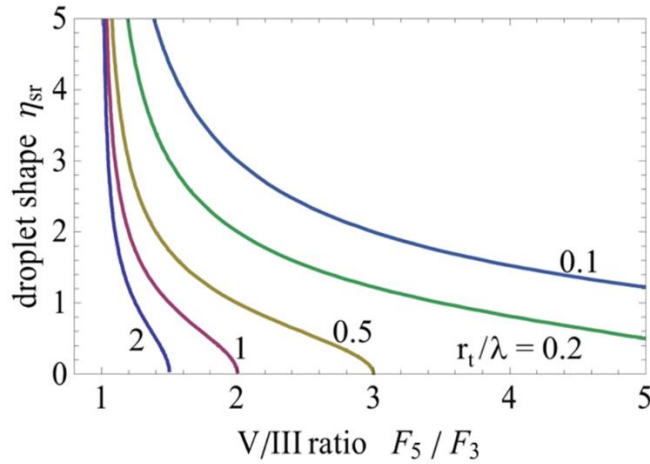


Figure 2.4: Steady state droplet shape parameter η_{sr} as a function of the effective V/III flux ratio F_5/F_3 for a fixed nanowire radius r_t expressed relative to a weighted diffusion length λ . Reprinted with permission from [22]. Copyright 2024 American Chemical Society.

From Equation 2.3, self-stable NW growth occurs for a given diameter under the flux condition

$$1 < \frac{F_5}{F_3} < 1 + \frac{\lambda}{r_t}. \quad (2.4)$$

In other words, the range of allowed V/III fluxes for stable growth is largest for narrow NWs with a long diffusion length, while wider NWs with a short diffusion length have a more restrictive set of growth conditions. This general trend is also evident in the theory presented in Chapter 5 wherein a different model for the stable NW tip radius is employed to account for the directionality of the group III and group V fluxes in an MBE reactor. The existence of different models reflects the complexity of describing the parameters governing VLS growth.

2.1.2 Crystal Structure of III-V Nanowires

An exciting possibility with NWs is the ability to engineer their crystal structure. A crystal is an ordered arrangement of atoms that can be described by the translation of a fundamental unit cell. Figure 2.5 shows the simple cubic unit cell. Because each unit cell is repeated to form a crystal it is convenient to describe crystallographic directions by leveraging the spatial periodicity and inherent symmetries of lattice planes; for example, the (100) plane, labelled in Figure 2.5, describes the family of planes with a normal vector in the $\langle 100 \rangle$ direction and a periodicity equal to the length of the unit cell. A crystal can also be described using a reciprocal space representation. The so-called reciprocal lattice comes from the Fourier transform of the crystal lattice in real space. In reciprocal space the

simple cubic cell with side length a becomes a simple cubic cell with side length $2\pi/a$; however, other types of unit cells do not generally undergo the same simple scaling when they transform into their equivalent reciprocal space representation.

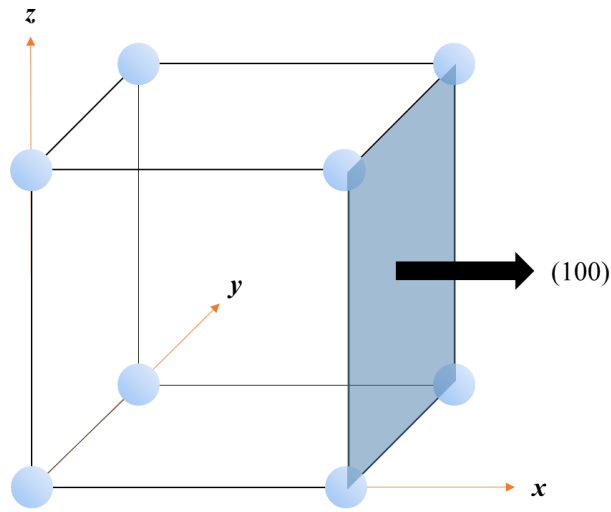


Figure 2.5: Simple cubic unit cell with the (100) plane highlighted.

III-V semiconductors adopt crystal structures that cannot be described by the simple cubic unit cell. Most bulk III-V semiconductors, including GaP, adopt the cubic ZB structure; however, III-V NWs are well known to prefer the hexagonal WZ structure under certain growth conditions. The difference between the ZB and WZ phases is visualized in Figure 2.6. When viewed along the $\langle 11\bar{2}0 \rangle$ (or equivalent) direction, the atoms in the WZ phase generate a stacking sequence with two unique layers (...ABABAB...). Comparatively, when viewed along the $\langle 1\bar{1}0 \rangle$ (or equivalent) direction, the atoms in the ZB phase generate a stacking sequence with three unique layers (...ABCABC...).

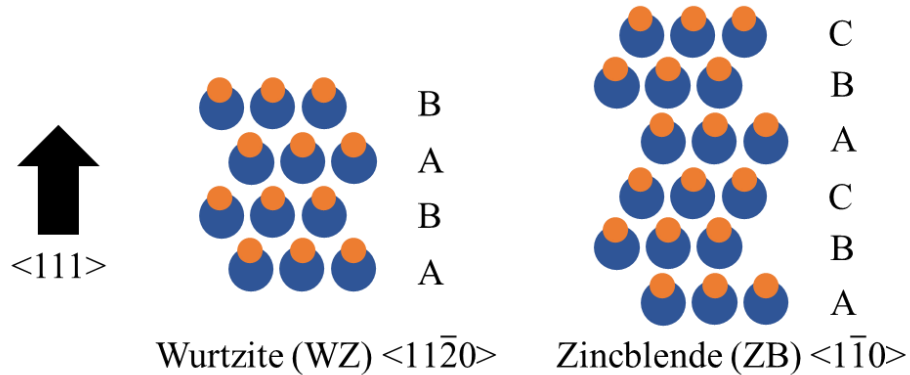


Figure 2.6: Visualization of the wurtzite (WZ) and zincblende (ZB) crystal structures. WZ exhibits a two-layer stacking sequence while ZB exhibits a three-layer stacking sequence. The orange circles represent group III atoms and the blue circles represent group V atoms.

The determination of NW crystal phase is largely controlled by the contact angle as defined in Figure 2.3, which has been explained by surface energetics [24], [25], [26]. For GaP NWs, contact angles in the range 95° - 105° yield the WZ phase, while larger contact angles favor the ZB phase [26]. In practice, precise control over the crystal phase of GaP NWs has been demonstrated by changing the growth temperature and Ga concentration of the droplet [27]. Decreasing the growth temperature and Ga concentration (higher V/III ratio) during self-catalyzed VLS growth led to crystal phase transitions from WZ to ZB.

The crystal structure determines the optoelectronic properties of a material; indeed, ZB and WZ GaP have different electronic band structures, the nature of which will be more thoroughly discussed in Chapter 6. The band structure determines the allowed energies of electron (and hole) states in a material. Its origin can be understood by considering the Schrödinger equation in reciprocal space \mathbf{k} for the case of an electron in a weak periodic potential described by Fourier components $U_{\mathbf{K}}$ for a reciprocal lattice vector \mathbf{K} [28]:

$$\left[\frac{\hbar}{2m} (\mathbf{k} - \mathbf{K})^2 - E \right] c_{\mathbf{k}-\mathbf{K}} + \sum_{\mathbf{K}'} U_{\mathbf{K}'-\mathbf{K}} c_{\mathbf{k}-\mathbf{K}'} = 0. \quad (2.5)$$

Here, \hbar is Plank's constant and m is the electron mass. The coefficients $c_{\mathbf{k}-\mathbf{K}}$ are related to the wave function $\psi_{\mathbf{k}}(\mathbf{r})$ by

$$\psi_{\mathbf{k}}(\mathbf{r}) = \sum_{\mathbf{K}} c_{\mathbf{k}-\mathbf{K}} e^{i(\mathbf{k}-\mathbf{K})\cdot\mathbf{r}}, \quad (2.6)$$

where \mathbf{r} is the real space position vector. Equation 2.5 represents a set of equations that determine the energy of the level E . In the case of a free electron there is no contribution from the periodic potential and the well-known form for the energy and wave function are obtained:

$$E = E_{\mathbf{k}-\mathbf{K}} = \frac{\hbar}{2m} (\mathbf{k} - \mathbf{K})^2, \quad \psi_{\mathbf{k}} \propto e^{i(\mathbf{k}-\mathbf{K})\cdot\mathbf{r}}. \quad (2.7)$$

When the components $U_{\mathbf{K}}$ are non-vanishing, solutions to Equation 2.5 become more complicated; however, considering the special case of two isolated electron levels yields the following system of equations:

$$\begin{aligned} (E - E_{\mathbf{k}-\mathbf{K}_1}) c_{\mathbf{k}-\mathbf{K}_1} + U_{\mathbf{K}_2-\mathbf{K}_1} c_{\mathbf{k}-\mathbf{K}_2}, \\ (E - E_{\mathbf{k}-\mathbf{K}_2}) c_{\mathbf{k}-\mathbf{K}_2} + U_{\mathbf{K}_1-\mathbf{K}_2} c_{\mathbf{k}-\mathbf{K}_1}. \end{aligned} \quad (2.8)$$

Here, \mathbf{K}_1 and \mathbf{K}_2 are two reciprocal lattice vectors of the crystal. A solution exists when

$$E = \frac{1}{2} (E_{\mathbf{k}-\mathbf{K}_1} + E_{\mathbf{k}-\mathbf{K}_2}) \pm \left[\left(\frac{1}{2} (E_{\mathbf{k}-\mathbf{K}_1} - E_{\mathbf{k}-\mathbf{K}_2}) \right)^2 + |U_{\mathbf{K}_2-\mathbf{K}_1}|^2 \right]^{\frac{1}{2}}. \quad (2.9)$$

The energy bands defined by Equation 2.9 are plotted in Figure 2.7 for the case where $\mathbf{k} - \mathbf{K}_1$ is parallel to $\mathbf{K}_2 - \mathbf{K}_1$. The allowed energies for a free electron are also shown to compare. While the energy change of a free electron is continuous along $\mathbf{k} - \mathbf{K}_1$, there is a discontinuous energy change of magnitude $2|U_{\mathbf{K}_2 - \mathbf{K}_1}|$ when an electron is subject to the weak periodic potential of the crystal. This discontinuous energy change—conventionally known as the bandgap—occurs when $\mathbf{k} - \mathbf{K}_1 = \frac{1}{2}(\mathbf{K}_2 - \mathbf{K}_1)$. Geometrically, this means the vector $\mathbf{k} - \mathbf{K}_1$ lies in a plane that bisects the vector $\mathbf{K}_2 - \mathbf{K}_1$ at a right angle. This plane is called the Bragg plane.

The bandgap is thus a fundamental consequence of the periodicity of a crystal. It defines a range of energies for which electronic states do not exist. The lower energy band is called the valence band (E_v) and the higher energy band is called the conduction band (E_c). Electrons occupying the higher energy states in the conduction band are not locally bound to individual atoms in the crystal and give rise to electrical conductivity. The probability of a state being occupied satisfies the Fermi-Dirac distribution, which depends on the Fermi-energy (E_F)—defined as the maximum energy state an electron can occupy at 0 K. At equilibrium, the Fermi-energy lies within the bandgap (Figure 2.8). This is not a problem for metals for which the free electron model applies, giving electrons easy access to the conduction band. Semiconducting and insulating materials have a finite energy bandgap and therefore do not exhibit

the same physical properties as metals. The utility of semiconductors arises from their relatively small bandgap (< 4 eV) and the ability to control electronic and optical band transitions through various optoelectronic processes.

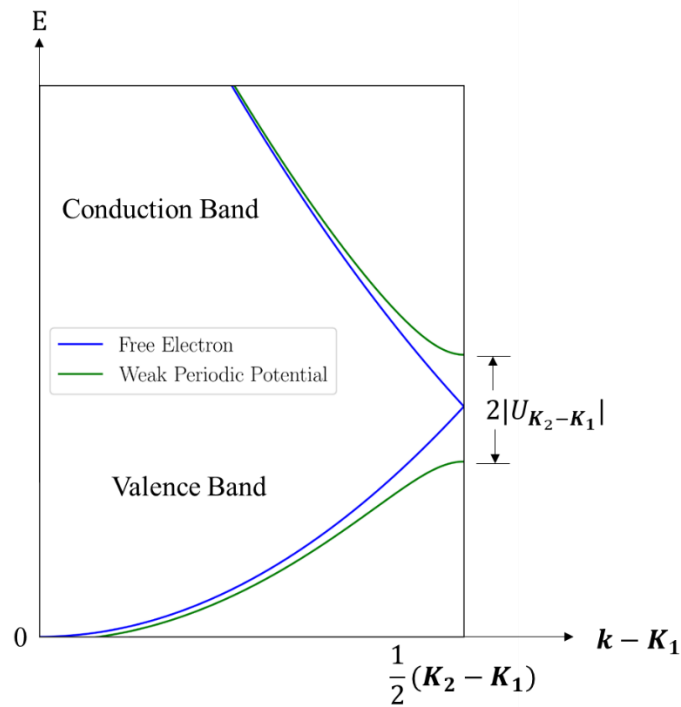


Figure 2.7: Energy band diagram comparing the allowed energies of a free electron versus an electron in a weak periodic potential as a function of the wave vector $k - K_1$. When $k - K_1 = \frac{1}{2}(K_2 - K_1)$ a bandgap of magnitude $2|U_{K_2 - K_1}|$ arises because of the periodic potential.

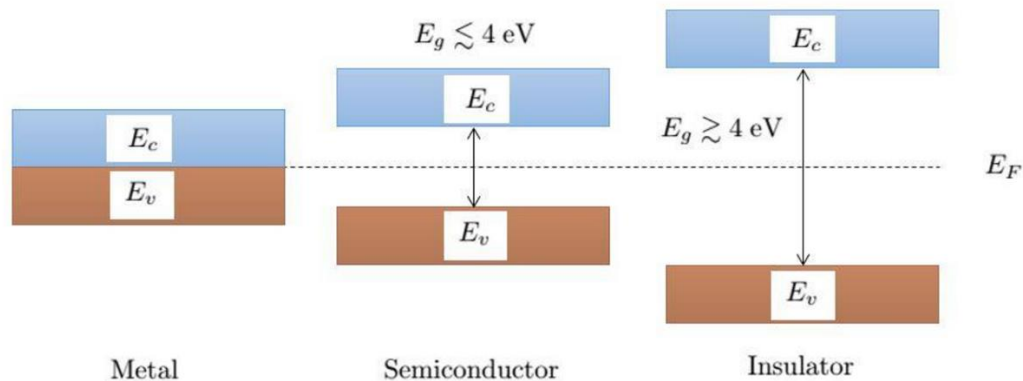


Figure 2.8: Depiction of the energy bands for a metal, a semiconductor, and an insulator. At equilibrium, the Fermi-energy (E_F) lies within the bandgap (E_g), which separates the conduction band (E_c) from the valence band (E_v).

2.2 Chemically Defined Axial Quantum Dots in III-V

Nanowires

NWs have gained attention for their role in engineering semiconductor QDs. QDs are sometimes called artificial atoms because they consist of tens of thousands of atoms, yet possess optical properties characteristic of single atoms due to the discretized energy states that arise from the quantum confinement of electrons and holes at the nanoscale. Thus, a QD facilitates the concentration of charge carriers at a particular energy—a direct consequence of its zero-dimensional density of states. The properties of QDs have been leveraged to improve the performance of solid-state devices such as light-emitting diodes [29] and photodetectors [30]. The discrete electronic spectrum of a QD also facilitates the emission and absorption of single photons. Generating and detecting single photons represents the greatest possible precision in quantum-optics experiments and has

implications for the implementation of quantum computers wherein photons act as quantum bits [31].

Classically, QDs are grown using the Stranski-Krastanov (SK) growth mode wherein three-dimensional islands randomly form to relieve excess strain during lattice-mismatched thin film growth. The islands can behave as QDs, but their precise location and morphology cannot be assured. The advent of NWs has enabled new and advantageous ways of designing QDs; in particular, we have seen that bottom-up grown NWs can be precisely positioned on a substrate by means of a patterned oxide mask. QDs embedded in NWs can thus be deterministically localized. Furthermore, control of NW morphology during growth enables tuning of the size and composition of NWQDs.

NWQDs can be defined by chemical composition or crystal phase. Chemically defined QDs involve switching the chemical composition of the NW during growth, creating a region of quantum confinement by surrounding a small bandgap material with a larger bandgap material; for example, a GaAs QD with GaP boundaries (Figure 2.9a). QDs can also be defined by changing the NW crystal phase. As discussed in Section 2.1.2, III-V NWs can adopt either the ZB or WZ crystal phase. A ZB/WZ interface forms a type II hetero-interface that can be engineered to provide quantum confinement; for instance, a WZ/ZB/WZ structure confines electrons to the ZB segment (Figure 2.9b). An advantage of crystal phase defined QDs is the ability to form atomically abrupt interfaces. That is, the switch from ZB to WZ (or vice versa) occurs across a monolayer (ML). By contrast, it is non-trivial to obtain an atomically sharp interface during the growth of a chemically defined QD since the desired supply flux of the atomic species cannot usually be instantly

generated or terminated [32]. Any compositional gradient at the interface represents an interruption to the translational symmetry of the crystal and has consequences for the electronic structure as undesired states may be introduced, skewing the ideal optoelectronic properties of a QD [33].

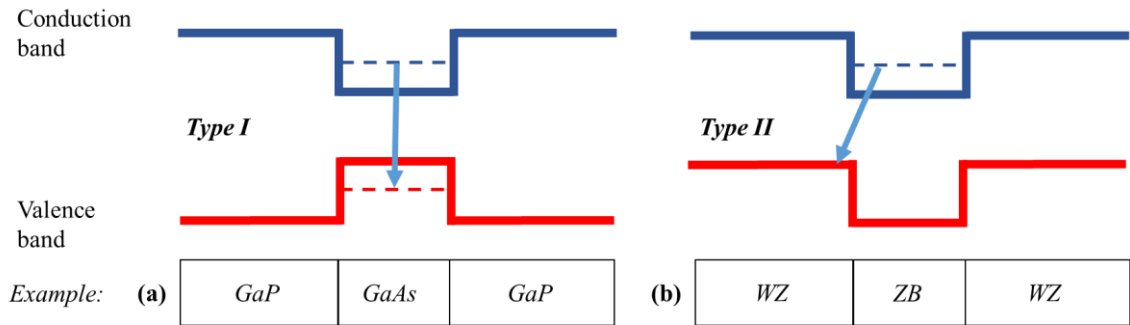


Figure 2.9: Chemical versus crystal phase defined quantum dot (QD). (a) A small bandgap material like GaAs is surrounded by a higher bandgap material like GaP, forming a chemically defined QD with type I interfaces. (b) The zincblende (ZB) crystal phase is surrounded by the wurtzite (WZ) phase, forming a crystal phase defined QD with type II interfaces. The arrows represent the recombination of an electron in the conduction band with a hole in the valence band.

NWQDs can also be further distinguished by their geometry. The concept of an axial QD was introduced in Figure 1.2; however, NWQDs can also be defined along the radial direction by initiating radial NW growth [34]. We focus our attention on axial NWQDs because the small diameter of our NWs already provides natural two-dimensional quantum confinement and we therefore believe our ultrathin NWs are of special interest for engineering axial QDs. Furthermore, we restrict our discussion to chemically defined NWQDs. While crystal phase defined QDs naturally facilitate atomically abrupt interfaces, they are limited by the band structures of the ZB and WZ phases. Meanwhile, chemically

defined QDs may be realized using a variety of III-V binaries and ternaries representing a wider range of optoelectronic properties that can be tuned to suit a desired application. Section 2.2.1 will explain the theoretical principles of quantum confinement and Section 2.2.2 will review the state-of-the-art of chemically defined axial NWQDs.

2.2.1 Quantum Confinement

Quantum confinement refers to the confinement of particles in physical space. The spatial confinement of particles modifies their density of states and results in quantization effects; in particular, classically continuous variables such as the energy of a state become discrete. Different degrees of confinement can be achieved by controlling the dimensions of nanostructures as depicted in Figure 2.10. A QD is realized when particles are confined along all three spatial dimensions, yielding a zero-dimensional density of states.

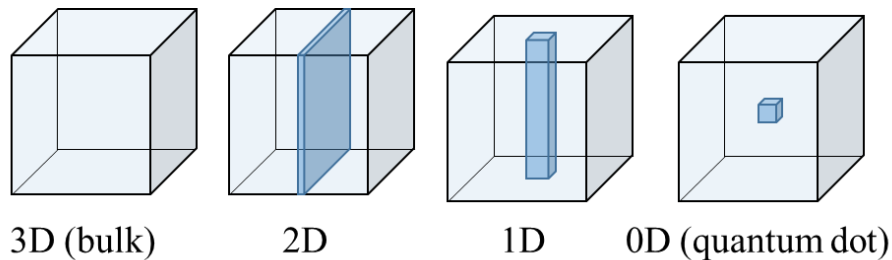


Figure 2.10: Illustration of spatial confinement leading to 2D (quantum well), 1D (quantum wire), and 0D (quantum dot) structures.

A textbook example of confinement is the problem of an electron in an infinite potential well. The electron cannot escape the well and so the electron's wave function must vanish at the boundaries, leading to the energy eigenvalues

$$E_n = \frac{\hbar^2 \pi^2 n^2}{2m_e l^2}, n \in \mathbb{Z}^+, \quad (2.10)$$

where m_e is the electron's mass and l is the length of the well. As the size of the well increases, the energy eigenvalues become more closely spaced, approaching a continuous range of allowed energies expected from classical physics. As the size of the well decreases, the allowed energies become more distant from one another, leading to a series of discrete energies. In the case of a QD, both electrons and holes are confined in space by some form of potential barrier, generating a set of electron and hole states with discrete energies. At equilibrium, the empty electron states lie in the conduction band and the empty hole states lie in the valence band. Each state can be occupied by two fermions with opposite spins due to the Pauli exclusion principle. A fundamental QD charge configuration consists of an electron-hole pair, known as an exciton. The exciton is bound by a Coulomb interaction because of the small spatial distance between the electron and hole. The preferential separation distance between the electron and hole is called the exciton Bohr radius and defines the length-scale for which significant quantum confinement effects emerge. The exciton Bohr radius is approximately 12.5 nm for GaAs [35] and 10 nm for GaP [36].

Figure 2.11 reviews allowed transitions between the lowest energy QD states. Of particular interest are radiative transitions, namely, the combination of an electron-hole pair resulting in the emission of a polarized photon. Non-radiative transitions do not lead to photon emission and cause reduced device efficiency. Ideally, the energy of the emitted photon suffers from few broadening effects [37], leading to a measured spectral linewidth on the

order of 1 meV or less. Each radiative transition has a distinct energy thanks to quantization effects; therefore, a radiative transition from a certain state can be obtained via spectral filtering, yielding an effective SPS.

Quasiparticle/ state name	Charge config.	Quantum state	Spin state	Linear transitions	Circ. trans. flip	Spin flip	Non- rad.
Biexciton		$ XX\rangle$	$ \downarrow\uparrow\downarrow\uparrow\rangle$				
Negative trion		$ X^- \rangle$	$ u_h\rangle \alpha_h\rangle \otimes \frac{1}{\sqrt{2}}(\uparrow\downarrow\rangle - \downarrow\uparrow\rangle)$				
Positive trion		$ X^+ \rangle$	$\frac{1}{\sqrt{2}}(\uparrow\downarrow\rangle - \downarrow\uparrow\rangle) \otimes u_c\rangle \alpha_c\rangle$	HV			
Exciton		$ Y_b\rangle$	$\frac{1}{\sqrt{2}}(\uparrow\downarrow\rangle + \downarrow\uparrow\rangle)$				
		$ X_b\rangle$	$\frac{1}{\sqrt{2}}(\uparrow\downarrow\rangle - \downarrow\uparrow\rangle)$				
		$ Y_d\rangle$	$\frac{1}{\sqrt{2}}(\uparrow\uparrow\rangle + \downarrow\downarrow\rangle)$				
		$ X_d\rangle$	$\frac{1}{\sqrt{2}}(\uparrow\uparrow\rangle - \downarrow\downarrow\rangle)$	HV			
Electron		$ g^- \rangle$	$ u_c\rangle \alpha_c\rangle$				
Hole		$ g^+ \rangle$	$ u_h\rangle \alpha_h\rangle$				
Ground state		$ g\rangle$					

Figure 2.11: Visualization of allowed transitions amongst the lowest energy quantum dot states. The blue (red) circles represent electrons (holes) in the lowest energy level of the conduction (valence) band. The biexciton, trion, and exciton states can support radiative recombination leading to the emission of a horizontally (H), vertically (V), or circularly (σ^+ , σ^-) polarized photon. Non-radiative transitions between states are also possible. Reprinted with permission from [38]. Copyright 2024 by the American Physical Society.

2.2.2 Nanowire Quantum Dots in Literature

There exists a lot of information about III-V NWQDs including crystal phase NWQDs [39], radial NWQDs [40], and NWQD SPSs [3], [31], [41]. Here we review

recently published works on the growth of chemically defined axial QDs in III-V NWs. Of particular interest is the growth technique and its relation to QD size, interface abruptness, and measured exciton linewidth.

As discussed in Section 2.2.1, hetero-interface abruptness is crucial for high quality QD growth. During VLS growth, interface abruptness is limited by the reservoir effect, which refers to the lingering presence of an element in the liquid droplet that incorporates into the solid even when that element's vapor flux has been extinguished; therefore, there is always some interface broadening due to the reservoir effect even when the vapor flux is instantly halted. Figure 2.12a shows a high-angle annular dark field (HAADF) image of a GaAs/Al_xGa_{1-x}As/GaAs heterostructure grown within a NW. The pixel intensities reflect the changing elemental composition and can be used to estimate the interface abruptness, as shown in Figure 2.12b. It is clear that the interface retains a compositional gradient.

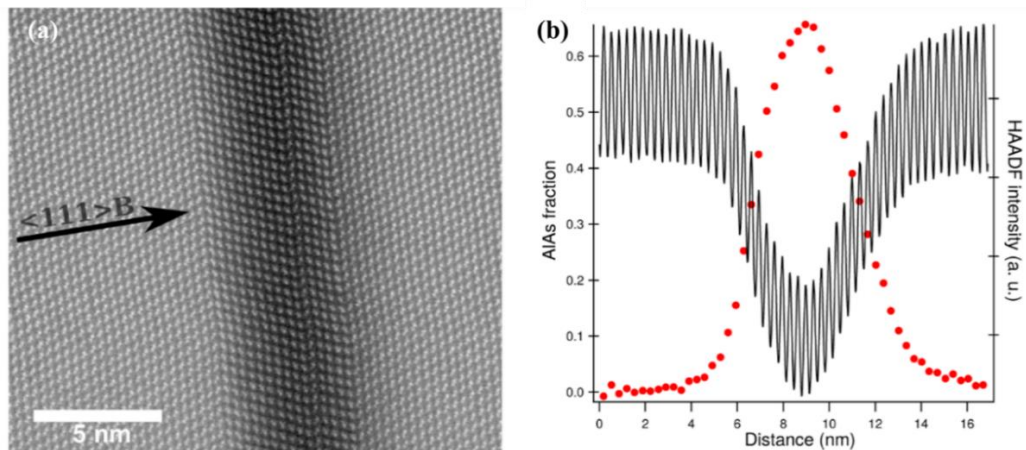


Figure 2.12: Measuring the interface abruptness of a GaAs/Al_xGa_{1-x}As/GaAs heterostructure in a nanowire (NW). (a) High-angle annular dark field (HAADF) image of the heterostructure. (b) The pixel intensity (black) can be used to estimate the elemental composition (red) along the NW. Reprinted with permission from [42]. American Chemical Society

Sharper interfaces can be achieved by optimizing growth conditions. In general, it is easier to abruptly change the group V composition because of the lower solubility of group V species in the liquid droplet [43]. The reservoir effect is also known to be reduced for narrower NWs because the droplet volume is smaller [42]. Furthermore, Leshchenko and Johansson [44] showed that sharper InAs/GaAs and GaAs/AlAs interfaces can be obtained by reducing the growth temperature and increasing the flux of the element forming the heterostructure. Dubrovskii and Sibirev [32] also concluded that growth interrupts and the use of a foreign catalyst such as Au can lead to sharper interfaces, though the former risks droplet instability and the latter may introduce Au contaminants.

Theoretical knowledge of the formation of NW hetero-interfaces has enabled researchers to grow axial NWQDs with atomically abrupt interfaces, as summarized in Table 2.1. Wu et al. [45] grew GaAs QDs in GaAsP NWs using the self-catalyzed VLS method by MBE. During growth, the As beam equivalent pressure was increased to compensate for the termination of the P supply during the formation of the GaAs QD so as to maintain droplet supersaturation. The authors observed sharp interfaces measuring a few MLs, which they attributed to the low solubility and high incorporation rate of P. A low solubility ensures a fast depletion time of P during the switch from AsP to As, while a high incorporation rate enables rapid recovery of the AsP flux condition. Yu et al. [46] and Fonseca et al. [47] also grew GaAs QDs in GaAsP NWs using the self-catalyzed VLS method by MBE. Yu et al. employed a similar flux compensation growth strategy as Wu et al. and demonstrated the formation of atomically sharp interfaces. Fonseca et al. measured broader interfaces

between 6-13 MLs. Asgari et al. [48] grew Au-catalyzed InAs NWs by chemical beam epitaxy. InAs QDs were defined by growing InAsP barrier layers, which exhibited atomically sharp interfaces due to the low solubility of As and P in Au. Zhang et al. [49] grew multiple GaAs QDs in GaAsP NWs using the self-catalyzed VLS method by MBE. They achieved 1.8-3.6 nm interfaces by using a flux compensation method and increasing the growth temperature to 640 °C to decrease the reservoir effect for As and P. Recently, Chang et al. [50] showed that the reservoir effect can also be leveraged to achieve atomically sharp interfaces. They grew InAsP QDs in InP NWs using the Au-catalyzed VLS method by MOCVD. InAsP QD segments were generated by first terminating the flow of the In and P precursors and then pulsing the As precursor. In this way, In and P were incorporated within the QD segment purely by means of the reservoir effect.

Table 2.1: Summary of recent chemically defined axial III-V nanowire quantum dots in literature with reported interface widths.

Year	Authors	Material	QD Width	Interface Width	Exciton Linewidth
2016	Wu et al. [45]	GaAsP/GaAs	40-50 nm	A few MLs	34 meV (77 K); 130 μ eV (5 K)
2019	Yu et al. [46]	GaAsP/GaAs	30-60 nm	“Atomically sharp”	1.8 meV (60 K); 1.2 meV (10 K)
2020	Fonseka et al. [47]	GaAsP/GaAs	~50 nm	~6-13 MLs	80 μ eV (4 K)
2021	Asgari et al. [48]	InAsP/InAs	~50 nm	“Atomically sharp”	Not reported
2021	Zhang et al. [49]	GaAsP/GaAs	~50 nm	1.8-3.6 nm	0.5 meV (6 K); 9.8 meV (140 K)
2022	Chang et al. [50]	InP/InAsP	~66 nm	“Atomically sharp”	219.2 μ eV (4 K)

Table 2.1 also indicates the measured exciton linewidth by photoluminescence (PL) spectroscopy at the indicated temperature. The smallest linewidth was reported by Fonseka et al. as 80 μ eV at 4 K. At higher temperatures the linewidth suffers from thermal

broadening proportional to $k_B T$. Zhang et al. were able to obtain a 9.8 meV linewidth at 140 K, indicative of efficient radiative recombination which often deteriorates at elevated temperatures due to thermal quenching.

Lastly, it is noteworthy that the reported QD widths are larger than the exciton Bohr radius for the relevant material; for instance, Wu et al. report a QD diameter measuring around four times the calculated exciton Bohr radius of GaAs, meaning the degree of confinement in at least two dimensions remains limited by the NW radius. Combining techniques for the growth of ultrathin NWs with the methods of obtaining atomically sharp interfaces presents an interesting challenge and should result in higher quality NWQDs.

Chapter 3: Characterizing Nanowires

3.1 Structural Characterization by Electron Microscopy

A material's structure refers to the arrangement of its atoms; therefore, the structural characterization of a material can be interpreted as the pursuit of the location and identity of each atom within said material. In the context of NWs, structural characterization means defining a NW's morphology, dimensions, material composition, and crystal phase, which is essential to evaluate growth methods and interpret optoelectronic properties.

Characterizing nanostructures such as NWs requires high resolution imaging techniques. Resolution describes the size of the smallest feature that can be discerned from an image. A well-known calculation of the resolution, r , for conventional light microscopy comes from the Rayleigh criterion

$$r = \frac{0.61\lambda}{NA}, \quad (3.1)$$

where λ is the wavelength of light and NA is the numerical aperture of the objective lens. Taking $\lambda = 500$ nm (visible light) and $NA \approx 1$ gives $r = 305$ nm, unsuitable for imaging NWs. More appropriate imaging techniques for NWs include electron microscopy and atom probe tomography (APT). APT is a destructive technique involving the controlled removal of atoms from a sharply pointed sample. As atoms are ripped off of the sample's tip they are characterized by various detectors, enabling an atomic resolution digital reconstruction of the sample. APT is a powerful characterization technique in its own right

and has been used to map the spatial distribution of dopants in NWs, for instance [51]. We restrict our discussion to electron microscopy, which is relevant to this thesis.

Electron microscopy is a structural characterization technique that relies on physical interactions between electrons and atoms. The reason we expect high resolution images by using electrons can be understood as a consequence of the wave-particle duality. The de Broglie wavelength, λ_{dB} , of an electron with momentum \vec{p} is given by

$$\lambda_{dB} = \frac{h}{|\vec{p}|}, \quad (3.2)$$

where h is Planck's constant. By choosing a high momentum it is possible to reduce the de Broglie wavelength; thus, the resolution is improved according to Equation 3.1. In practice, the momentum of incident electrons can be increased by applying a high voltage so as to accelerate electrons with a strong electric field.

Electrons can be used to generate images thanks to scattering events that occur when electrons are incident on a sample of interest. Scattering events can alter the trajectory, energy, and phase relation of incident electrons. During these processes electrons and photons may also be ejected from within the sample. Figure 3.1 distinguishes between different types of electron scattering.

Figure 3.1a shows the case wherein a coherent beam of electrons is incident on a thick sample such that no electrons pass through the sample; instead, electrons interact with atoms in the sample over a finite volume. Incident electrons will lose energy from inelastic scattering events with other electrons; thus, the interaction volume for a given sample will

get larger if the electron beam energy is increased. In some cases, incident electrons may impart sufficient energy to ionize an atom. The electron removed from the atom, called a secondary electron (SE), typically has a low energy (< 15 eV), but can escape from the sample if it is generated near the surface. Incident electrons that are elastically scattered by nuclei in the sample through an angle greater than 90 degrees can also be detected. These so-called backscattered electrons (BSEs) are also usually incoherent, meaning they have lost the phase relation of the incident electron beam.

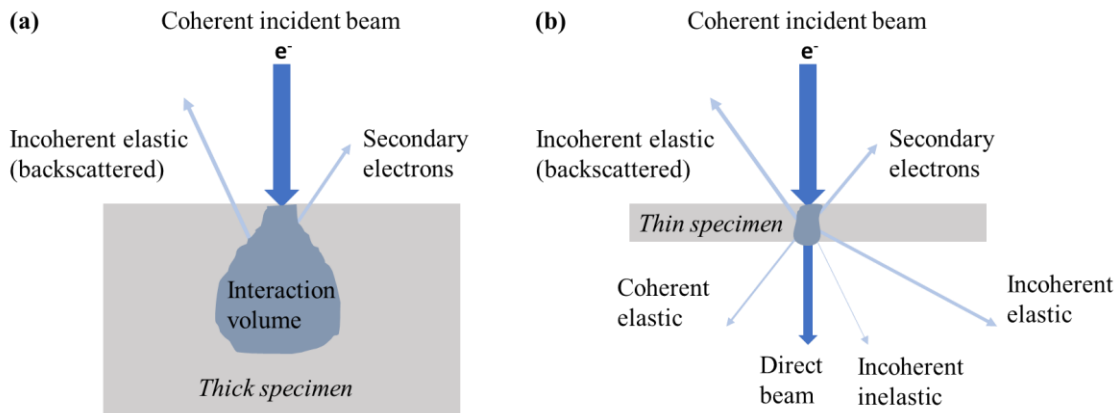


Figure 3.1: Types of electron scattering. (a) An electron beam incident on a thick sample interacts over a certain volume, yielding backscattered and secondary electrons. (b) Electrons also scatter in the forward direction in the case of a thin transparent sample.

When a sample has a thickness on the order of a couple hundred nanometers or less it becomes transparent to an incident electron beam. Figure 3.1b depicts the classification of forward scattered electrons. The direct beam consists of electrons that pass through the sample without scattering. These electrons form the central spot of a diffraction pattern. Incident electrons can also collide with electrons in the sample, resulting in low angle ($< 1^\circ$) incoherent inelastic scattering. Meanwhile, elastic collisions with nuclei result in

coherent elastic scattering at low angles ($1 - 10^\circ$), which becomes incoherent at higher angles ($> \sim 10^\circ$).

Specific details of electron scattering strongly depend on the material composition and topography of the sample being considered; for example, larger nuclei yield a higher fraction of BSEs, meaning areas with heavier atoms will appear brighter than areas with lighter atoms in a SEM image. If electron scattering did not occur there would be no means of creating contrast—a change in intensity over an area—and electron microscopy would not be useful.

3.1.1 Theory of Scanning Electron Microscopy

A SEM operates on the principle of focusing a beam of electrons at a sample and reading the BSE and SE signals; thus, a SEM is suitable for imaging thick samples that are not transparent to the electron beam. The resolution of a SEM is approximated by the interaction volume and so a SEM typically operates with a relatively low accelerating voltage (< 30 kV). Unfortunately, decreasing the interaction volume will also reduce the quantity of BSEs and SEs, meaning image contrast will be sacrificed in the pursuit of higher resolution images. A SEM user must consider the trade-off between resolution and contrast when they take an image.

In the context of NWs, a SEM is a good tool to assess the yield and general morphology of NWs that have just been grown. Figure 3.2 is a SEM image of an array of GaP NWs obtained using the SE signal. The SE intensity does not have a simple relationship with atomic number like the BSE signal, but is fitted approximately by the secant of the angle

of incidence; thus, the SE signal is sensitive to topography, making it useful to visualize the shape of NWs. From the SEM image it is apparent that the right side of the array has a high yield of ordered NWs while the left side of the array has a high yield of disordered NWs. This non-uniformity points to an issue involving substrate preparation prior to NW growth; in particular, the absence of NWs along the left corner of the array suggests some of the array holes did not successfully seed NWs. It might be concluded the holes were not properly defined during EBL or perhaps they are still passivated by a native oxide that was not removed by etching. In this way, a SEM can provide feedback about NW fabrication processes.

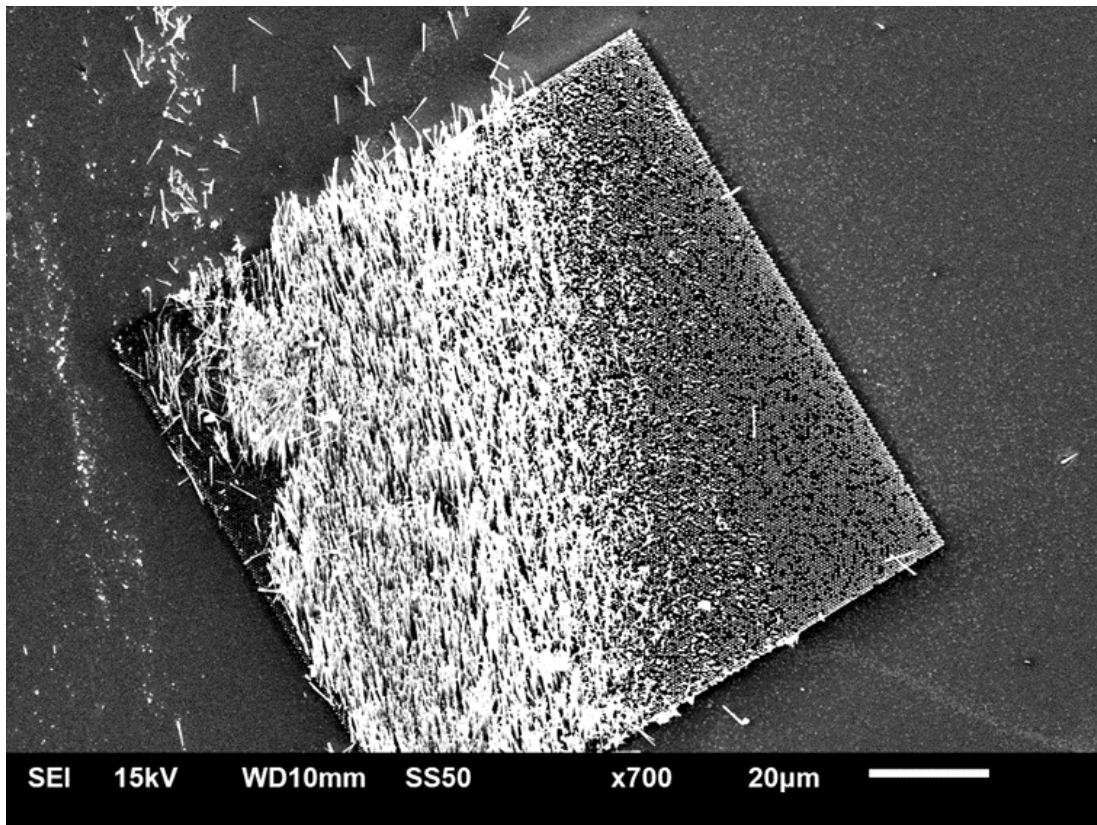


Figure 3.2: Scanning electron microscope image of a square array of GaP nanowires.

The fundamental components of a SEM are illustrated in Figure 3.3. An electron gun supplies electrons that will ultimately probe the sample. A low cost electron gun is a bent tungsten filament that emits electrons when it is heated beyond a threshold temperature; for instance, slowly heating a tungsten filament to over 2000 °C stimulates thermionic emission. The brightness of the source, which has the dimensions of current per unit area per unit solid angle, can be increased by replacing the thermionic gun with a field emission gun (FEG). A FEG can be made, for example, by sharpening a piece of tungsten to yield a tip radius of around 100 nm. Applying a negative bias (on the order of several kVs) to the FEG will generate strong enough electric fields to eject electrons preferentially from the tip. A FEG is more expensive than a thermionic source and must operate in a lower pressure environment, but is brighter and more coherent, meaning the electrons appear to originate from a smaller effective point source and possess a more uniform phase relation.

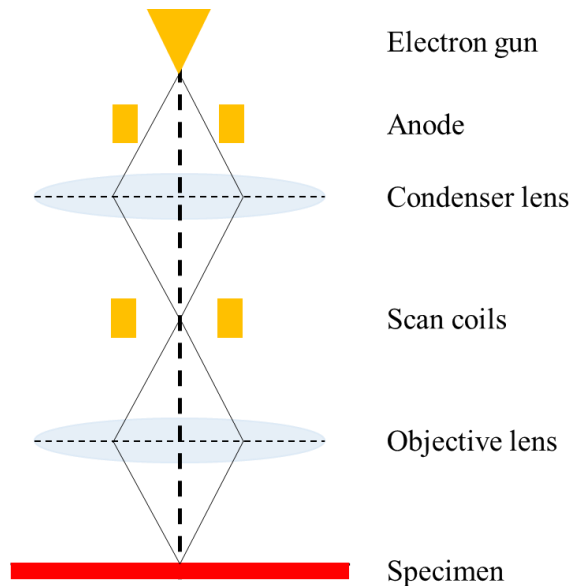


Figure 3.3: Fundamental components of a scanning electron microscope.

A positive voltage is applied to an anode to accelerate the electrons before they reach a condensing lens, which focuses the beam of electrons to a small point. Electromagnetic lenses are used to focus an electron beam. An electromagnetic lens works by exploiting the Lorentz force. Namely, an electron with velocity \vec{v} in a magnetic field \vec{B} will experience a force \vec{F} satisfying

$$\vec{F} = -e \cdot \vec{v} \times \vec{B}, \quad (3.3)$$

where e is the elementary charge. The operating principle of an electromagnetic lens are depicted in Figure 3.4. The lens is effectively a coil of wire that generates a magnetic field along the optical axis when current passes through the coil; for example, a counter-clockwise current generates an axial field \vec{B}_{axial} in the upwards direction. According to Equation 3.3, electrons travelling parallel to the optical axis will not feel a force; however, creating a notch along the perimeter of the lens introduces a radial field component \vec{B}_{radial} such that off-axis electrons will be deflected towards the optical axis along a spiraling helical path. Therefore, the coil of wire behaves like a lens for electrons with a focal length that can be adjusted by changing the strength of the induced magnetic field.

Electromagnetic lenses can never focus electrons to a single perfect point because of inevitable chromatic and spherical aberrations. Chromatic aberration in a lens occurs when electrons of different energies are focused to different points along the optical axis. It follows that the focal point of the lens becomes better approximated by a disc than a point. The size of the disc can be reduced if the energy distribution of incoming electrons is minimized; hence, the best instruments utilize a monochromatic electron source. Spherical

aberration in a lens is a geometric consequence of the reality that electrons further from the optical axis have to travel further than electrons close to the axis. Again, it follows that the focal point of the lens will consequently appear as a disc instead of a point. Spherical aberrations may be reduced by selecting a small aperture that allows only electrons near the optical axis to pass through. In any case, there will always be some aberrations from electromagnetic lenses that limit the ultimate resolution of an electron microscope.

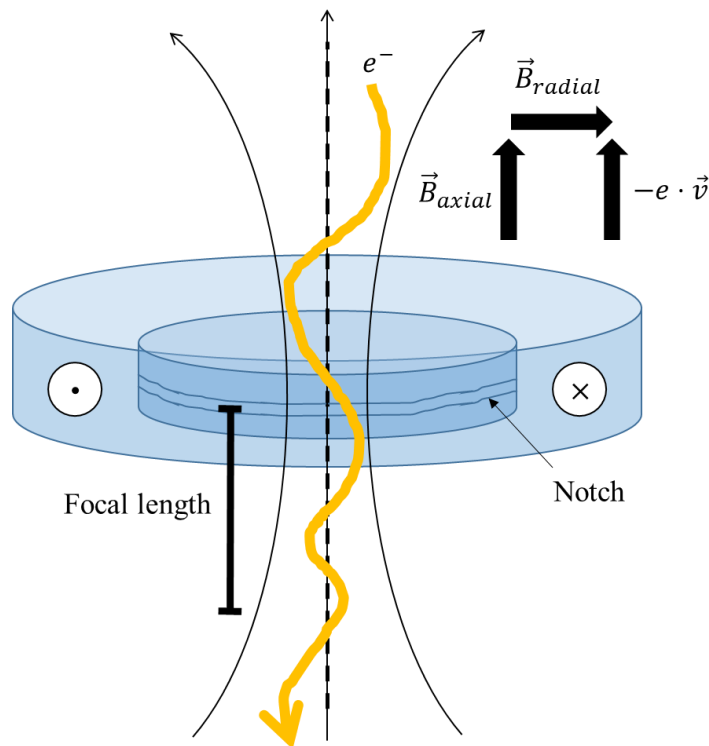


Figure 3.4: Operating principle of an electromagnetic lens. A counter-clockwise current loop creates a magnetic field parallel to the optical axis. A notch along the perimeter of the lens induces a radial magnetic field component that forces off-axis electrons along a spiralling helical path towards the optical axis, effectively focusing the electrons.

Once the electron beam has been focused by the condenser lens, it encounters scanning coils used to deflect the beam. In practice, the beam must be rastered across the sample surface, effectively mapping out individual pixels that together form a cohesive image. Like an electromagnetic lens, scanning coils leverage the charged nature of electrons, deflecting them with an induced magnetic field. Finally, an objective lens focuses the deflected electron beam onto the sample and detectors are used to observe the BSE and SE signals used to generate a SEM image.

3.1.2 Theory of Transmission Electron Microscopy

The TEM employs similar components as the SEM, but forms an image using information from forward scattered electrons instead of from BSEs and SEs. Consequently, a TEM is usually much larger than a SEM as electrons must be accelerated towards the sample and then collected from the other side—requiring a significant number of electrical and optical components to be packed into a long column. A TEM also employs a higher accelerating voltage, typically between 100-300 kV, to ensure electrons have sufficient energy to pass through the sample and to decrease their de Broglie wavelength to enable higher resolution imaging as discussed in Section 3.1.

The power of a TEM comes from its many possible imaging modes. Generally, each imaging mode confers unique information about the structure of the material under investigation; thus, a complete picture of sample structure is usually obtained via TEM imaging at various conditions. Figure 3.5 illustrates the selection of three principal TEM imaging modes, which are intimately related to the image of the sample in reciprocal space.

The reciprocal space image is called the diffraction pattern. Electron diffraction is a consequence of the wave nature of electrons whereby elastically scattered electrons constructively interfere when the difference between incident and scattered wave vectors is equal to a reciprocal lattice vector. Mathematically, this condition reads

$$\vec{K}_I - \vec{K}_D = \vec{g}, \quad (3.4)$$

where \vec{g} is a reciprocal lattice vector and \vec{K}_I and \vec{K}_D are the incident and scattered electron wave vectors, respectively. The dependence of the diffraction condition on \vec{g} implies a diffraction pattern contains information about crystal structure.

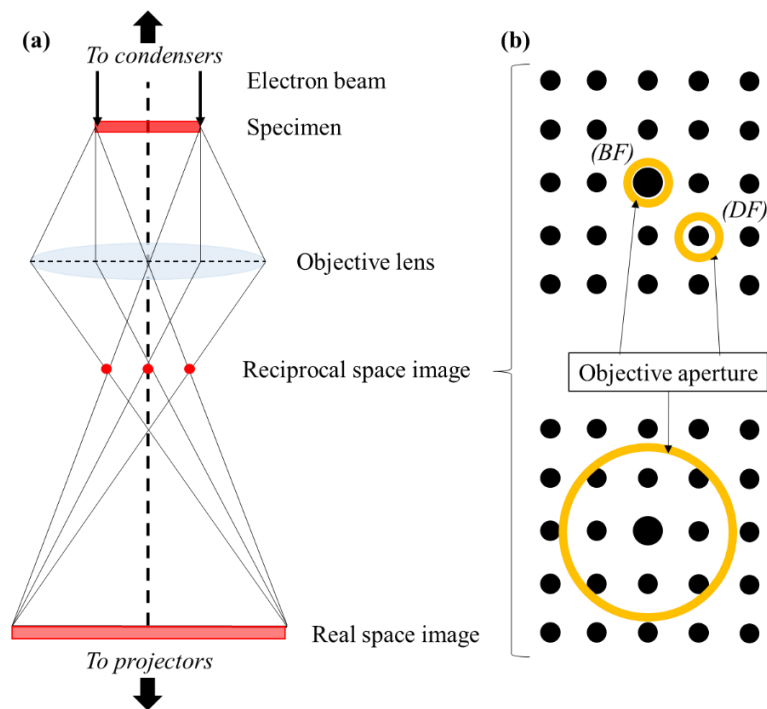


Figure 3.5: Selecting the imaging mode of a transmission electron microscope. (a) A ray diagram showing how the objective lens creates reciprocal space and real space images from electrons that have scattered through the specimen. (b) Representation of a diffraction pattern. Bright field (BF) and dark field (DF) images are obtained by selecting the central spot or a diffracted spot with the objective aperture, respectively. Phase contrast for high resolution images is achieved by selecting multiple spots with the objective aperture.

Figure 3.5a is a ray diagram showing the formation of a diffraction pattern in the back focal plane of the objective lens in a TEM. In practice, a TEM user can observe a diffraction pattern by adjusting the focal lengths of a series of lenses used to project the specimen image onto a viewing screen. Figure 3.5b indicates how an objective aperture positioned in the back focal plane of the objective lens can be used to select different parts of the transmitted electron beam. The simplest TEM imaging mode is called bright field (BF) imaging. A BF imaging condition is achieved by blocking all electrons except those from the central diffraction spot. In this way, objects that scatter more electrons will appear darker, leading to image contrast. Conversely, a dark field (DF) imaging condition is achieved by blocking all electrons except those from a diffraction spot; therefore, a DF image is formed by electrons diffracted by a certain family of lattice planes. It follows that objects that scatter more electrons will appear brighter using a DF imaging condition.

Figure 3.6 compares the relative BF and DF intensities for a “toy” example of a silver/carbon film with variable thickness. The heavier silver atoms scatter electrons more strongly than the carbon atoms. Additionally, thicker parts of the film will also yield a higher fraction of scattered electrons because electrons are forced to travel further through the sample, increasing their scattering probability. As such, the BF intensity is smallest for the thickest portion of the silver side of the film and highest for the thinnest carbon segment. The DF intensity profile is roughly the inverse of the BF intensity profile; however, it is noted the average BF intensity is higher than the average DF intensity because more electrons are contained in the central diffraction spot. Meanwhile, a DF image will generally exhibit a higher contrast than the same BF image.

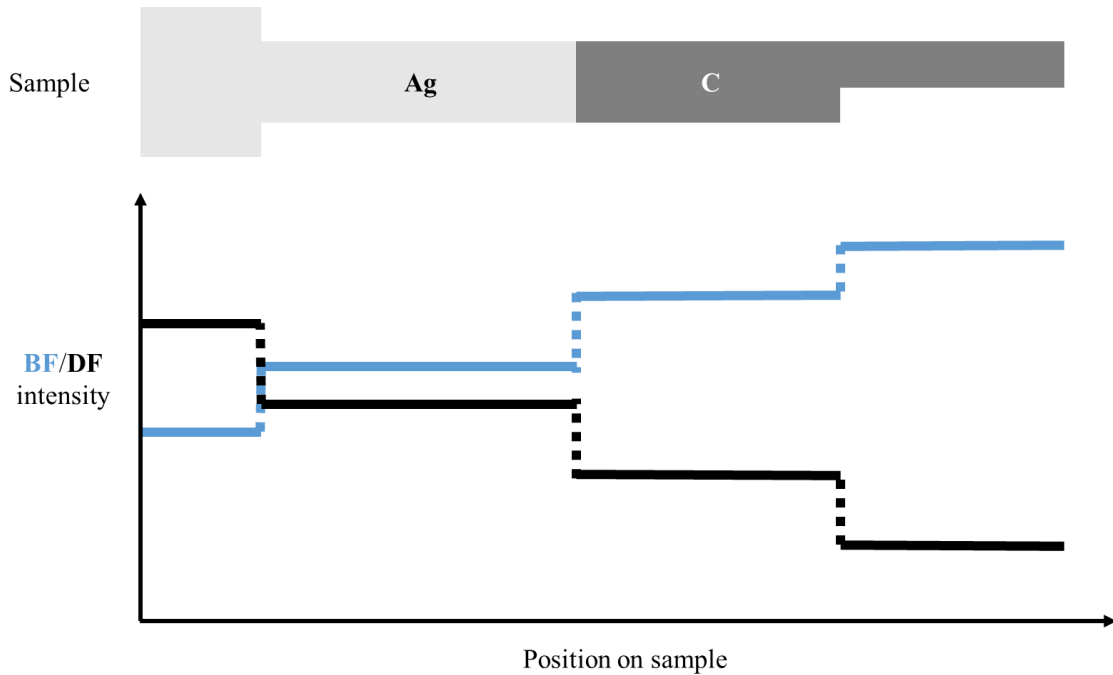


Figure 3.6: Comparison of bright field (BF) and dark field (DF) intensities for an inhomogeneous sample. The average BF intensity is higher than the average DF intensity, but the DF image exhibits a higher contrast than the BF image.

It is also possible to form an image using multiple spots in the diffraction pattern simultaneously. The coherent interference of multiple diffracted beams gives rise to what is called phase contrast. Each diffraction spot thus contributes to the final image. Such an approach is used to obtain high resolution TEM (HRTEM) images, which are capable of sub-angstrom (atomic) resolution. The resolution of the image is determined by the highest spatial frequency that can be transferred from the specimen to the final image by the TEM optics since a high spatial frequency corresponds to a small distance. Ideally, an arbitrarily high spatial frequency could be selected to obtain the best possible resolution; however, high spatial frequencies correspond to large distances in reciprocal space (getting further

away from the optical axis) and so points on the sample will be spread into discs as a consequence of spherical aberrations as discussed in Section 3.1.1. Consequently, each point in a final image contains contributions from many points on the sample, creating a distortion and limiting the resolution. It can be shown that points on a thin sample are related to points on the resulting image by the transfer function $T(\vec{u})$ [52]:

$$T(\vec{u}) = 2A(\vec{u})\sin\chi(\vec{u}). \quad (3.5)$$

Here, \vec{u} denotes the reciprocal lattice vector and $A(\vec{u})$ and $\chi(\vec{u})$ are known as the aperture and phase-distortion functions, respectively. Equation 3.5 is derived under the weak phase-object approximation, which linearly relates the amplitude of the transmitted electron wave function to the sample's projected potential. Ideally, the transfer function is constant up until a certain value of \vec{u} , which determines the resolution as shown in Figure 3.7a. A constant transfer function enables an interpretable image; specifically, atoms will appear bright when $T(\vec{u})$ is negative (positive phase contrast), but will appear dark when $T(\vec{u})$ is positive (negative phase contrast). The sinusoidal term of Equation 3.5 generates oscillations as determined by the phase-distortion function, leading to undesired transitions between positive and negative phase contrast and confusing image interpretation. The phase-distortion function has the form

$$\chi(\vec{u}) = \pi\Delta f\lambda_{EB}|\vec{u}|^2 + \frac{1}{2}\pi C_s\lambda_{EB}^3|\vec{u}|^4, \quad (3.6)$$

where Δf is the objective lens defocus, λ_{EB} is the electron wavelength, and C_s is the spherical aberration coefficient of the objective lens. The transfer function with the fewest

zeros is obtained by balancing the effects of spherical aberration in Equation 3.6 using a special defocus value called the Scherzer defocus Δf_{Sch} :

$$\Delta f_{Sch} = -1.2(C_s \lambda_{EB})^{\frac{1}{2}}. \quad (3.7)$$

The Scherzer defocus is negative and corresponds to focusing the objective lens on a plane below the sample. Figure 3.7b compares the sinusoidal component of the transfer function under zero defocus and under the Scherzer defocus condition. Choosing the Scherzer defocus condition facilitates more constant transfer characteristics at lower values of the reciprocal lattice vector and also extends the first zero crossing compared to the case of zero defocus, enabling higher resolution imaging.

The study of NWs is greatly aided by HRTEM imaging. HRTEM images facilitate the determination of crystal phase and the assessment of defects with atomic precision, for example. In Chapter 5 we use HRTEM images to map out the crystal phase transitions in our Te-doped GaP NWs. We also used BF TEM images to measure the size of our NWs. In general, there is a lot more information about NWs that can be obtained using a TEM; for instance, in situ TEM techniques have been developed to study the growth of NWs in real time [18], [19], [20]. Some other powerful TEM techniques that are not employed in this thesis include scanning TEM (STEM) imaging, HAADF STEM imaging, energy dispersive X-ray (EDX) spectroscopy, and electron energy loss spectroscopy (EELS).

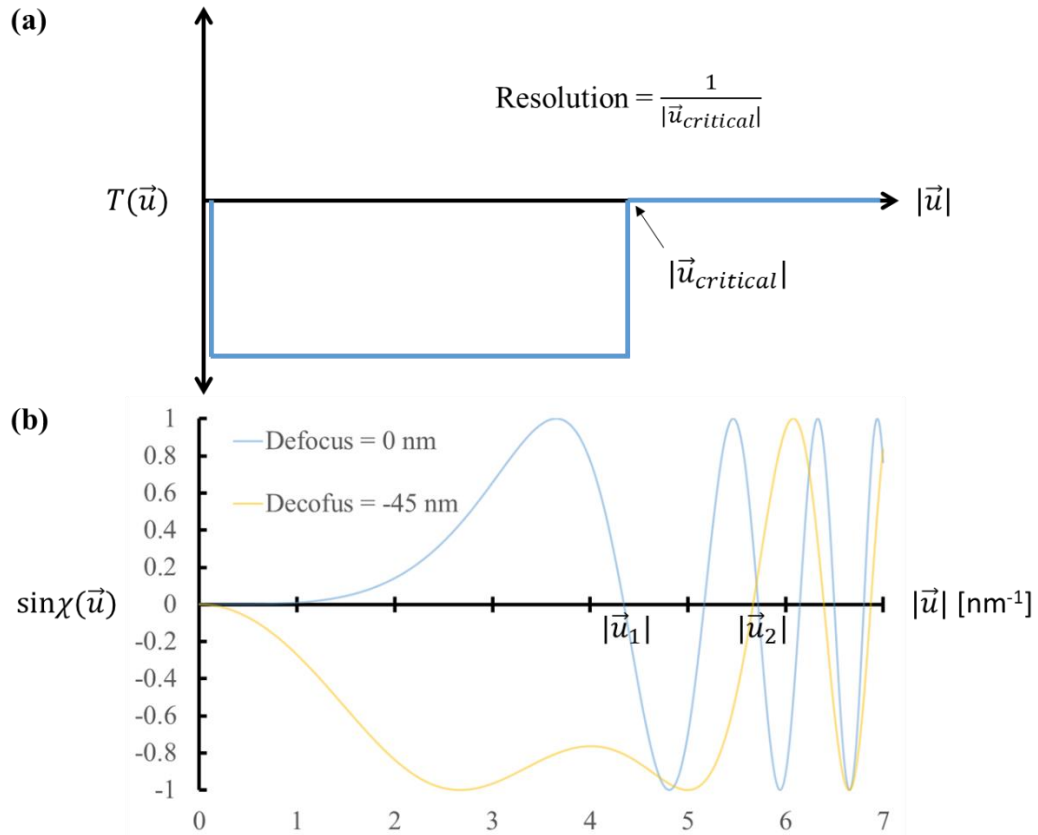


Figure 3.7: Visualization of the transfer function of a phase contrast transmission electron microscope image. (a) An ideal transfer function is constant up to a critical reciprocal vector $|\vec{u}_{critical}|$, which determines the resolution. (b) The sinusoidal component of the transfer function induces oscillations between positive and negative phase contrast. Choosing the Scherzer defocus condition ($\Delta f_{sch} \approx -45$ nm for an example case $C_s = 700 \mu\text{m}$ and $\lambda_{BE} = 2$ pm) yields more ideal transfer function characteristics and a higher resolution since $|\vec{u}_2| > |\vec{u}_1|$.

3.2 Optical Characterization Techniques

Optical characterization techniques aid in understanding the electronic structure of a material. In general, an optical characterization technique involves perturbing the semiconductor from its equilibrium ground state into an excited state and then observing the photons emitted as the semiconductor relaxes back to its ground state. The detected

photon energies and their relative intensities can then be used to infer the characteristics of various optical processes involved during the relaxation. Usually spectral interpretation is non-trivial; therefore, it is beneficial to utilize several optical characterization techniques and perform repeated measurements before forming conclusions about electronic structure.

In this thesis, PL, CL, and Raman spectroscopy were used to characterize our GaP NWs. These techniques are useful for NW characterization because an objective lens can be used to focus the laser or electron beam used to excite the sample, enabling spatially resolved measurements on a single NW. The following three sections discuss the principles of PL, CL, and Raman spectroscopy, respectively.

3.2.1 Theory of Photoluminescence

PL spectroscopy uses a laser beam excitation; thus, the semiconductor is brought to its excited state by absorbing a photon. Photon emission to return the semiconductor to its ground state can occur via a number of optical processes. As discussed in Section 2.2.1, an exciton (electron-hole pair) can recombine, producing a photon. Excitons can be distinguished as free excitons or bound excitons. A free exciton can move freely through the crystal while a bound exciton is bound to an impurity or defect in the crystal. A free exciton has a linewidth on the order of 1 meV while the linewidth of a bound exciton is typically ten times narrower [53]. Figure 3.8a and Figure 3.8b depict the free exciton radiative transition for the case of a direct and indirect bandgap semiconductor, respectively. When the conduction band minimum and valence band maximum are aligned the momentum k is directly conserved and the emitted photon energy is

$$h\nu = E_g - E_x, \quad (3.8)$$

where E_g is the bandgap energy and E_x is the ionization energy of the electron-hole pair. In the case of an indirect bandgap, a phonon with energy E_p must supply the missing momentum to facilitate the transition and so the energy of the emitted photon is

$$h\nu = E_g - E_x - mE_p. \quad (3.9)$$

Here, m is the number of phonons involved in the process. Transitions with $m > 1$ are called phonon replicas in the collected emission spectrum and become progressively weaker as m becomes larger. Note that phonons are necessary for indirect transitions, but can also occur in direct transitions.

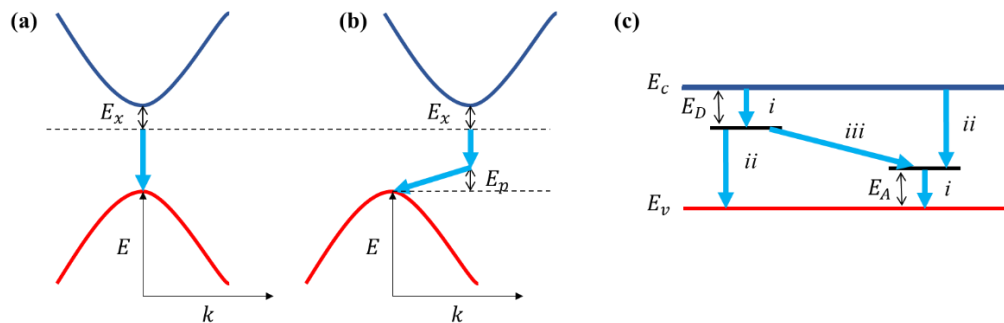


Figure 3.8: Fundamental radiative transitions in a semiconductor. (a) Recombination of an exciton with ionization energy E_x in a direct bandgap semiconductor. (b) Recombination of an exciton in an indirect bandgap semiconductor requires help of a phonon with energy E_p to conserve momentum k . (c) The presence of donor and acceptor levels leads to the possibility of shallow (*i*), deep (*ii*), and donor-acceptor level (*iii*) transitions.

The recombination of a bound exciton can be visualized in a similar fashion; however, the ionization energy of the original free exciton complex is modified to account for the additional energy E_b needed to bind the exciton to the impurity center:

$$E_i = E_x + E_b . \quad (3.9)$$

The ionization energy E_i of the bound exciton can be estimated by calculating the binding energy from a measured temperature dependent intensity curve [54], which follows the Arrhenius relation

$$I = \frac{1}{1 + c \cdot \exp\left(-\frac{E_b}{k_B T}\right)}, \quad (3.10)$$

where I is intensity, T is absolute temperature, k_B is the Boltzmann constant, and c is a prefactor.

The presence of donors and acceptors in the semiconductor can also facilitate radiative transitions, as depicted in Figure 3.8c. Ionized donors and acceptors have levels within the bandgap determined by their respective ionization energies E_D and E_A . These levels support shallow transitions (process *i*), deep level transitions (process *ii*), and donor-acceptor pair transitions (process *iii*). The latter process leads to the photon energy

$$h\nu = E_g - E_D - E_A - \frac{q^2}{4\pi\epsilon r}, \quad (3.11)$$

where the last term describes the energy shift due to the coulomb interaction between charges q in a material with dielectric constant ϵ and separation r .

3.2.2 Theory of Cathodoluminescence

CL spectroscopy uses an electron beam to excite a sample instead of a laser. The electrons are more energetic than photons used in PL and so CL enables the excitation of larger

bandgap semiconductors; however, the high energy beam can cause damage to the sample. The electron beam can also be focused to a smaller spot size and easily rastered across a sample using SEM controls, enabling spatially resolved measurements. In terms of optical processes, CL can be used to observe the same radiative pathways described in Section 3.2.1, and so this method is useful for confirming PL results.

3.2.3 Theory of Raman Spectroscopy

Raman spectroscopy is unique from PL and CL in that it aims to investigate a material's phonon modes. Each mode corresponds to a characteristic lattice vibration and observation of different modes generally depends on selection rules governed by crystal orientation, light polarization, and chosen scattering geometry. Practically, Raman is conducted by illuminating a sample with a focused laser and observing the light that is scattered. Light is usually elastically scattered; however, some light is inelastically scattered via the process of phonon absorption (anti-Stokes) or phonon emission (Stokes). The measured energy change between the direct and scattered beam is usually expressed as the Raman shift with units of cm^{-1} .

Phonon modes in a crystal are classified by the direction of atomic oscillations and the relative vibration between atoms. The directionality of the atomic oscillations can be described as transverse or longitudinal while relative vibrations between atoms can be acoustic or optical. Acoustic phonon modes involve the movement of atoms in the same direction with the same phase. Optical phonon modes involve the movement of atoms in opposite directions and may interact with light due to the change in dipole moment caused

by these oscillations. Thanks to their high surface area to volume ratio, NWs can support a surface optical (SO) phonon mode, which lies between the transverse optical (TO) and longitudinal optical (LO) modes [55]. The small diameter of NWs may also cause slight frequency shifts and broadening to phonon peaks when compared to the bulk case [56].

Recently, Kang et al. [57] measured the Raman shifts of the characteristic phonon modes of WZ and ZB GaP NWs. The relevant values are given in Table 3.1. Of interest are the distinct EL 2 (low frequency) and EH 2 (high frequency) modes that arise only for the WZ crystal structure. It follows that a distinction between WZ and ZB GaP can be made purely by Raman spectroscopy.

Table 3.1: Experimentally measured Raman shift of characteristic phonon modes of wurtzite (WZ) and zincblende (ZB) GaP nanowires. The A and E notation comes from group theory. Data from Ref. [57].

Raman Shift (Phonon Mode)						
WZ	77.7 cm ⁻¹ (EL 2)	356 cm ⁻¹ (EH 2)	364.5 cm ⁻¹ [E ₁ (TO)]	-	394.8 cm ⁻¹ [A ₁ (LO)]	401.2 cm ⁻¹ [E ₁ (LO)]
ZB	-	-	363 cm ⁻¹ (TO)	394 cm ⁻¹ (SO)	-	401 cm ⁻¹ (LO)

Chapter 4: Experimental Methods

4.1 Nanowire Growth

Three key GaP NW samples are involved in the present study. Each sample was grown via identical processes save for the incorporation of different dopants during MBE growth. The three NW variants are Be+Te-doped, Be-doped, and undoped. Section 4.1.1 describes the substrate preparation prior to NW growth and Section 4.1.2 summarizes the NW growths by MBE. It is acknowledged that Amanda Thomas from McMaster University is responsible for the preparation of all three NW substrates and for the growth of the Be+Te-doped and Be-doped NWs. Spencer McDermott from McMaster University is acknowledged for the growth of the undoped NWs. Alex Tsukernik from the University of Toronto is acknowledged for the performance of EBL on all substrates.

4.1.1 Substrate Preparation

A single side polished three-inch p-type Si(111) wafer was sourced from Virginia Semiconductor to act as a substrate for NW growth. A 30 nm oxide layer was deposited onto the intact layer by CVD. To achieve the correct oxide thickness, a substrate temperature of 500 °C was attained and 2.5 sccm of SiH₄ and 25 sccm of O₂ were flowed over the sample for 21 minutes using a balanced forward/reflected power of 500 W. Next, EBL was performed on the wafer. The wafer was degreased via sonication in acetone for one minute followed by sonication in IPA for another minute. A 1:1 solution of AR-P 6200.3/Anisole was used as the EBL resist. The resist was spun onto the wafer at 6000 rpm

for one minute and then baked at 150 °C for another minute. The sample was then loaded into the EBL instrument. The inscribed EBL pattern was developed in ZED-N50 for two minutes and then immersed in IPA for a minute. The EBL pattern is visualized in Figure 4.1. Note that the original wafer is cleaved into six identical “pie” pieces before MBE growth and so the same EBL pattern is repeated six times on unique areas of the wafer. Each EBL pattern consists of six 1 mm² NW pads and a larger TEM pad. Each row (R1-3) contain NW pads with identical patterns. Each column (C1-3) consists of hexagonal NW arrays with a pitch of either 360 nm, 600 nm, or 1000 nm. The hole diameter for the NW arrays was 100 nm.

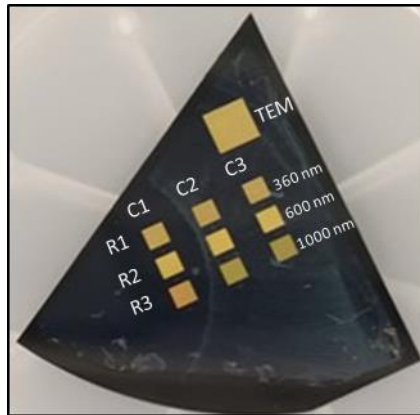


Figure 4.1: The electron beam lithography pattern consists of six 1 mm² nanowire (NW) pads and a larger TEM pad. Each row (R1-3) contain NW pads with identical patterns. Each column (C1-3) consists of square NW arrays with a pitch of either 360 nm, 600 nm, or 1000 nm. Image credited to Amanda Thomas.

The EBL pattern was then transferred to the oxide layer by RIE with a CF₄ plasma. The wafer was cleaved into six identical pie pieces prior to this step, facilitating the growth of up to six unique NW samples from each wafer. The etch was conducted by flowing 10 sccm

of CF_4 for 75 s using a power of 100 W. To remove the EBL resist, each pie piece was sequentially submerged in 1,3-dioxolane (5 minutes), acetone (3 minutes), and IPA (3 minutes).

4.1.2 Growth by Molecular Beam Epitaxy

Prior to MBE growth, the native oxide was removed by etching the substrate for 20 s with a 10:1 buffered HF solution, followed by rinsing with DI water for one minute, and then drying with N_2 . The substrate was then quickly loaded into the MBE reactor's UHV environment ($\sim 10^{-9}$ Torr) to prevent further oxidation. Degassing was conducted inside the MBE reactor's preparation chamber by heating the sample to 300 °C for 15 minutes. The substrate was then moved into the growth chamber in preparation for NW growth.

Table 4.1 outlines the growth protocol for the Be+Te-doped GaP NWs. Ga droplets were established in the holes using a Ga pre-deposition of 250 s in the MBE reactor at a Ga impingement rate corresponding to 0.125 $\mu\text{m}/\text{h}$ and substrate temperature of 650 °C. The GaP NW growth proceeded for a duration of 90 min at a substrate temperature of 650 °C, V/III flux ratio of 3, and Ga impingement rate corresponding to 0.125 $\mu\text{m}/\text{h}$ – conditions which result in a GaP base with nearly 100% yield of vertical NWs. Furthermore, a nominal Be dopant flux corresponding to a carrier concentration of 10^{19} cm^{-3} was incorporated during this growth step. Subsequently, the substrate temperature was set at 520 °C, Ga impingement rate at 1 $\mu\text{m}/\text{h}$, and V/III flux ratio at 2 for the remainder of growth. A nominally undoped GaP segment was grown for 37 min, followed by a Te-doped segment grown for 7 min. The Te dopant flux was supplied by a GaTe valved cracker cell operating

at 550 °C, corresponding to a nominal doping level in GaP of $5 \times 10^{18} \text{ cm}^{-3}$ as determined by Hall effect measurements on thin films. The actual Te dopant incorporation in the GaP NWs requires further study but is expected to be lower than the nominal value by about an order of magnitude based on other NW studies [58]. Regardless of the actual dopant incorporation, the introduction of the Te dopant flux during NW growth had a profound effect on the NW morphology and crystal structure as discussed in Chapter 5. Growth was terminated by shuttering the Ga beam and cooling under P₂ flux.

The Be-doped GaP NWs were grown by an identical method, except the final growth step involving the Te dopant was omitted (Table 4.2). The undoped sample was grown using the same steps as the Be+Te-doped sample, except no dopants were included (Table 4.3).

Table 4.1: Molecular beam epitaxy growth protocol of the Be+Te-doped GaP nanowire sample.

Segment	Time	Temperature (°C)	Doping Concentration (cm ⁻³)	Growth Rate (µm/h)	V/III Ratio
Start					
Ga	250 s	650	None	0.125	-
GaP	90 min	650	Be - 10^{19}	0.125	3
GaP	37 min	520	None	1	2
GaP	7 min	520	Te - 5×10^{18}	1	2
End					

Table 4.2: Molecular beam epitaxy growth protocol of the Be-doped GaP nanowire sample.

Segment	Time	Temperature (°C)	Doping Concentration (cm ⁻³)	Growth Rate (µm/h)	V/III Ratio
Start					
Ga	250 s	650	None	0.125	-
GaP	90 min	650	Be - 10 ¹⁹	0.125	3
GaP	37 min	520	None	1	2
End					

Table 4.3: Molecular beam epitaxy growth protocol of the undoped GaP nanowire sample.

Segment	Time	Temperature (°C)	Doping Concentration (cm ⁻³)	Growth Rate (µm/h)	V/III Ratio
Start					
Ga	250 s	650	None	0.125	-
GaP	90 min	650	None	0.125	3
GaP	37 min	520	None	1	2
GaP	7 min	520	None	1	2
End					

4.2 Structural Characterization Methods

Structural characterization was carried out at the Canadian Center for Electron Microscopy (CCEM). Section 4.2.1 details the methods for SEM characterization and Section 4.2.2 describes the methods for TEM characterization. Carmen Andrei and Natalie Hamada from the CCEM are acknowledged for their help with TEM characterization. Chris Butcher from the CCEM and Amanda Thomas are acknowledged for their help with SEM imaging.

4.2.1 Scanning Electron Microscopy

The as-grown NWs were imaged using a FEI Magellan 400 operating at 2 kV. The NW length and diameter were assessed from SEM images taken at a 30° tilt relative to the substrate normal. Measurements were made by counting pixels in Inkscape and translating the pixel count to units of length using the calibrated scale bar associated with the SEM images.

4.2.2 Transmission Electron Microscopy

NWs were prepared for TEM analysis by mechanical transfer onto a holey carbon grid. BF TEM images were obtained using a Thermo Scientific Talos L120C operating at 120 kV. These were used to gauge the tapering of the Be+Te-doped NWs and to assess the crystal structure of the NWs via selective area electron diffraction. HRTEM images were obtained using a Thermo Scientific Spectra Ultra operating at 300 kV.

4.3 Optical Characterization Methods

Optical characterization consisted of low temperature PL, low temperature CL, and room temperature Raman spectroscopy. Jonas Lähnemann and Kasigo Loeto from the Paul-Drude Institute are acknowledged for their role in conducting the CL measurements. Alain Moréac from the University of Rennes is acknowledged for performing the Raman measurements. The PL measurements were done at McMaster University. All samples were prepared by mechanically dispersing the as-grown NWs onto a p-doped Si substrate, enabling single NW measurements.

4.3.1 Photoluminescence

Micro-PL measurements were conducted by first cooling the NWs to 10 K using a He-cooled cryostat. Next, the NWs were excited by a 488 nm Ar⁺ laser focused by a 60× objective, producing a spot size on the order of 1 μm. It was discovered that the PL from a single NW was too weak to detect and thus PL spectra were obtained from small groups of ~10 NWs. Luminescence was collected by a 0.55 m Horiba Jobin Yvon spectrometer (0.2 mm slit, 1200 lines/mm 750 nm blazed grating) and dispersed onto a LN₂ cooled Si charge-coupled device (CCD) detector.

4.3.2 Cathodoluminescence

Spatially resolved CL data was collected via line scans along the growth direction of individual Be-doped and Be+Te-doped NWs. CL spectroscopy was performed in a Zeiss Ultra 55 field-emission SEM fitted with a Gatan MonoCL4 system. The acceleration voltage was 5 kV and the beam current was 500-600 pA. The NWs were cooled to 10 K using a He-cold stage. Luminescence from the NWs was directed by a parabolic mirror and dispersed by a 600 lines/mm grating blazed at 800 nm before being detected by a CCD.

4.3.3 Raman Spectroscopy

Spatially resolved micro-Raman was conducted using a HR 800 instrument (Horiba – Jobin Yvon) with a 532 nm excitation wavelength. The focused laser spot size was approximately 1 μm and the resulting spectral resolution was roughly 1.2 cm⁻¹.

Chapter 5: Ultrathin Te-Doped GaP Nanoantenna with Crystal Phase Transitions

The results presented in this chapter are based on the publication:

E. Diak, A. Thomas, V. G. Dubrovskii, and R. R. LaPierre, “Ultrathin Te-Doped GaP Nanoantenna with Crystal Phase Transitions,” *Crystal Growth & Design*, vol. 23, no. 7, pp. 5074–5082, Jul. 2023.

The work is credited to the listed authors. In particular: Amanda Thomas is acknowledged for the growth of the NWs used in this study; and Vladimir Dubrovskii is acknowledged for the composition of the growth model presented in Section 5.3.

5.1 Introduction

As discussed in Chapter 2, III-V NWs can be realized by the self-assisted VLS growth method where a liquid metal droplet becomes a collector for adatoms, resulting in site-selective growth. The NW radius, determined by the size of the droplet, is typically greater than about 25 nm. However, many applications, such as single photon sources [3], require even thinner NWs for the realization of quantum dot heterostructures; for example, a NW radius below about 12.5 nm is required for quantum confinement in GaAs [35] and about 10 nm in GaP [36]. Self-assisted growth of GaAs NWs with a stable radius below 10 nm were obtained by shrinking the droplet size using a three-step MBE procedure [59]. The droplet shrinkage was accompanied by a change in the crystal structure from ZB to WZ. Even thinner Au-assisted GaAs NWs exhibiting a ZB phase and a stable radius down to 5 nm have been demonstrated using hydride vapor phase epitaxy, a technique that favors nearly pure axial growth [60]. Despite the development of NW growth processes over the

past decade, the implementation of ultrathin NWs remains challenging for self-assisted NWs.

Besides controlling the NW diameter, another challenge is the doping of semiconductor NWs due to the different growth mechanisms of NWs as compared to conventional thin films. A review of doping in III-V NWs is available in Refs. [61] and [62]. Firstly, silicon is typically an n-type dopant in III-V epitaxy but can exhibit amphoteric behavior in NWs [63], [64]. To circumvent this difficulty, Te has been investigated as an alternative n-type dopant in NWs [65], [66]. Secondly, the introduction of dopants during growth of NWs has been found to influence the NW morphology. For example, the introduction of Te dopant has been found to suppress axial growth and favor radial growth in InAs NWs grown by MOCVD due to a surfactant effect [67]. Thirdly, the crystal structure of NWs can be influenced by doping. For example, the accumulation of dopants into the Ga droplet of self-assisted GaAs NWs grown by MBE can lead to the change of the Ga droplet properties and influence the crystal structure of NWs [68]. The most dramatic example of the latter effect is seen in the Te-doping of self-assisted GaAs NWs, which was previously shown to produce twinning superlattices (TSLs) [69]. TSLs are described by ZB twinning along the (111)B NW growth direction accompanied by sidewall microfaceting due to alternating widening and narrowing facets. The formation of TSLs is sensitive to the substrate temperature and V/III flux ratio [70], with periodic TSLs forming between 492 and 537 °C using a V/III flux ratio of 0.5. Otherwise, the NWs exhibited nonperiodic twinning or a pure ZB structure with vertical facets.

In this chapter, we investigate the effect of a Te dopant flux on self-assisted GaP NWs grown by MBE, which has not been studied to date. The GaP NWs display a novel behavior whereby the introduction of a Te-dopant flux is accompanied by an abrupt positive tapering with a transition from ZB to WZ structure, resulting in a record ultrathin (5 nm in radius) nanoantenna. Furthermore, radius oscillations are observed along the nanoantenna, coinciding with polytypic phase segments. These results present a synergy between NW doping, morphology, and crystal structure and represent a new method of NW engineering. The decrease in NW radius is attributed to the suppression of surface diffusion of Ga adatoms on the NW sidewalls by the Te dopant atoms and the radius oscillations to the existence of two stable orientations of the narrowing and widening sidewall facets. These results may have applications in thermoelectrics [71], [72] and crystal phase quantum dots [73], [74], [75] where ultrathin NWs are desired. Ultrathin nanoantenna may also have photonic applications, for example as short-wavelength absorbers in NW-based photodetectors [30].

5.2 Structural Characterization

Selective-area GaP NWs were grown on Si(111) by the self-assisted (with a Ga droplet) VLS method in a gas source MBE system, using an array of holes in an oxide mask with pitch of 360, 600, or 1000 nm (see Section 4.1). NW growth was limited to the patterned area where Ga droplets nucleated in the holes of the oxide mask, as confirmed by SEM for the three different pitches (Figure 5.1a-c). Only a few parasitic NWs were observed outside the NW array region, likely due to pinholes in the oxide mask. The NWs exhibited a base

segment with hexagonal cross-section, presenting six (110)-type sidewall facets followed by an ultrathin “nanoantenna” (Figure 5.1a-c) that was most evident for a pitch of 600 nm. The NWs for a pitch of 360 nm exhibited a base segment with a length of 1770 ± 10 nm, and negative tapering with a bottom radius of 67 ± 3 nm and top radius of 111 ± 4 nm, ascertained by observation of NWs near the edge of the array as in Figure 5.1a. Similarly, the NWs in Figure 5.1b for a pitch of 600 nm exhibited a base segment with a length of 1874 ± 7 nm, bottom radius of 92 ± 5 nm, and top radius of 160 ± 5 nm, while the NWs in Figure 5.1c for a pitch of 1000 nm exhibited a base segment with a length of 1893 ± 10 nm, bottom radius of 119 ± 3 nm, and top radius of 176 ± 4 nm. Thus, the NW length and radius increased with pitch as expected due to increasing adatom flux with pitch owing to Ga diffusion from the oxide mask surrounding the NWs, and Ga and P₂ re-emitted by desorption from the oxide mask [76], [77], [78]. The NWs closer to the center of the NW array may have slightly different dimensions than those at the edge, but their view is blocked by neighboring NWs in the dense array. Therefore, we use TEM analysis of individual NWs for the growth model discussed below.

The NWs in Figure 5.1b showed a remarkable transition from negative tapering to strong positive tapering (Figure 5.1e), resulting in nanoantenna with length of about 3.5 μm and top radius as thin as 5 nm radius (Figure 5.1f, g). These nanoantenna are attributed to the introduction of the Te dopant flux, since identical NW growths but without the Te-doped segment showed similar base segments for the three different pitches but without any nanoantenna, as illustrated by the SEM image in Figure 5.1d for the 600 nm pitch. With the addition of Te flux, nanoantenna were observed throughout the NW array for the 600

nm pitch (Figure 5.1b), but only along the edges of the NW array for the 360 nm pitch (Figure 5.1a), and sparsely for the 1000 nm pitch (Figure 5.1c). The nanoantenna yield (fraction of NWs with an antenna) was approximately 34% for the 600 nm pitch and 12% for the 1000 nm pitch. NWs without the nanoantenna exhibited crystallites at their top, indicative of Ga droplet consumption prior to nanoantenna formation.

Closer examination of the nanoantenna (Figure 5.1f) revealed radius oscillations along the NW length. TEM analysis was used to further examine this feature of the NWs. The TEM image in Figure 5.2a shows a representative NW from the array of 600 nm pitch. The NW base on the left of Figure 5.2a exhibited a twinned ZB structure, as confirmed by SAED in Figure 5.2b. The HRTEM of the NW tip in Figure 5.2c revealed a radius of about 5 nm. The dark contrast bands in the NW antenna in Figure 5.2a (red arrows) are polytypic regions with WZ/ZB mixing, as shown in the higher magnification TEM image in Figure 5.2d (see Appendix A for HRTEM images and SAED patterns). Each polytypic region coincided with a local increase in radius as seen in Figure 5.2d. Between each polytypic region, the NW structure was WZ as shown in the HRTEM image in Figure 5.2e, with the presence of only a few stacking faults (ZB insertions). Figure 5.2e shows the transition from the predominantly WZ stacking (ABAB...) of the NW antenna, followed by the random WZ/ZB stacking sequence at the onset of the polytypic region. Besides the polytypic regions, the predominantly WZ structure continued along the entire length of the nanoantenna including the tip in Figure 5.2c (see Appendix A).

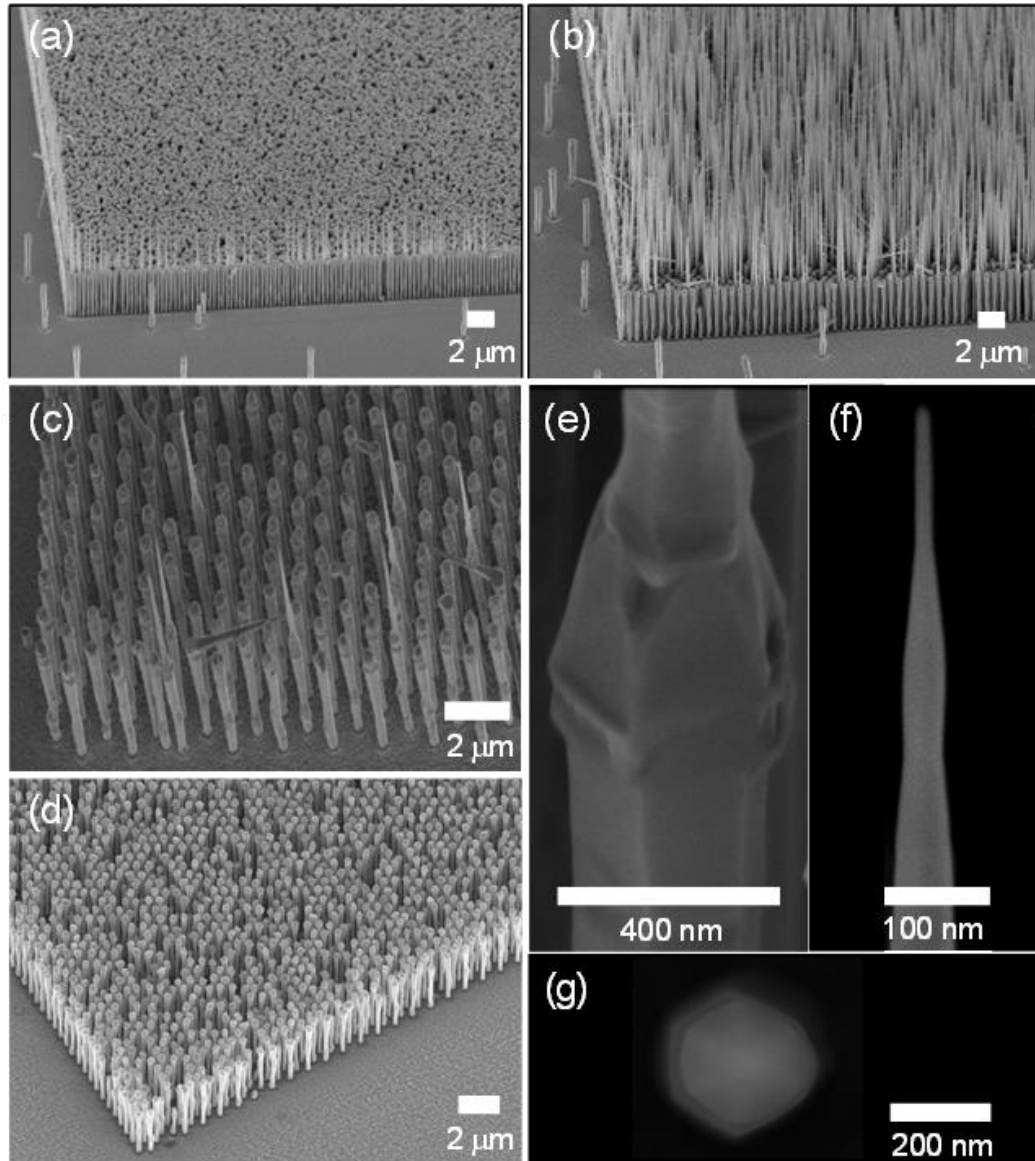


Figure 5.1: Scanning electron microscope (SEM) images (2 kV, 30° tilt) of GaP nanowires. With Te flux, nanoantenna form along the edge for a 360 nm pitch (a), uniformly for a 600 nm pitch (b), and sparsely for a 1000 nm pitch (c). Without Te flux, nanoantenna are not observed as shown by the SEM image for a 600 nm pitch (d). SEM image of a typical transition region (e) and tip (f, g) are shown for a 600 nm pitch with Te flux.

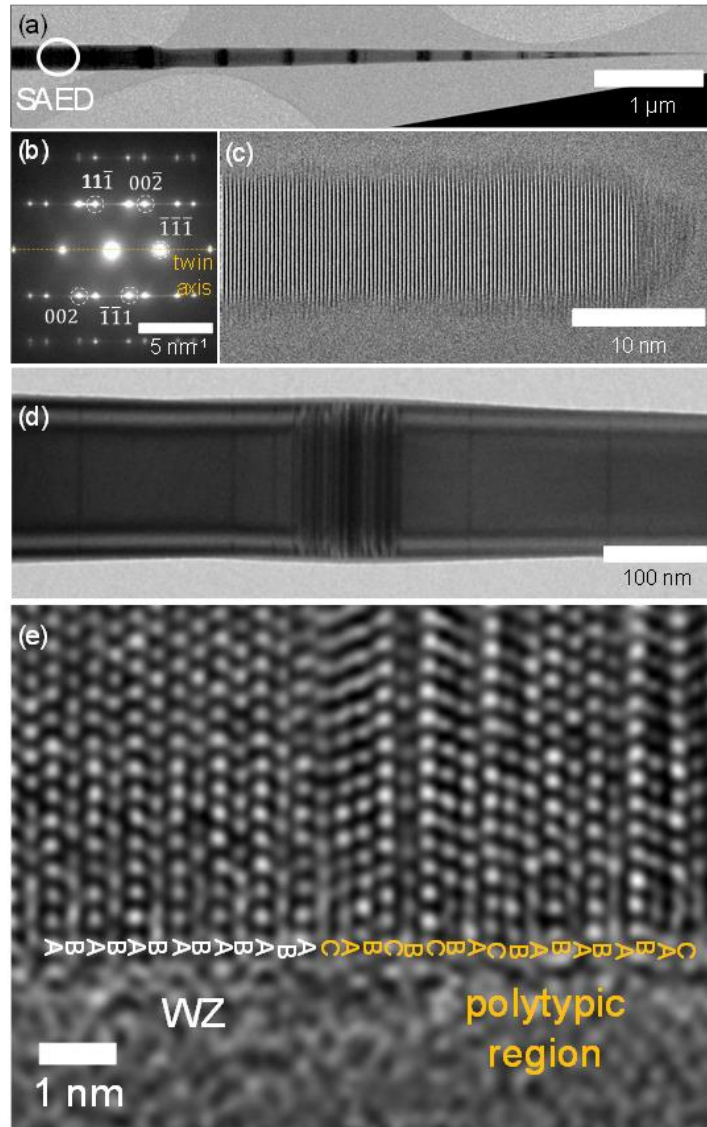


Figure 5.2: Transmission electron microscope (TEM) images of GaP nanowires (NWs). (a) TEM image (120 kV) of a NW showing periodic polytypic regions (dark contrast indicated by red arrows). (b) Selective area electron diffraction pattern of a NW base region (circled in (a)), indicating the twinned zincblende (ZB) crystal structure. (c) High resolution TEM (HRTEM) image (300 kV) of a NW tip, indicating the wurtzite (WZ) crystal structure. (d) TEM image (120 kV) of a polytypic region, coinciding with a slight increase of NW radius. (e) HRTEM image (300 kV) showing the WZ bilayer stacking sequence (ABAB...) below the polytypic region in (d) followed by random stacking (mixed WZ/ZB) in the polytypic region.

5.3 Growth Model

In modeling, we try to understand and quantify the data showing the following trends. First, GaP NWs without the Te doping showed inverse tapering. Positive tapering leading to ultrathin antenna developed only in Te-doped NWs. Figure 5.1e shows the abrupt transition from inverse to positive tapering. Formation of nanoantenna depends on the pitch of the masked pattern. Antenna are dominant for a NW pitch of 600 nm (Figure 5.1b). In dense NW arrays with 360 nm pitch, antenna exist only along the edges of the mask pattern (Figure 5.1a), while in sparse NW arrays with 1000 nm pitch, antenna occur rarely and randomly within the array (Figure 5.1c). Second, the ZB crystal phase of NW bases (Figure 5.2b) is transitioned to the predominantly WZ crystal phase (Figure 5.2c) after the introduction of Te doping. Third, the radius of Te-doped NWs oscillates slightly during growth (Figure 5.1f, Figure 5.2d). The polytypic ZB/WZ regions, defined by a dark contrast in Figure 5.2, correspond to local maxima in radius of the antenna, as shown in Figure 5.2d. Figure 5.3 shows the radius along the doped segment, plotted for two typical NWs, obtained by TEM measurements. It is seen that the polytypic ZB/WZ sections of both NWs correspond to local maxima of their radii, as in Figure 5.2d. Slight oscillations of the NW radius, induced by droplet breathing, and the corresponding phase changes will be elaborated below.

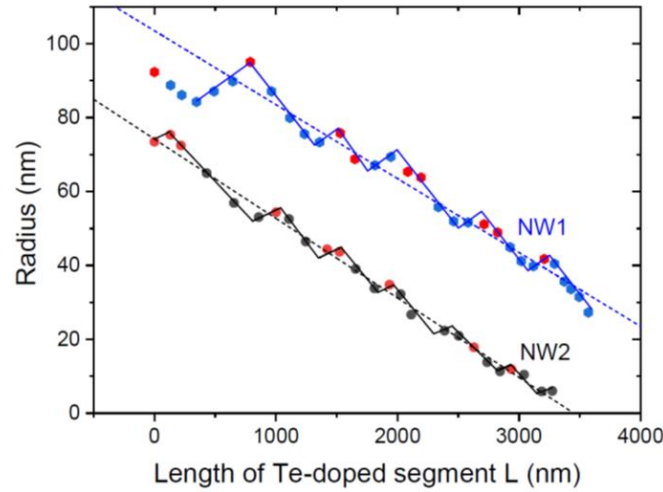


Figure 5.3: Radius of two NWs (NW1 and NW2) versus the length of Te-doped segments (symbols), with the polytypic ZB/WZ regions highlighted in red. The dotted lines are the mean NW radii with the similar tapering angles $\theta_* = 2.29^\circ$ for NW1 and $\theta_* = 2.46^\circ$ for NW2. The solid lines show the NW shapes obtained within the model, with the narrowing angle θ_n around 2.6° and the widening angle θ_w around 1° .

It is well known that the axial growth rate of self-assisted VLS III-V NWs is determined by the atomic flux of the group V element entering the Ga droplet, while the volume of the droplet is non-stationary and may either swell or shrink depending on the V/III flux ratio and the diffusion length of group III adatoms on the NW sidewalls [22], [59], [79], [80], [81], [82]. III-V NWs grow with a uniform radius only under the stationary conditions with a time-independent droplet volume, where the group V input into the droplet is equalized by the vapor flux of group III atoms plus the diffusion flux of group III adatoms into the droplet [22], [79], [82]. Otherwise, the Ga droplet volume swells or shrinks to reach the stationary state [22], [59], [79], [80]. Undoped Ga-assisted GaP NWs exhibit two stable contact angles β_{max} and β_{min} around 123° and 90° , respectively [80], [81], [82]. The large stable contact angle of $\sim 123^\circ$ corresponds to pure ZB crystal phase and inverse tapered

GaP NWs under group III rich conditions [81], as in our case. The WZ crystal phase is observed in a narrow range of contact angles between $\sim 90^\circ$ and $\sim 105^\circ$, with vertical sidewalls [80], [82]. The small stable contact angle of around 90° corresponds to positive NW tapering and the WZ-to-ZB phase transition with the predominant WZ phase [25], [26]. Similar behavior is observed for Ga-assisted GaAs NWs, with the WZ phase corresponding to the extended range of constant angles between $\sim 90^\circ$ and 125° [25], [26], [59]. In particular, the WZ phase has been seen in the thin (~ 10 nm in radius) tops of GaAs NWs grown under enhanced V/III flux ratio [59].

We now consider the morphological evolution of the Te-doped NW segments. At a time-independent droplet contact angle $\beta_* = \beta_{max}$ or $\beta_* = \beta_{min}$, the droplet base radius, which equals the radius of the NW top R_* , is related to the NW length L according to [59], [79], [81]

$$L = \frac{F_{53}}{\varepsilon(F_{53} - 1)} \left[R_*(0) - R_* + R_s \ln \left(\frac{R_*(0) - R_s}{R_* - R_s} \right) \right]. \quad (5.1)$$

Here, $R_*(0)$ is the NW radius at $L = 0$, F_{53} is the ratio of vapor P and Ga fluxes entering the droplet (the atomic V/III ratio), $\varepsilon = \Omega_{Ga} / [\Omega_{GaP} f(\beta_*)]$, with $\Omega_{Ga} = 0.02$ nm³ as the elementary volume of liquid Ga, $\Omega_{GaP} = 0.04$ nm³ as the elementary volume of solid GaP, and $f(\beta_*)$ as the geometrical function of the contact angle given in Refs. [59], [79], [81]. At low rates of radial growth, the NW morphology simply repeats the evolution of the top radius, and Equation 5.1 describes the observed NW morphology $R_*(L)$. Our GaP NWs show very pronounced negative or positive tapering. This should correspond to the

effective absence of the radial growth, particularly for ultrathin nanoantenna, which is neglected in the model. Figure 5.4 shows how the NW morphology changes with R_s . The NW shape is non-linear and less tapered for larger R_s , and becomes linear and more tapered at $R_s \rightarrow 0$. There is not much difference between the curves at $R_s = 1.5$ nm and $R_s \rightarrow 0$ apart from the very last stage. However, the stable radius of 1.5 nm is too small for any practical purposes because the droplet will most probably disappear before nanoantenna formation. Achieving ultra-thin nanoantenna with radius of about 5 nm requires a careful adjustment of the V/III balance at the NW tips. Our antenna grew under P-rich conditions, where some NWs finally become nanoneedles and Ga droplets are lost by the end of growth. We are very close to the regime where the stable radius of the nanoantenna is so small that the droplets are fully consumed under the excessive P flux in many NWs, which explains the low nanoantenna yield.

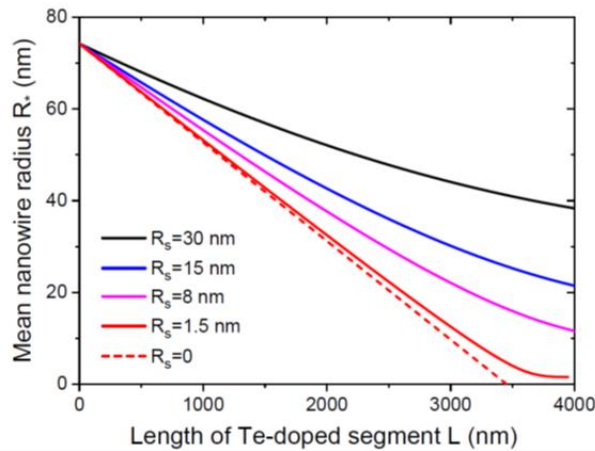


Figure 5.4: Mean radii R_* versus the length of Te-doped NW segment obtained from Equation 5.1 with $R_*(0) = 74.2$ nm and $\varepsilon(F_{53} - 1) / F_{53} = 0.215$, corresponding to NW2 in Figure 5.3, and different R_s shown in the legend. The dependences become more linear for smaller R_s and tend to the experimentally observed linear shape at $R_s \rightarrow 0$, shown by the dashed line.

The stable radius of the NW top R_s is determined by the well-known expression [59], [81]:

$$R_s = \frac{2\lambda_3 \sin\alpha_3}{\pi\chi_3(F_{53} - 1)}. \quad (5.2)$$

Here, α_3 is the Ga beam angle with respect to the substrate normal, λ_3 is the diffusion length of Ga adatoms on the NW sidewalls, and χ_3 is the geometrical function of the VLS growth in MBE given in Ref. [83]. Importantly, both P and Ga fluxes include the growth species which re-emit from the mask surface or diffuse along the NW sidewalls to the top [59], [78], [84]. Therefore, the actual F_{53} ratio of fluxes entering the droplet is generally different from the nominal V/III flux ratio in the vapor phase.

The stable radius is reached when the vapor flux of Ga plus the radius-dependent diffusion flux from the NW sidewalls equalize the P vapor flux. According to Equation 5.2, the self-stabilization of the NW radius occurs only at $F_{53} > 1$. Otherwise, the top NW radius increases infinitely due to excessive Ga vapor flux, leading to positive tapering at any time. This growth mode is observed in our inverse tapered undoped NWs. At $F_{53} > 1$, the stable radius decreases for shorter diffusion lengths of Ga and larger F_{53} ratios. This may lead to the droplet shrinking and positive tapering of NWs grown under locally P-rich conditions. Introduction of dopants, such as Zn, Be, and Te, leads to a modification of the NW sidewalls, which often manifests in the formation of TSL ZB III-V NWs restricted by alternating (111)A and (111)B side facets [69], [78], [85]. TSL NWs maintain a time-independent [86] or even increasing [69] mean radius R_* . Our Te-doped GaP NWs show a different morphology, with positive tapering leading to ultrathin antenna, some of which are 5 nm in radius. According to Figure 5.3, the mean NW radii decrease linearly with the

length of Te-doped NW segments, with very similar tapering angles. The linear shape corresponds to the limiting case of $R_s \rightarrow 0$ in Figure 5.4, where Equation 5.1 is reduced to

$$R_*(L) = R_*(0) - L \tan \theta_*, \quad \tan \theta_* = \frac{\varepsilon(F_{53}-1)}{F_{53}}. \quad (5.3)$$

Assuming $\beta_* = 90^\circ$, small tapering angles θ_* (corresponding to $\tan \theta_* \cong 0.02$ for both NWs in Figure 5.3) yield a value of $F_{53} \cong 1.09$.

The linear shape of the nanoantenna at $R_s \rightarrow 0$ should then be observed at negligible diffusion lengths of Ga adatoms λ_3 . We speculate that the accumulation of Te atoms on the NW sidewalls [61] leads to a modification of their structure such that flat (110) planes are changed to the sawtooth facets shown in Figure 5.3. This suppresses Ga impingement onto the NW sidewalls and diffusion into the droplet, because more Ga atoms are captured by the adsorbed Te atoms or simply desorb from the NW sidewalls. Desorption of Ga should be enhanced by Te doping, whose concentration is highest at the NW sidewalls, because Te replaces Ga atoms in solid GaP. On the other hand, formation of the antenna requires that $F_{53} > 1$. Larger P input to the antenna tops enables their rapid growth and shrinking of the droplets. This may explain the observed pitch dependence of the nanoantenna occurrence. In very dense arrays of NWs, a low P flux is received by each NW within the array, yielding $F_{53} < 1$. The antenna structures can only emerge along the edges of the pattern, where P flux re-emitted from the mask surface is larger. In very sparse NW arrays, the re-emitted P flux received by each NW increases. On the other hand, more additional Ga adatoms arrive to the droplets in the absence of the shadowing effect, which is why the F_{53} ratio may again decrease below unity. Accurate estimation of the pitch-

dependent material balance and the corresponding effective V/III ratios requires additional study and is beyond the scope of this work. It is clear, however, that $F_{53} < 1$ in negatively tapered undoped NWs, while in doped NWs the F_{53} value gets very large, which leads to rapid axial growth and positive tapering of the nanoantenna.

According to Refs. [25], [26], [80], the crystal phase of GaP NWs is mainly determined by the droplet contact angle β . Oscillations of the NW radius, shown in Figure 5.3, lead to the occurrence of polytypic ZB/WZ regions around the local maxima of the radius. The latter should correspond to the local minima of the contact angle, where the formation of the ZB stacking is more probable [25]. The mean tapering angles $\theta_* = 2.29^\circ$ for NW1 and $\theta_* = 2.46^\circ$ for NW2 as deduced from the fits in Figure 5.3 are determined by the purely kinetic process of emptying Ga droplets under the excessive P flux, and may not correspond to the preferred surface energy configuration of the NW side facets. Rather, the NW sidewalls are restricted by the two types of facets, as illustrated in Figure 5.5. The narrowing facet makes the angle θ_n to the substrate normal, which is slightly larger than the mean tapering angle θ_* . The widening facet makes the negative angle $-\theta_w$ to the substrate normal, which is why the NW radius increases in the widening sections of the antenna.

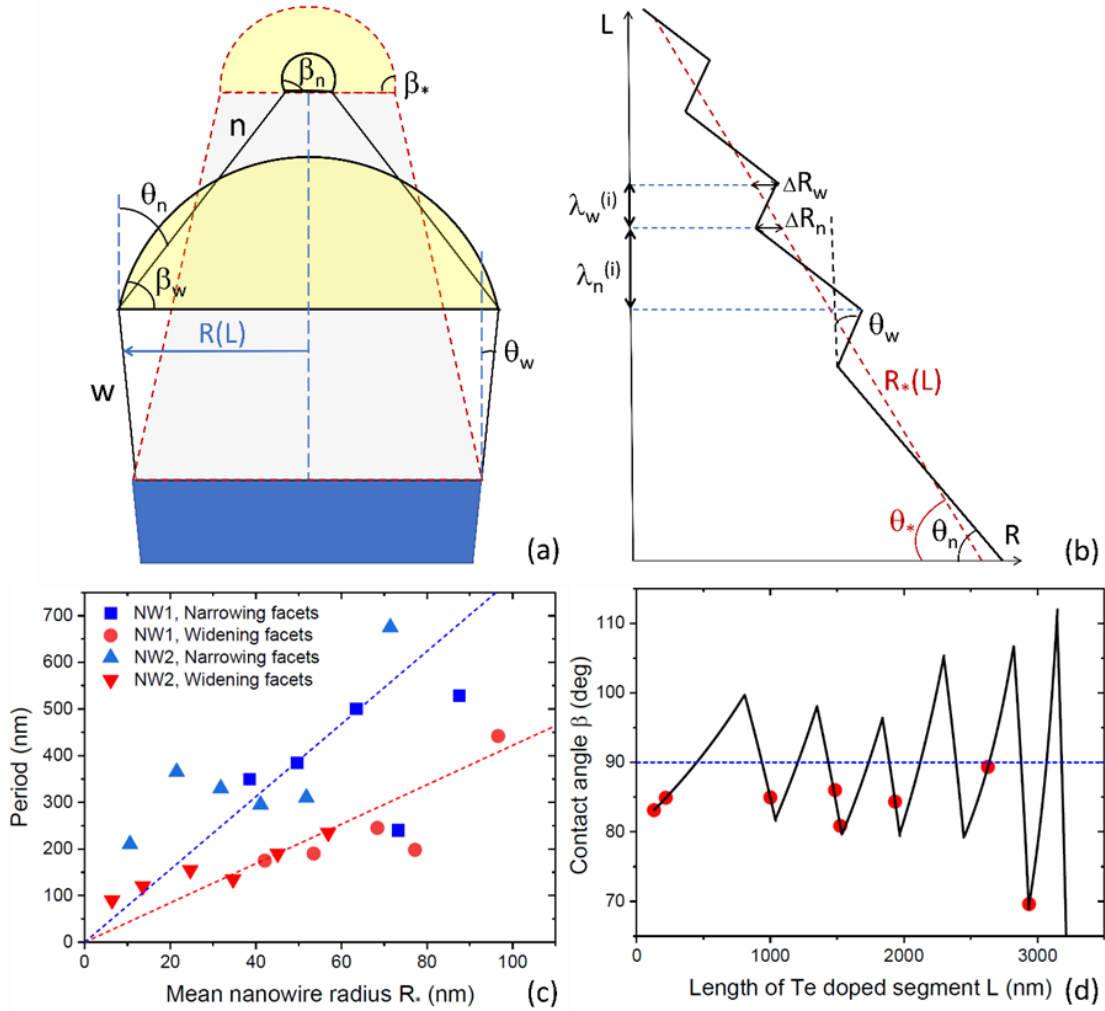


Figure 5.5: Growth model results. (a) Nanoantenna geometry showing the widening (w) and narrowing (n) facets inclined by the angles θ_w and θ_n to the substrate normal. The droplet contact angles in the widening (β_w) and narrowing (β_n) sections are different from the mean contact angle β_* . (b) Sawtooth geometry of tapered nanoantenna, with the lengths of the narrowing and widening sections $\lambda_n^{(i)}$ and $\lambda_w^{(i)}$. $R_*(L)$ is the mean nanowire radius corresponding to the mean tapering angle θ_* , while ΔR_n and ΔR_w are the radius deviations in the narrowing and widening sections of the nanoantenna. (c) Periods of the narrowing and widening sections in NW1 and NW2, corresponding to the morphologies shown in Figure 5.3 (symbols) and their linear fits (dashed lines). (d) Oscillations of the droplet contact angle given by Eq. (5.6) at $\beta_* = 90^\circ$, corresponding to the radius oscillations shown in Figure 5.3 for NW2. The amplitude of these oscillations increases for smaller radius of the nanoantenna. The red dots correspond to the areas of mixed zincblende/wurtzite phases.

Both θ_n and θ_w angles are very small, but not equal to the mean tapering angle θ_* . This leads to the oscillations of the NW radii seen in Figure 5.3 for both NWs, and induces the corresponding oscillations of the droplet contact angle. We cannot identify the exact crystallographic orientations of the side facets of the nanoantenna. The small narrowing and widening angles should correspond to high-index planes of the WZ or polytypic ZB/WZ GaP, probably influenced by step flow on the NW sidewalls. In any case, the data shown in Figure 5.3 reveal the oscillations of the NW radii, which can only occur when the two facet orientations defined by the angles θ_n and θ_w are preferred to the orientation θ_* . Therefore, we will treat the morphology of the VLS growth interface with the two stable facet orientations using the approach of Refs. [24], [26], [69], [87], generalized to account for the gradually decreasing radius at the top of tapered nanoantenna. The geometry of angular-symmetric sawtooth nanoantenna is illustrated in Figure 5.5a,b. Angular-symmetric geometry allows for analysis of the surface energetics in two-dimensional case [24], [87], which is simpler than the three-dimensional geometry of TSL NWs [61], [86]. The effective surface energies of the VLS growth interface in the narrowing (labeled “n”) and widening (labelled “w”) sections of the nanoantenna are given by [26], [87]

$$\Gamma_n = \frac{\gamma_n}{\cos\theta_n} - (\gamma_d \cos\beta_n + \gamma_i) \tan\theta_n ,$$

$$\Gamma_w = \frac{\gamma_w}{\cos\theta_w} + (\gamma_d \cos\beta_w + \gamma_i) \tan\theta_w .$$
(5.4)

Here, γ_n and γ_w are the effective surface energies of the narrowing and widening facets, γ_d is the surface energy of Ga droplet, and γ_i is the energy of the solid-liquid interface

under the droplet. The droplet contact angles β_n and β_w correspond to the narrowing and widening sections of the nanoantenna, and are different from the mean contact angle β_* .

At $\beta_n = \beta_w = \beta_*$, the two surface energies are equalized: $\Gamma_n = \Gamma_w = \Gamma_*$. Using Equation 5.4, we obtain: $\cos\beta_* = -\gamma_i/\gamma_d + (\gamma_n/\cos\theta_n - \gamma_w/\cos\theta_w)/[\gamma_d(\tan\theta_n + \tan\theta_w)]$, which is reduced to the result of Ref. [69] at $\theta_n = \theta_w$. Substitution of this β_* into Equation 5.4 gives the corresponding surface energy Γ_* . The mean contact angle β_* should be close to the small stable contact angle of $\cong 90^\circ$ according to the discussion above. As in Refs. [69], [87], we assume that the droplet volume in the narrowing and widening sections of the nanoantenna equals the mean droplet volume V_* at a given mean radius R_* and mean contact angle β_* . Then the deviation of the contact angle $\Delta\beta = \beta - \beta_*$ for both narrowing and widening sections can be related to the measurable deviation of the NW radius $\Delta R = R - R_*$ according to

$$\Delta\beta = -\frac{\Delta R}{R_*} \sin\beta_*(2 + \cos\beta_*). \quad (5.5)$$

The additional surface energies of the narrowing and widening facets, $\Delta\Gamma_n = \Gamma_n - \Gamma_*$ and $\Delta\Gamma_w = \Gamma_w - \Gamma_*$, are given by

$$\Delta\Gamma_n = \gamma_d \tan\theta_n \sin\beta_* \Delta\beta_n, \Delta\Gamma_w = -\gamma_d \tan\theta_w \sin\beta_* \Delta\beta_w. \quad (5.6)$$

According to Ref. [87], the narrowing facet is converged to widening and vice versa when the extra energies of the two facets reach the critical energy Γ_c which is required to introduce an edge: $\Delta\Gamma_n = \Gamma_c$ and $\Delta\Gamma_w = \Gamma_c$. Using Equation 5.6 and relating $\Delta\beta$ to

ΔR according to Equation 5.5, we obtain the maximum deviations of the radii in the narrowing and widening sections in the form

$$\Delta R_n^c = \frac{\Gamma_c}{\gamma_d \tan \theta_n \sin^2 \beta_* (2 + \cos \beta_*)} R_* = a_n R_*, \quad (5.7)$$

$$\Delta R_w^c = \frac{\Gamma_c}{\gamma_d \tan \theta_w \sin^2 \beta_* (2 + \cos \beta_*)} R_* = a_w R_*.$$

With the known tapering angles in the narrowing and widening sections, the NW morphology is given by

$$R_n = (1 + a_w) R_* (L_i) - x \tan \theta_n,$$

$$L_k \leq x \leq L_k + \lambda_n^{(i)},$$

(5.8)

$$R_w = (1 - a_n) R_* (L_i + \lambda_n^{(k)}) + x \tan \theta_w,$$

$$L_k + \lambda_n^{(k)} \leq x \leq L_k + \lambda_n^{(k)} + \lambda_w^{(k)}$$

Here, R_n and R_w are the NW radii in the k -th narrowing and widening sections ($k = 0, 1, 2, \dots$) of the nanoantenna as the functions of the distance x along the NW axis.

The narrowing and widening sections start from the NW lengths L_k and $L_k + \lambda_n^{(k)}$, respectively, with $L_k = 0$ corresponding to the NW lengths at the beginning of Te doping.

The NW morphology is now determined by the periods of the narrowing and widening sections $\lambda_n^{(k)}$ and $\lambda_w^{(k)}$. These periods are obtained by equating the radius deviations of the narrowing and widening sections following from Equation 5.8 to their maximum values given by Equation 5.7. The result is obtained in the form

$$\lambda_n^{(k)} = \left[(a_w + a_n)R_*(L_k) + (1 - a_n) \left(R_*(L_k) - R_*(L_k + \lambda_n^{(k)}) \right) \right] \cotan\theta_n, \quad (5.9)$$

$$\lambda_w^{(k)} = \left[(a_w + a_n)R_*(L_k + \lambda_n^{(k)}) - (1 + a_w) \left(R_*(L_k + \lambda_n^{(k)}) - R_*(L_k + \lambda_n^{(k)} + \lambda_w^{(k)}) \right) \right] \cotan\theta_w.$$

These expressions are valid for any NW shape $R_*(L)$. In the case of linear tapering given by Equation 5.3 and Equation 5.9 are reduced to

$$\lambda_n^{(k)} = \frac{(a_w + a_n)\cotan\theta_n}{1 - (1 - a_n)\cotan\theta_n\tan\theta_*} R_*(L_k), \quad (5.10)$$

$$\lambda_w^{(k)} = \frac{(a_w + a_n)\cotan\theta_w}{1 + (1 + a_w)\cotan\theta_w\tan\theta_*} R_*(L_k + \lambda_n^{(k)}).$$

Therefore, the periods of the narrowing and widening sections of the nanoantenna are proportional to the mean NW radii $R_*(L)$ from which they start. This result is similar to Refs. [69], [87], where it was argued that NW radius is the only parameter of the theory which is homogeneous to length.

Lines in Figure 5.3 show the fits of the NW1 and NW2 morphologies obtained from Equation 5.8. The average narrowing angle θ_n was 2.6° and the average widening angle θ_w was 1° in both cases, although we allowed for slight variations of these angles with the NW length to obtain the best fits to the measured shapes. Small angles of the narrowing and widening facets lead to the extremely low value of the critical energy Γ_c in Equation 5.7. Indeed, oscillations of the NW radius with the amplitudes $\Delta R/R_* \sim 0.05$ and

$\tan\theta \sim 0.01$ for both facets require that $\Gamma_c/\gamma_d \sim 5 \times 10^{-4}$, which yields $\Gamma_c \sim 3.5 \times 10^{-4} \text{ J/m}^2$ at $\gamma_d \sim 0.7 \text{ J/m}^2$ for liquid Ga [24], [25]. It seems plausible that the critical energy for introduction of an edge between the two facets with very close orientations is small, and leads to only a slight breathing of the NW radius around R_* . The periods of the narrowing and widening sections obtained from the fits are shown in Figure 5.5c versus the mean NW radius R_* . The tendency for decreasing the oscillation period with the NW radius is clear. The linear dependences of the periods on the NW radius, predicted by Equation 5.10, work reasonably well. However, the scatter of linear fits in Figure 5.5c is quite large. For example, the short second oscillation of the radius of NW1 in Figure 5.3 does not follow the linear trend. This scatter should be due to statistical fluctuations of the growth process. Interestingly, the lengths of the narrowing and widening sections do not seem to converge to zero for very thin tops of the nanoantenna. This may be explained by the influence of ridges separating the facets, whose contribution to the effective surface energy is known to increase for smaller NW radii [88], [89], but totally neglected in Equation 5.4.

Finally, Figure 5.5d shows the oscillations of the droplet constant angle, induced by the radius variations of NW2. These oscillations were obtained from Equation 5.5 assuming $\beta_* = 90^\circ$. As mentioned above, the oscillation period of the NW radius reduces slower than the NW radius itself, which is why the amplitude of the contact angle oscillations increases in thinner nanoantenna. This may lead to instabilities of the droplet position on the NW top. The droplet may slide onto the NW side, which explains the observed kinking of some very thin nanoantenna observed in Figure 5.1a-c. The polytypic ZB/WZ GaP

structures shown in Figure 5.5d are formed around the local maxima of the NW radius. The corresponding contact angles of Ga droplet are systematically smaller than 90° . This is consistent with in situ observations of Ref. [25] and confirm the importance of the contact angle for the crystal phase transitions in III-V NWs.

In conclusion, the transition from inverse to positive tapering and rapid growth of GaP nanoantenna is attributed to the suppression of surface diffusion of Ga adatoms on the NW sidewalls by Te dopant, which changes the NW growth conditions from Ga-rich to P-rich. The linear decrease of the mean radius of the nanoantenna with its length corresponds to an almost negligible Ga diffusion on the corrugated NW sidewalls. Positive NW tapering due to droplet shrinking, which leads to ultra-thin tops, is different from tapering due to shell growth around the NW core [90], [91], where the NW diameter increases away from the top and the NW top itself maintains a constant radius. Quasi-periodic oscillations of the NW radius are attributed to the two stable orientations of the narrowing and widening sidewall facets. The model provides the direct relationship between the radius modulations and the oscillations of the droplet contact angle. The latter oscillates around the mean value, which is close to the small stable contact angle observed previously in Ga-assisted GaP and GaAs NWs [25], [26], [59]. Larger contact angles in the narrowing sections yield pure WZ phase of the nanoantenna. Smaller contact angles around the local maxima of the radius favor the ZB stacking, consistent with the earlier findings [25]. This explains the occurrence of polytypic ZB/WZ structures in the sawtooth Te-doped antenna. The droplet breathing effect is enhanced in thin tips of the nanoantenna, which may lead to the droplet instabilities and termination of the Ga-assisted VLS growth. Nevertheless, the obtained

nanoantenna with the radii as low as 5 nm are thinner than all other III-V NWs grown by MBE [25], [59], [81], and on par with the 5 nm radius ZB GaAs NWs grown by Au-assisted HVPE [60].

Chapter 6: Optical Study of Ultrathin Te-Doped GaP Nanoantenna

6.1 Introduction

Semiconductor NWs are pseudo one-dimensional crystals and exhibit optical properties that often deviate from their bulk counterparts, motivating their optical study. In this chapter, we investigate the optical properties of GaP NWs using PL, CL, and Raman spectroscopy.

The optical properties of GaP NWs have been investigated in a limited capacity. Available data suggests spectral features depend significantly on crystal structure, defects, and incorporated impurities such as dopants. While bulk GaP uniquely adopts the cubic ZB crystal structure, GaP crystals grown as NWs may prefer the hexagonal WZ crystal structure under certain growth conditions. The existence of ZB or WZ will be reflected in any optical spectrum since band structure is ultimately determined by crystal structure. GaP in the ZB phase is well known to have an indirect bandgap measuring around 2.34 eV at 4 K [92]; however, WZ GaP is expected to have a direct bandgap [93]. The direct bandgap of pure WZ GaP NWs has been measured to be approximately 2.19 eV at 4 K [54], [94].

NWs are susceptible to stacking faults during growth. Such planar crystal defects may act as trap states, facilitating new recombination pathways that manifest as peaks in a PL spectrum [54], [57], [94], [95], [96], [97]. Gupta et al. [97] demonstrated that the presence of twin boundaries in a ZB GaP NW introduces shallow trap states for electrons and holes,

enabling excitonic recombination with an energy dependence on the thickness of the twin boundary. Tuning the thickness of the twin boundaries thus enables control over the emission energy. Assali et al. [75] employed a similar principle to tune the emission energy of crystal-phase-defined quantum wells in GaP NWs, leveraging the type II heterostructure formed between ZB and WZ phases that can be used to confine either electrons or holes.

Impurities such as dopants incorporated during growth may also behave as recombination centers, influencing the PL spectrum [98], [99], [100], [101], [102], [103], [104]. Notably, Seo et al. [104] resolved the PL spectrum of N-doped ZB GaP NWs. They identified sharp emission lines assigned to excitons bound to N atoms embedded in the GaP matrix as well as multiple peaks attributed to excitons bound to N atom pairs and their respective phonon replicas.

As discussed in Chapter 5, we have grown self-assisted Be+Te-doped GaP NWs by MBE that exhibit crystal phase transitions as well as strong positive tapering to radii as low as 5 nm—a record for III-V NWs grown using the VLS mechanism by MBE (see Figure 1.3). The unique morphology of our GaP NWs differ from those previously studied by optical techniques, motivating the present study.

6.2 Optical Characterization

Be-doped and Be+Te-doped GaP NWs were characterized by PL according to the methods described in Section 4.3.1. The obtained spectra are plotted in Figure 6.1. Figure 6.1a,b show the data for the Be-doped and Be+Te-doped NWs, respectively. The red curve represents the raw data while the blue curve is the spectrum after subtracting the

background. A background spectrum (orange) was measured by collecting light scattered by the Si substrate without any interfering NWs. It is suspected that the primary background contribution is from parasitic light during data collection. Notably, the set of peaks below ~ 2.05 eV and the sharp peak at ~ 2.27 eV vanish after background subtraction.

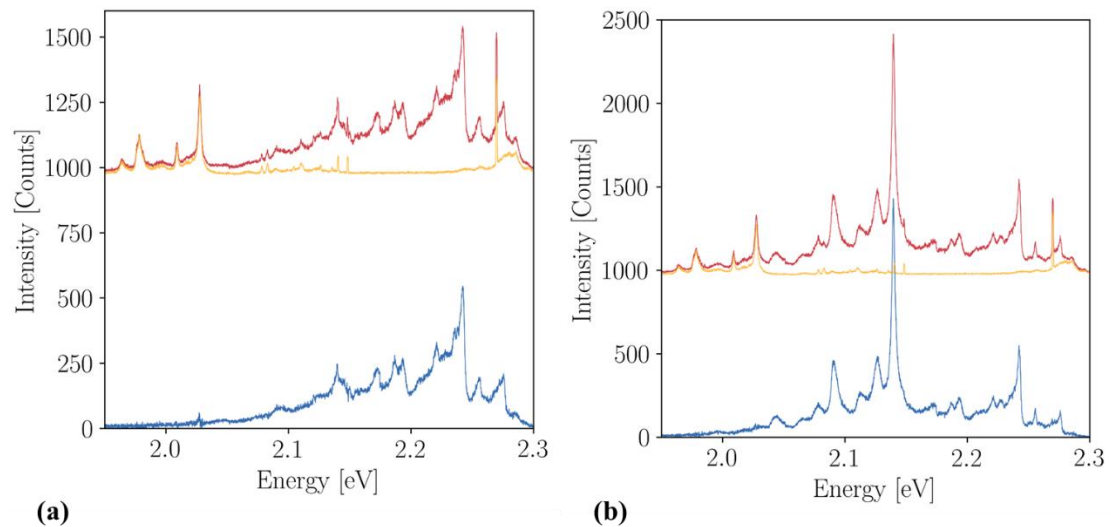


Figure 6.1: Unmodified (red) and background subtracted (blue) photoluminescence spectra (10 K) for (a) the Be-doped GaP nanowires and (b) the Be+Te-doped GaP nanowires. The orange curve is the background spectrum.

Figure 6.2 compares the two spectra after background subtraction. Strikingly, both spectra appear to share the same set of peaks; however, the emission from the Be+Te-doped sample is more intense below ~ 2.15 eV while the emission from the Be-doped sample is more intense above ~ 2.15 eV. We expect that the differences in the PL spectra reflect the difference in crystal structure between samples.

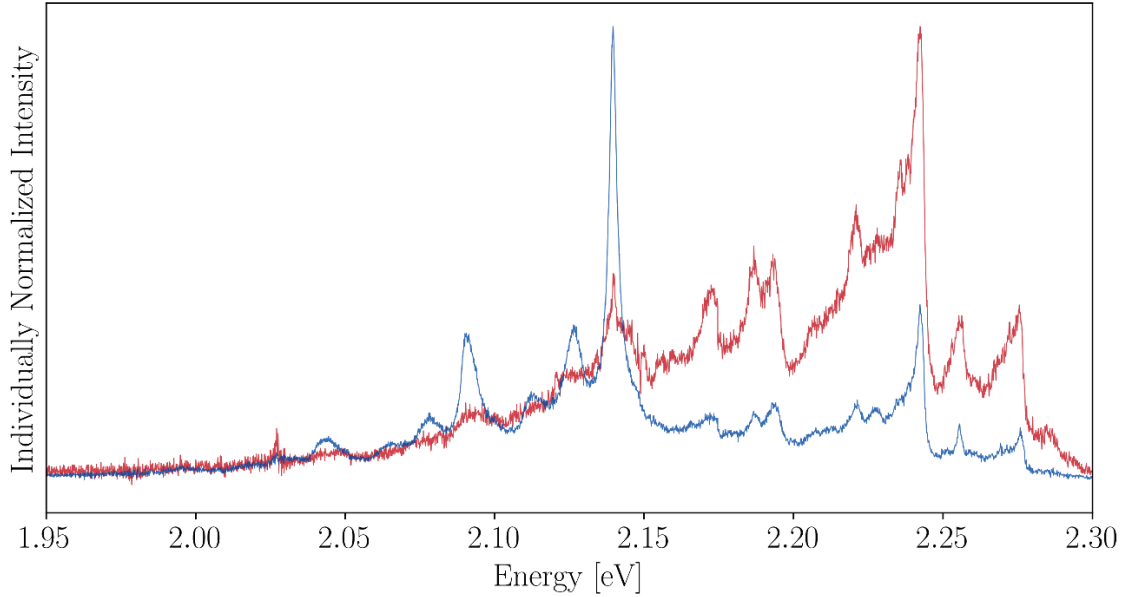


Figure 6.2: Background subtracted and individually normalized photoluminescence spectra (10 K) for the Be-doped (red) and Be+Te-doped (blue) GaP nanowires.

Theoretical band structure calculations predict a decrease in the fundamental bandgap of GaP when the crystal structure is changed from ZB to WZ [93]. Furthermore, the minimum in the conduction band and maximum in the valence band are both predicted at the Γ -point in WZ GaP, resulting in a direct $\Gamma_{9v} - \Gamma_{8c}$ bandgap reported between 2.18 eV and 2.25 eV [93], [105], [106]. The $\Gamma_{9v} - \Gamma_{8c}$ transition is only weakly allowed due to selection rules, but these rules may be relaxed in the presence of defects [54].

In ZB GaP the bandgap is indirect and around 100 meV larger than in WZ GaP. In our spectra we observe an approximate 100 meV separation between the most intense peaks from the Be-doped and Be+Te-doped NWs, which may reflect the dominance of either ZB or WZ. The Be-doped NWs are predominantly ZB while the Be+Te-doped NWs exhibit a

crystal phase transition from ZB to WZ with a periodic ZB/WZ mixing due to the Te-doping. We suspect the PL features below ~ 2.15 eV reflect the WZ crystal structure while the PL peaks above ~ 2.15 eV are due to the ZB crystal structure. The WZ peaks are more intense from the Be+Te-doped NWs because WZ is the predominant crystal phase; conversely, the ZB peaks are more intense from the Be-doped NWs because ZB is the predominant crystal phase. The Be-doped NWs still exhibit WZ peaks because of the high density of stacking faults in the ZB phase, producing effective WZ stacking sequences.

The same NWs were investigated by CL according to methods described in Section 4.3.2. Spatially resolved CL spectra shown in Figure 6.3 reaffirm the crystal phase dependence observed in our PL measurements. A transition from ZB to WZ is evident in Figure 6.3a through the analysis of CL spectra obtained from the base segment (orange), transition region (blue), and antenna (red). The transition from a ZB to WZ CL signal is in direct agreement with crystal phase transition data obtained using HRTEM in Chapter 5. Without Te-doping there is no crystal phase transition from ZB to WZ and so CL features below ~ 2.15 eV are suppressed (Figure 6.3b).

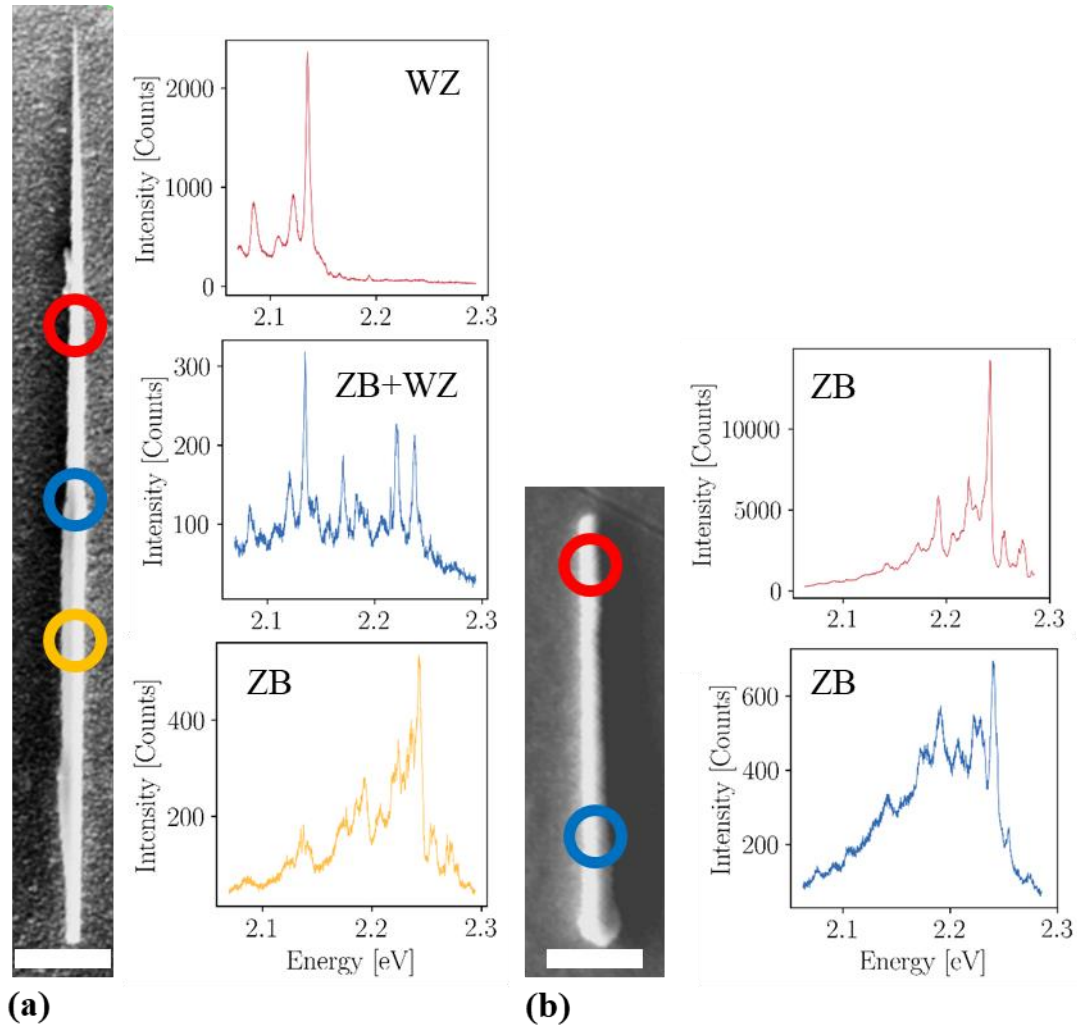


Figure 6.3: Spatially resolved cathodoluminescence measurements (10 K) of (a) Be+Te-doped and (b) Be-doped GaP nanowires. Color-coded circles on the scanning electron microscope images indicate the location of origin for each spectrum. The scale bars are 1 μm .

Crystal phase transitions were also deduced by Raman data obtained according to methods described in Section 4.3.3. Figure 6.4 shows four Raman spectra collected from a scan along the length of a Be+Te-doped GaP NW. The spectra labelled 1 and 2 are from the ZB regime and the spectra labelled 3 and 4 originate from the predominantly WZ nanoantenna

regime. All spectra exhibit expected peaks from the TO ($\sim 364 \text{ cm}^{-1}$) and LO ($\sim 401 \text{ cm}^{-1}$) GaP phonon modes; however, only spectra from the nanoantenna possess peaks from the EL 2 ($\sim 78 \text{ cm}^{-1}$) and EH 2 ($\sim 356 \text{ cm}^{-1}$) phonon modes characteristic of WZ GaP (see Table 3.1). The EL 2 mode appears as a small peak (inset in Figure 6.4) while the EH 2 mode appears as a shoulder to the TO peak. The NW diameter near the tip is small and so the Raman intensity of spectrum 4 is heavily suppressed relative to the other spectra. Note that the peak above 500 cm^{-1} originates from the Si substrate.

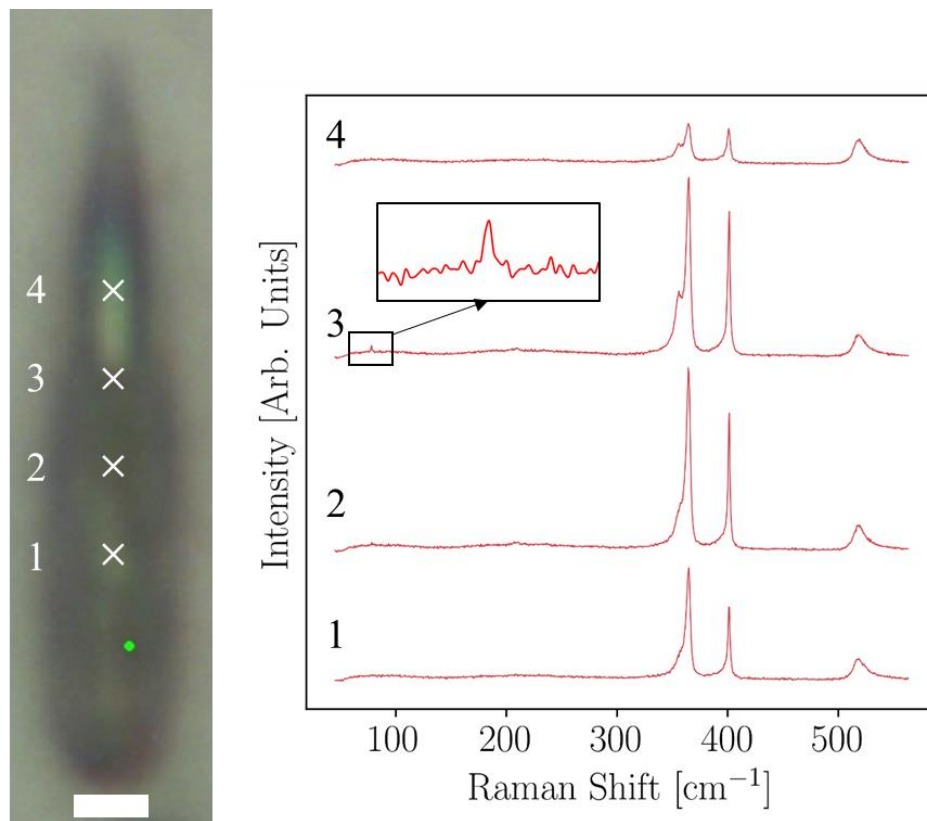


Figure 6.4: Spatially resolved Raman data from a Be+Te-doped GaP nanowire. The numbered \times s on the optical microscope image indicate the measurement location of the corresponding spectrum shown in the cascade plot. The scale bar is $1 \mu\text{m}$.

6.3 Proposed Model

In modelling, we attempt to explain the origin of the PL peaks above and below 2.15 eV, which we have argued derive from the WZ and ZB crystal structures, respectively. First, our PL data in the WZ regime agrees well with work conducted by Assali et al. [54] on pure WZ GaP NWs. In their work, they observed a sharp peak at 2.140 eV characteristic of a bound exciton and attributed lower energy peaks to its phonon replicas. Similar observations have also recently been published by Kang et al. [57], supporting the conclusion that these peaks originate from WZ GaP.

Figure 6.5a shows the PL spectrum of the Be+Te-doped sample in the WZ regime with the characteristic peaks labelled A-G. Peak G originates from the recombination of a bound exciton and the other peaks are its phonon replicas determined by the energies of the TO, LO, and transverse acoustical (TA) modes. Based on our Raman measurements, the LO and TO modes have corresponding energies ~ 50 meV and ~ 45 meV, respectively. The TA mode has a small energy reported to be around 11 meV [54]. Figure 6.5b summarizes the origin of each PL peak. The peak energies agree very well with published data; however, Assali et al. report a ~ 220 μ eV full width half maximum (FWHM) for the excitonic peak while the FWHM of the corresponding peak in our work is around 3 meV. The significant peak broadening might be due to stacking faults that disturb the local band structure, causing a spread in the available excitonic energy transitions [97].

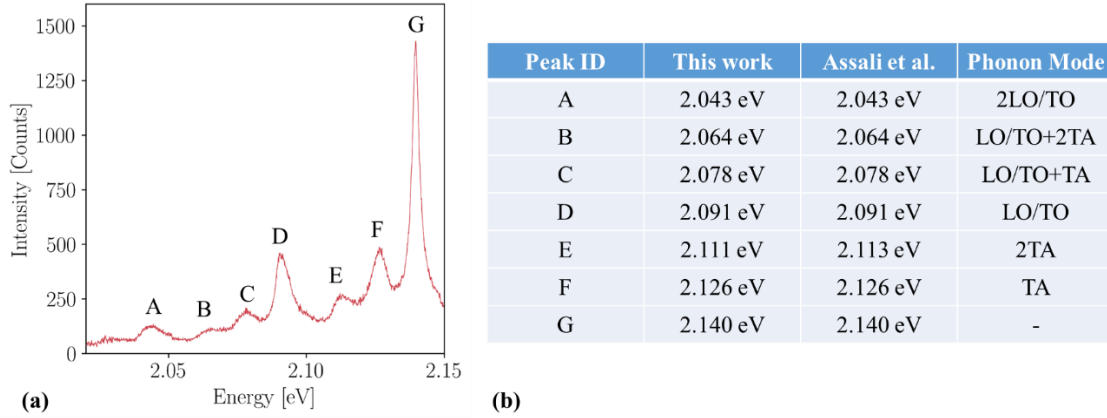


Figure 6.5: Origin of photoluminescence (PL) peaks from wurtzite (WZ) GaP nanowires. (a) PL spectrum (10 K) with characteristic WZ peaks labelled A-G. (b) Measured peak energies compared to those published by Assali et al. [54]. Peak G is from a bound exciton and the other peaks are phonon replicas determined by the energies of the longitudinal optical (LO), transverse optical (TO), and transverse acoustical (TA) modes.

The exciton responsible for Peak G is localized in real-space at a deep center, facilitating recombination beyond the Γ -point where the selection rules are more favorable to radiative recombination [54]. The binding energy of the exciton to the center, $E_{b,WZ}$, is estimated by fitting Equation 3.10 to temperature dependent PL data as shown in Figure 6.6a. Our PL setup is not well equipped for unique measurements at successive temperatures and so the fit is not excellent due to a large (± 2 K) uncertainty in the temperature during each measurement. In any case, we find the exciton binding energy to be around 17 ± 5 meV, which has a similar order of magnitude to the 31 ± 2 meV reported by Assali et al. The overall ionization energy associated with the bound exciton is found by adding the free exciton energy as in Equation 3.9. The free exciton energy for WZ GaP, $E_{x,WZ}$, is approximately 17 meV [54], yielding an overall exciton ionization energy of around 34 meV. This is similar to the 31 ± 3 meV ionization energy reported by Kang et al. for WZ

GaP NWs. A possible radiative channel is illustrated in Figure 6.6b. The exciton is bound to a deep center around 34 meV from the conduction band, facilitating a radiative transmission and emission of a photon with energy 2.140 eV as measured by PL and CL. Such a scheme predicts a $\Gamma_{9v} - \Gamma_{8c}$ direct bandgap measuring around 2.174 eV, which is close to the values reported in literature as discussed in Section 6.2.

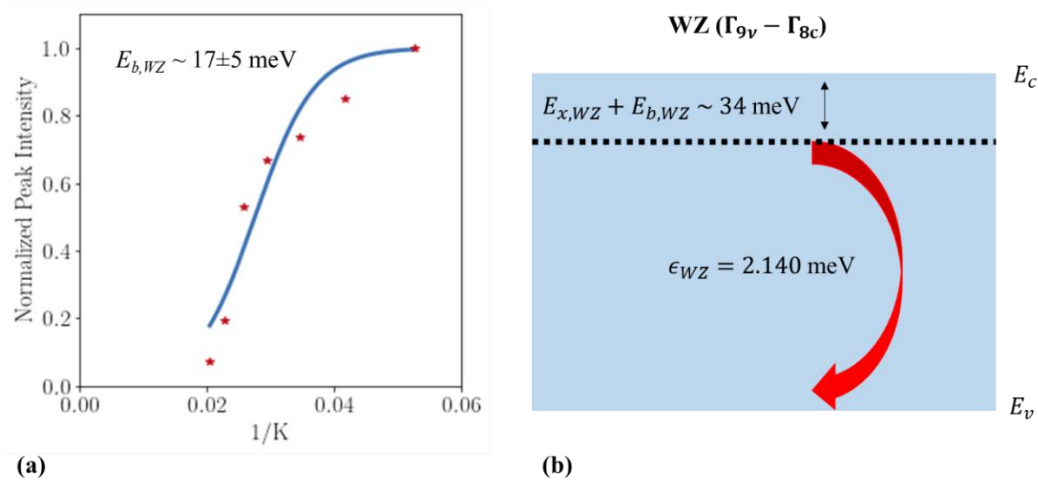


Figure 6.6: Origin of exciton peak in wurtzite (WZ) GaP. (a) Fitting the Arrhenius equation to temperature dependent photoluminescence data predicts the exciton is bound to a deep center with a characteristic energy $E_{b,WZ} = 17 \pm 5$ meV. (b) A possible radiative channel for the exciton bound to a deep center 34 meV from the conduction band edge. $E_{x,WZ}$ is the free exciton binding energy for WZ GaP.

Our PL data in the ZB regime is more difficult to explain. The optical properties of bulk GaP have been studied [98], [99], [100], [101], [107]; however, there is little published work which examines the PL spectrum from ZB GaP NWs. Seo et al. [104] investigated N-doped ZB GaP NWs and showed a spectrum that resembled that of bulk GaP, but was redshifted by ~ 70 meV [108]. The authors estimated a doping level of 10^{18} cm $^{-3}$. Since our NWs are Be and/or Te-doped, we suspected that these dopants may have also contributed

to the peaks we observed. To rule out the role of dopants, we measured the PL spectrum of undoped GaP NWs, shown as a blue curve in Figure 6.7. The undoped spectrum is compared with the Be+Te-doped spectrum (red curve). Both spectra exhibit the same peaks, implying that the Be and Te dopants do not contribute to radiative recombination in our case.

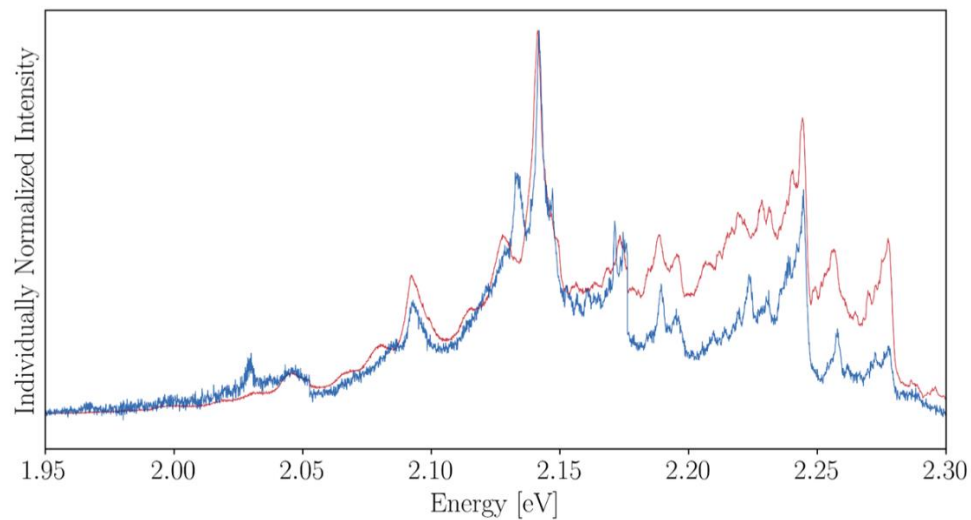


Figure 6.7: Comparison of photoluminescence spectra (10 K) of undoped (blue) and Be+Te-doped (red) GaP nanowires.

To explain the PL signal in the ZB regime, we tentatively attribute the strongest peak around 2.24 eV to the recombination of a bound exciton as was done for the WZ case. This peak consists of at least three closely spaced sub peaks labelled N, O, and P in Figure 6.8a. The other peaks are considered to be phonon replicas based on their energy shifts from the primary peaks as categorized in Figure 6.8b. Some peaks, such as the high energy peaks Q, R, and S, as well as the shoulder K remain unclassified.

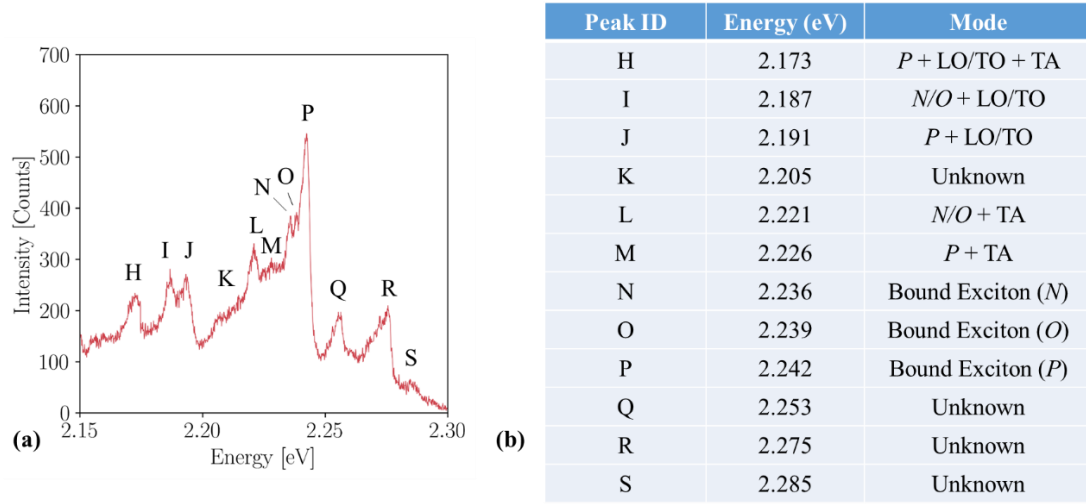


Figure 6.8: Origin of photoluminescence (PL) peaks from zincblende (ZB) GaP nanowires. (a) PL spectrum (10 K) with characteristic ZB peaks labelled H-S. (b) Peaks N, O, and P are attributed to bound excitons and most of the peaks are phonon replicas determined by the energies of the longitudinal optical (LO), transverse optical (TO), and transverse acoustical (TA) modes. The origin of a few peaks remains unknown.

The binding energies of the three exciton peaks were estimated from temperature dependent PL data (Figure 6.9). Each exciton is bound by an energy in the range 18-22 meV, which is roughly the same as the free exciton binding energy in GaP [109].

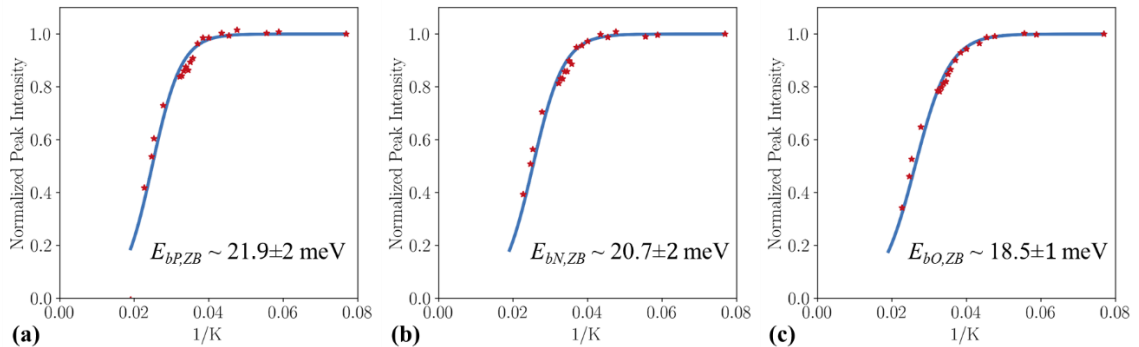


Figure 6.9: Exciton binding energies for the N, O, and P peaks obtained by fitting the Arrhenius equation to temperature dependent photoluminescence data (10 K).

The measured exciton splitting is on the order of a few meV. Dean and Ilegems [98] observed splitting of no-phonon lines in Be-diffused GaP and attributed it to the splitting of states formed by the J-J (spin) coupling of a hole ($J=3/2$) and electron ($J=1/2$). The splitting, outlined in Figure 6.10a, is thought to be caused by an electric field induced by an axial defect in the crystal. This results in several available transitions closely spaced in energy for an exciton bound to this defect.

A possible recombination pathway describing the luminescence in the ZB regime is shown in Figure 6.10b. The ionization energy of the bound exciton is thought to be around 40 meV based on temperature dependent PL data and the known free exciton energy in ZB GaP. There is a small splitting of this level into at least three components due to a field from an axial defect. Validating this splitting would require high quality Zeeman spectroscopy, which is currently unavailable to us; however, it is plausible that some kind of state splitting is present due to the high density of stacking faults we observed in our NWs. Furthermore, the non-uniformity of these faults and the subsequent effects on radiative transition probabilities could explain why the relative intensities of the peaks in the ZB regime appear to fluctuate along the length of the NW, as shown in our CL measurements in Figure 6.3.

Since the $X_{1c} - \Gamma_{15v}$ indirect bandgap is approximately 2.34 eV [92], the measured photon energies around 2.24 eV from exciton recombination are not validated by a transition from the proposed exciton level to the valence band. In particular, if the exciton level has an associated energy of 40 meV (sum of free exciton binding energy in ZB GaP and binding energy calculated from temperature dependent PL), there is ~60 meV missing from the transition. To account for this missing energy, it is possible that there is a second

(unknown) defect level offset around 60 meV from the valence band. Such a deep level defect could be related to the stacking faults in our NWs. Alternatively, we could argue a ~ 60 meV red-shift from the bulk case to the pseudo one-dimensional NW case as in Refs. [103], [104]. The possibility that the PL peaks originate from trap states caused by stacking faults should also be considered, as was used to interpret spectra from GaP NWs in Ref. [97]. Such a theory could be verified by measuring the PL emission from ZB GaP NWs without stacking faults to check if similar peaks arise. In general, more evidence is required to understand the PL and CL in the ZB regime.

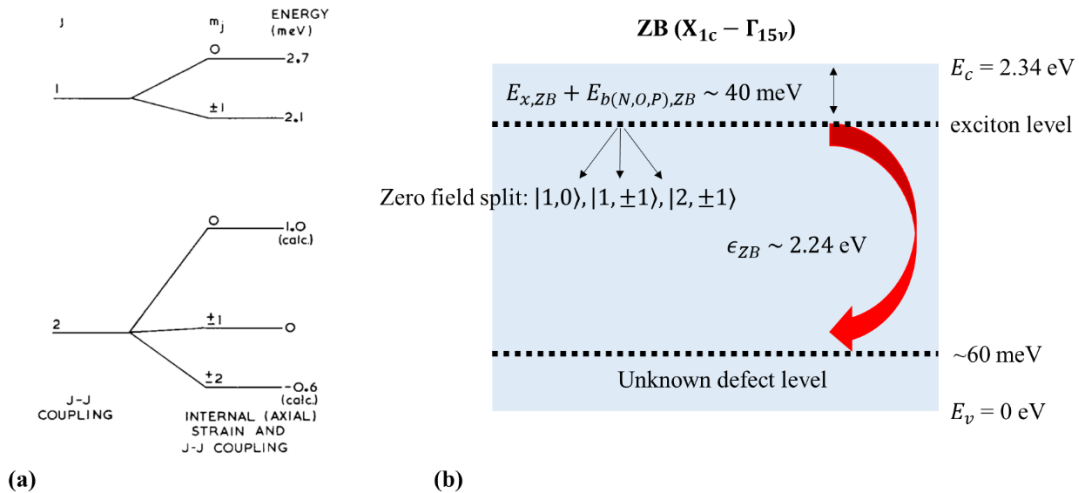


Figure 6.10: Origin of exciton peak in zincblende (ZB) GaP. (a) States formed by binding an exciton to an axial defect in GaP. The states are split by a field induced by the axial defect. Reprinted from [98], copyright 2024, with permission from Elsevier. (b) A possible radiative channel for the exciton bound to an axial defect 40 meV from the conduction band edge. $E_{x,ZB}$ is the free exciton binding energy for ZB GaP.

Chapter 7: Conclusions

We have demonstrated the growth of ultrathin Te-doped GaP NWs using the self-assisted VLS mechanism by MBE. These NWs exhibited crystal phase transitions between ZB and polytypic WZ/ZB correlated with diameter oscillations as well as strong positive tapering to a tip radius as small as 5 nm. We have proposed a growth model to explain the occurrence of these unconventional NW characteristics, which only appear when a Te dopant is incorporated during growth and are most prominent for a 600 nm pitch. Crystal phase transitions from WZ to polytypic WZ/ZB are explained by the oscillation between two energetically stable facet orientations. Widening facets imply smaller contact angles ($<90^\circ$), corresponding to a higher likelihood of ZB stacking. Larger contact angles ($>90^\circ$) favor pure WZ segments. Meanwhile, sharp tapering is attributed to the suppression of Ga atom diffusion along the NW sidewalls caused by Te doping. This results in a higher effective V/III ratio and consequential decrease in NW radius during growth.

We have also optically characterized our NWs using PL, CL, and Raman spectroscopy. We demonstrated the occurrence of unique spectra that reflect the presence of either the WZ or ZB phase. Spatially resolved Raman measurements reveal the expected phonon modes for WZ and ZB GaP. In PL and CL spectra obtained at 10 K, WZ GaP exhibits luminescence below ~ 2.15 eV while ZB GaP has characteristic features above ~ 2.15 eV. The WZ peaks originate from a bound exciton and its phonon replicas, as corroborated by published results. The origin of the ZB peaks are not as clear and require further study. We

have tentatively attributed the spectrum to a bound exciton split by a field originating from axial defects and associated phonon replicas.

Future work can build from the fundamental studies conducted in this thesis. It is recommended that Te-doped GaP NWs be grown under similar conditions to verify the repeatability of the nanoantenna formation we have observed. A systematic growth study (conducted by varying growth rate, growth time, temperature, V/III flux, pattern pitch, etc.) should then be conducted to ascertain the range of conditions yielding nanoantenna. Efforts should also be made to control the crystal phase. Ideally, the crystal phase could be controlled to define axial NWQDs, taking advantage of the small NW radius suitable for quantum confinement. Similarly, it would be beneficial to design chemically defined NWQDs by incorporating heterostructures within the nanoantenna. In this way, high quality NWQDs for quantum information, renewable energy, and communications applications could be manufactured.

References

- [1] N. I. Goktas *et al.*, “Nanowires for energy: A review,” *Applied Physics Reviews*, vol. 5, no. 4, p. 041305, Dec. 2018, doi: 10.1063/1.5054842.
- [2] R. R. LaPierre *et al.*, “A review of III–V nanowire infrared photodetectors and sensors,” *J. Phys. D: Appl. Phys.*, vol. 50, no. 12, p. 123001, Feb. 2017, doi: 10.1088/1361-6463/aa5ab3.
- [3] H. Mäntynen *et al.*, “Single-photon sources with quantum dots in III–V nanowires,” *Nanophotonics*, vol. 8, no. 5, pp. 747–769, May 2019, doi: 10.1515/nanoph-2019-0007.
- [4] M. de la Mata *et al.*, “Atomic Scale Strain Relaxation in Axial Semiconductor III–V Nanowire Heterostructures,” *Nano Lett.*, vol. 14, no. 11, pp. 6614–6620, Nov. 2014, doi: 10.1021/nl503273j.
- [5] G. E. Cirlin *et al.*, “Critical diameters and temperature domains for MBE growth of III–V nanowires on lattice mismatched substrates,” *physica status solidi (RRL) – Rapid Research Letters*, vol. 3, no. 4, pp. 112–114, 2009, doi: 10.1002/pssr.200903057.
- [6] E. Diak *et al.*, “Ultrathin Te-Doped GaP Nanoantenna with Crystal Phase Transitions,” *Crystal Growth & Design*, vol. 23, no. 7, pp. 5074–5082, Jul. 2023, doi: 10.1021/acs.cgd.3c00315.
- [7] R. Chen *et al.*, “Thermoelectrics of Nanowires,” *Chem. Rev.*, vol. 119, no. 15, pp. 9260–9302, Aug. 2019, doi: 10.1021/acs.chemrev.8b00627.
- [8] J. Johansson *et al.*, “Recent advances in semiconductor nanowire heterostructures,” *CrystEngComm*, vol. 13, no. 24, pp. 7175–7184, 2011, doi: 10.1039/C1CE05821E.
- [9] C. J. Goosney *et al.*, “InSb nanowires for multispectral infrared detection,” *Semicond. Sci. Technol.*, vol. 34, no. 3, p. 035023, Feb. 2019, doi: 10.1088/1361-6641/ab0476.
- [10] Y. Zhang *et al.*, “III-V nanowires and nanowire optoelectronic devices,” *Journal of Physics D: Applied Physics*, vol. 48, no. 46, Oct. 2015, doi: 10.1088/0022-3727/48/46/463001.
- [11] R. S. Wagner *et al.*, “Vapor-liquid-solid mechanism of single crystal growth,” *Applied Physics Letters*, vol. 4, no. 5, pp. 89–90, 1964, doi: 10.1063/1.1753975.
- [12] J. Su *et al.*, “Catalytic growth of group III-nitride nanowires and nanostructures by metalorganic chemical vapor deposition,” *Applied Physics Letters*, vol. 86, no. 1, p. 013105, Dec. 2004, doi: 10.1063/1.1843281.
- [13] E. Gil *et al.*, “Growth of long III-As NWs by hydride vapor phase epitaxy,” *Nanotechnology*, vol. 32, no. 16, p. 162002, Jan. 2021, doi: 10.1088/1361-6528/abdb14.
- [14] J. P. Boulanger *et al.*, “Patterned gold-assisted growth of GaP nanowires on Si,” *Semicond. Sci. Technol.*, vol. 27, no. 3, p. 035002, Jan. 2012, doi: 10.1088/0268-1242/27/3/035002.
- [15] K. Tomioka *et al.*, “Selective-area growth of III-V nanowires and their applications,” *Journal of Materials Research*, vol. 26, no. 17, pp. 2127–2141, Sep. 2011, doi: 10.1557/jmr.2011.103.

- [16] S. A. Fortuna *et al.*, “Planar GaAs Nanowires on GaAs (100) Substrates: Self-Aligned, Nearly Twin-Defect Free, and Transfer-Printable,” *Nano Lett.*, vol. 8, no. 12, pp. 4421–4427, Dec. 2008, doi: 10.1021/nl802331m.
- [17] A. Thomas *et al.*, “Analytical model of a nanowire-based betavoltaic device,” *Journal of Applied Physics*, vol. 135, no. 13, p. 134302, Apr. 2024, doi: 10.1063/5.0202949.
- [18] Y. Wu *et al.*, “Direct Observation of Vapor–Liquid–Solid Nanowire Growth,” *J. Am. Chem. Soc.*, vol. 123, no. 13, pp. 3165–3166, Apr. 2001, doi: 10.1021/ja0059084.
- [19] O. Landré *et al.*, “Nucleation mechanism of GaN nanowires grown on (111) Si by molecular beam epitaxy,” *Nanotechnology*, vol. 20, no. 41, p. 415602, Sep. 2009, doi: 10.1088/0957-4484/20/41/415602.
- [20] F. M. Ross, “Controlling nanowire structures through real time growth studies,” *Rep. Prog. Phys.*, vol. 73, no. 11, p. 114501, Oct. 2010, doi: 10.1088/0034-4885/73/11/114501.
- [21] V. G. Dubrovskii, “Chapter One - Theory of VLS Growth of Compound Semiconductors,” in *Semiconductors and Semimetals*, vol. 93, A. F. I. Morral, S. A. Dayeh, and C. Jagadish, Eds., in *Semiconductor Nanowires I*, vol. 93., Elsevier, 2015, pp. 1–78. doi: 10.1016/bs.semsem.2015.09.002.
- [22] J. Tersoff, “Stable Self-Catalyzed Growth of III–V Nanowires,” *Nano Lett.*, vol. 15, no. 10, pp. 6609–6613, Oct. 2015, doi: 10.1021/acs.nanolett.5b02386.
- [23] Y. Zhang *et al.*, “Polarity-driven quasi-3-fold composition symmetry of self-catalyzed III–V–V ternary core-shell nanowires,” *Nano Letters*, vol. 15, no. 5, pp. 3128–3133, May 2015, doi: 10.1021/acs.nanolett.5b00188.
- [24] V. G. Dubrovskii, “Development of Growth Theory for Vapor–Liquid–Solid Nanowires: Contact Angle, Truncated Facets, and Crystal Phase,” *Crystal Growth & Design*, vol. 17, no. 5, pp. 2544–2548, May 2017, doi: 10.1021/acs.cgd.7b00076.
- [25] F. Panciera *et al.*, “Phase Selection in Self-catalyzed GaAs Nanowires,” *Nano Lett.*, vol. 20, no. 3, pp. 1669–1675, Mar. 2020, doi: 10.1021/acs.nanolett.9b04808.
- [26] V. G. Dubrovskii *et al.*, “Classification of the Morphologies and Related Crystal Phases of III–V Nanowires Based on the Surface Energy Analysis,” *J. Phys. Chem. C*, vol. 123, no. 30, pp. 18693–18701, Aug. 2019, doi: 10.1021/acs.jpcc.9b05028.
- [27] S. Assali *et al.*, “Exploring Crystal Phase Switching in GaP Nanowires,” *Nano Lett.*, vol. 15, no. 12, pp. 8062–8069, Dec. 2015, doi: 10.1021/acs.nanolett.5b03484.
- [28] A. Neil W. *et al.*, *Solid State Physics*, 1st ed. Saunders College Publishing, 1976.
- [29] E. D. Minot *et al.*, “Single quantum dot nanowire LEDs,” *Nano Letters*, vol. 7, no. 2, pp. 367–371, Feb. 2007, doi: 10.1021/nl062483w.
- [30] P. Kuyanov *et al.*, “GaAs quantum dots in a GaP nanowire photodetector,” *Nanotechnology*, vol. 29, no. 12, p. 124003, Feb. 2018, doi: 10.1088/1361-6528/aaa92e.
- [31] Y. Arakawa *et al.*, “Progress in quantum-dot single photon sources for quantum information technologies: A broad spectrum overview,” *Applied Physics Reviews*, vol. 7, no. 2, p. 021309, Jun. 2020, doi: 10.1063/5.0010193.

- [32] V. G. Dubrovskii *et al.*, “Factors Influencing the Interfacial Abruptness in Axial III-V Nanowire Heterostructures,” *Crystal Growth and Design*, vol. 16, no. 4, pp. 2019–2023, Apr. 2016, doi: 10.1021/acs.cgd.5b01613.
- [33] C. Jia *et al.*, “Nanowire Electronics: From Nanoscale to Macroscale,” *Chemical Reviews*, vol. 119, no. 15, pp. 9074–9135, Aug. 2019, doi: 10.1021/acs.chemrev.9b00164.
- [34] N. I. Goktas *et al.*, “Conformal Growth of Radial InGaAs Quantum Wells in GaAs Nanowires,” *J. Phys. Chem. Lett.*, vol. 12, no. 4, pp. 1275–1283, Feb. 2021, doi: 10.1021/acs.jpcclett.0c03712.
- [35] A. D. Yoffe, “Low-dimensional systems: quantum size effects and electronic properties of semiconductor microcrystallites (zero-dimensional systems) and some quasi-two-dimensional systems,” *Advances in Physics*, vol. 42, no. 2, pp. 173–262, Apr. 1993, doi: 10.1080/00018739300101484.
- [36] G. Liao *et al.*, “Electronic Structures of Free-Standing Nanowires made from Indirect Bandgap Semiconductor Gallium Phosphide,” *Sci Rep*, vol. 6, no. 1, Art. no. 1, Jun. 2016, doi: 10.1038/srep28240.
- [37] H. Taleb *et al.*, “Homogeneous and inhomogeneous broadening effects on static and dynamic responses of quantum-dot semiconductor optical amplifiers,” *Front. Optoelectron.*, vol. 5, no. 4, pp. 445–456, Dec. 2012, doi: 10.1007/s12200-012-0288-4.
- [38] P. Lodahl *et al.*, “Interfacing single photons and single quantum dots with photonic nanostructures,” *Rev. Mod. Phys.*, vol. 87, no. 2, pp. 347–400, May 2015, doi: 10.1103/RevModPhys.87.347.
- [39] M. Sinusia Lozano *et al.*, “Epitaxial growth of crystal phase quantum dots in III–V semiconductor nanowires,” *Nanoscale Advances*, vol. 5, no. 7, pp. 1890–1909, 2023, doi: 10.1039/D2NA00956K.
- [40] M. de la Mata *et al.*, “A review of MBE grown 0D, 1D and 2D quantum structures in a nanowire,” *J. Mater. Chem. C*, vol. 1, no. 28, pp. 4300–4312, Jun. 2013, doi: 10.1039/C3TC30556B.
- [41] H. Arab *et al.*, “Recent advances in nanowire quantum dot (NWQD) single-photon emitters,” *Quantum Inf Process*, vol. 19, no. 2, p. 44, Dec. 2019, doi: 10.1007/s11128-019-2542-9.
- [42] G. Priante *et al.*, “Sharpening the Interfaces of Axial Heterostructures in Self-Catalyzed AlGaAs Nanowires: Experiment and Theory,” *Nano Lett.*, vol. 16, no. 3, pp. 1917–1924, Mar. 2016, doi: 10.1021/acs.nanolett.5b05121.
- [43] F. Glas, “Comparison of Modeling Strategies for the Growth of Heterostructures in III-V Nanowires,” *Crystal Growth and Design*, vol. 17, no. 9, pp. 4785–4794, Sep. 2017, doi: 10.1021/acs.cgd.7b00732.
- [44] E. D. Leshchenko *et al.*, “Interfacial profile of axial nanowire heterostructures in the nucleation limited regime,” *CrystEngComm*, vol. 24, no. 46, pp. 8052–8059, Oct. 2022, doi: 10.1039/d2ce01337a.
- [45] J. Wu *et al.*, “Defect-Free Self-Catalyzed GaAs/GaAsP Nanowire Quantum Dots Grown on Silicon Substrate,” *Nano Lett.*, vol. 16, no. 1, pp. 504–511, Jan. 2016, doi: 10.1021/acs.nanolett.5b04142.

- [46] P. Yu *et al.*, “Nanowire Quantum Dot Surface Engineering for High Temperature Single Photon Emission,” *ACS Nano*, vol. 13, no. 11, pp. 13492–13500, Nov. 2019, doi: 10.1021/acsnano.9b07204.
- [47] H. A. Fonseka *et al.*, “GaAsP nanowires containing intentional and self-forming quantum dots,” in *Quantum Dots, Nanostructures, and Quantum Materials: Growth, Characterization, and Modeling XVII*, SPIE, Mar. 2020, pp. 37–47. doi: 10.1117/12.2543747.
- [48] M. Asgari *et al.*, “Quantum-Dot Single-Electron Transistors as Thermoelectric Quantum Detectors at Terahertz Frequencies,” *Nano Lett.*, vol. 21, no. 20, pp. 8587–8594, Oct. 2021, doi: 10.1021/acs.nanolett.1c02022.
- [49] Y. Zhang *et al.*, “Defect-Free Axially Stacked GaAs/GaAsP Nanowire Quantum Dots with Strong Carrier Confinement,” *Nano Lett.*, vol. 21, no. 13, pp. 5722–5729, Jul. 2021, doi: 10.1021/acs.nanolett.1c01461.
- [50] T.-Y. Chang *et al.*, “InAsP Quantum Dot-Embedded InP Nanowires toward Silicon Photonic Applications,” *ACS Appl. Mater. Interfaces*, vol. 14, no. 10, pp. 12488–12494, Mar. 2022, doi: 10.1021/acscami.1c21013.
- [51] C. Mead *et al.*, “Detection of Be dopant pairing in VLS grown GaAs nanowires with twinning superlattices,” *Nanotechnology*, vol. 34, no. 38, p. 385701, Jul. 2023, doi: 10.1088/1361-6528/acde84.
- [52] D. B. Williams *et al.*, *Transmission Electron Microscopy*. Boston, MA: Springer US, 2009. doi: 10.1007/978-0-387-76501-3.
- [53] J. I. Pankove *et al.*, “Optical Processes in Semiconductors,” *J. Electrochem. Soc.*, vol. 119, no. 5, p. 156Ca, May 1972, doi: 10.1149/1.2404256.
- [54] S. Assali *et al.*, “Optical study of the band structure of wurtzite GaP nanowires,” *Journal of Applied Physics*, vol. 120, no. 4, p. 044304, Jul. 2016, doi: 10.1063/1.4959147.
- [55] R. Gupta *et al.*, “Surface Optical Phonons in Gallium Phosphide Nanowires,” *Nano Lett.*, vol. 3, no. 12, pp. 1745–1750, Dec. 2003, doi: 10.1021/nl034842i.
- [56] Y. Xiang *et al.*, “Spatially resolved Raman spectroscopy on indium-catalyzed core-shell germanium nanowires: size effects,” *Nanotechnology*, vol. 21, no. 10, p. 105703, Feb. 2010, doi: 10.1088/0957-4484/21/10/105703.
- [57] S. Kang *et al.*, “Gallium Phosphide Nanowires Grown on SiO₂ by Gas-Source Molecular Beam Epitaxy,” *Crystal Growth & Design*, vol. 23, no. 4, pp. 2568–2575, Apr. 2023, doi: 10.1021/acs.cgd.2c01447.
- [58] N. I. Goktas *et al.*, “Doping assessment in GaAs nanowires,” *Nanotechnology*, vol. 29, no. 23, p. 234001, Apr. 2018, doi: 10.1088/1361-6528/aab6f1.
- [59] W. Kim *et al.*, “Bistability of Contact Angle and Its Role in Achieving Quantum-Thin Self-Assisted GaAs nanowires,” *Nano Lett.*, vol. 18, no. 1, pp. 49–57, Jan. 2018, doi: 10.1021/acs.nanolett.7b03126.
- [60] E. Gil *et al.*, “Record Pure Zincblende Phase in GaAs Nanowires down to 5 nm in Radius,” *Nano Lett.*, vol. 14, no. 7, pp. 3938–3944, Jul. 2014, doi: 10.1021/nl501239h.

- [61] W. Kim *et al.*, “Doping challenges and pathways to industrial scalability of III–V nanowire arrays,” *Applied Physics Reviews*, vol. 8, no. 1, p. 011304, Jan. 2021, doi: 10.1063/5.0031549.
- [62] S. A. Dayeh *et al.*, “Progress in doping semiconductor nanowires during growth,” *Materials Science in Semiconductor Processing*, vol. 62, pp. 135–155, May 2017, doi: 10.1016/j.mssp.2016.10.016.
- [63] H. Hijazi *et al.*, “Si Doping of Vapor–Liquid–Solid GaAs Nanowires: n-Type or p-Type?,” *Nano Lett.*, vol. 19, no. 7, pp. 4498–4504, Jul. 2019, doi: 10.1021/acs.nanolett.9b01308.
- [64] V. G. Dubrovskii *et al.*, “Be, Te, and Si Doping of GaAs Nanowires: Theory and Experiment,” *J. Phys. Chem. C*, vol. 124, no. 31, pp. 17299–17307, Aug. 2020, doi: 10.1021/acs.jpcc.0c04061.
- [65] S. Suomalainen *et al.*, “Te-doping of self-catalyzed GaAs nanowires,” *Appl. Phys. Lett.*, vol. 107, no. 1, p. 012101, Jul. 2015, doi: 10.1063/1.4926494.
- [66] M. Orrù *et al.*, “A Roadmap for Controlled and Efficient n-Type Doping of Self-Assisted GaAs Nanowires Grown by Molecular Beam Epitaxy,” *Advanced Functional Materials*, vol. 26, no. 17, pp. 2836–2845, 2016, doi: 10.1002/adfm.201504853.
- [67] C.-H. Song *et al.*, “Morphology Transition of Te-Doped InAs Nanowire on InP(111)B Grown Using MOCVD Method,” *Crystals*, vol. 12, no. 12, Art. no. 12, Dec. 2022, doi: 10.3390/cryst12121846.
- [68] Y. Zhang *et al.*, “Doping of Self-Catalyzed Nanowires under the Influence of Droplets,” *Nano Lett.*, vol. 18, no. 1, pp. 81–87, Jan. 2018, doi: 10.1021/acs.nanolett.7b03366.
- [69] N. Isik Goktas *et al.*, “Formation Mechanism of Twinning Superlattices in Doped GaAs Nanowires,” *Nano Lett.*, vol. 20, no. 5, pp. 3344–3351, May 2020, doi: 10.1021/acs.nanolett.0c00240.
- [70] A. Ghukasyan *et al.*, “Phase Diagram for Twinning Superlattice Te-Doped GaAs Nanowires,” *Nano Lett.*, vol. 22, no. 3, pp. 1345–1349, Feb. 2022, doi: 10.1021/acs.nanolett.1c04680.
- [71] A. Ghukasyan *et al.*, “Thermal transport in twinning superlattice and mixed-phase GaAs nanowires,” *Nanoscale*, vol. 14, no. 17, pp. 6480–6487, May 2022, doi: 10.1039/D2NR00720G.
- [72] A. Ghukasyan *et al.*, “Thermal Conductivity of GaAs Nanowire Arrays Measured by the 3ω Method,” *Nanomaterials*, vol. 12, no. 8, Art. no. 8, Jan. 2022, doi: 10.3390/nano12081288.
- [73] N. Akopian *et al.*, “Crystal Phase Quantum Dots,” *Nano Lett.*, vol. 10, no. 4, pp. 1198–1201, Apr. 2010, doi: 10.1021/nl903534n.
- [74] M. Bouwes Bavinck *et al.*, “Photon Cascade from a Single Crystal Phase Nanowire Quantum Dot,” *Nano Lett.*, vol. 16, no. 2, pp. 1081–1085, Feb. 2016, doi: 10.1021/acs.nanolett.5b04217.
- [75] S. Assali *et al.*, “Crystal Phase Quantum Well Emission with Digital Control,” *Nano Lett.*, vol. 17, no. 10, pp. 6062–6068, Oct. 2017, doi: 10.1021/acs.nanolett.7b02489.

- [76] S. Hertenberger *et al.*, “Growth kinetics in position-controlled and catalyst-free InAs nanowire arrays on Si(111) grown by selective area molecular beam epitaxy,” *Journal of Applied Physics*, vol. 108, no. 11, p. 114316, Dec. 2010, doi: 10.1063/1.3525610.
- [77] S. J. Gibson *et al.*, “Model of patterned self-assisted nanowire growth,” *Nanotechnology*, vol. 25, no. 41, p. 415304, Sep. 2014, doi: 10.1088/0957-4484/25/41/415304.
- [78] M. R. Ramdani *et al.*, “Arsenic Pathways in Self-Catalyzed Growth of GaAs Nanowires,” *Crystal Growth & Design*, vol. 13, no. 1, pp. 91–96, Jan. 2013, doi: 10.1021/cg301167g.
- [79] V. G. Dubrovskii *et al.*, “Self-Equilibration of the Diameter of Ga-Catalyzed GaAs Nanowires,” *Nano Lett.*, vol. 15, no. 8, pp. 5580–5584, Aug. 2015, doi: 10.1021/acs.nanolett.5b02226.
- [80] V. V. Fedorov *et al.*, “Formation of wurtzite sections in self-catalyzed GaP nanowires by droplet consumption,” *Nanotechnology*, vol. 32, no. 49, p. 495601, Sep. 2021, doi: 10.1088/1361-6528/ac20fe.
- [81] E. D. Leshchenko *et al.*, “Tuning the morphology of self-assisted GaP nanowires,” *Nanotechnology*, vol. 29, no. 22, p. 225603, Mar. 2018, doi: 10.1088/1361-6528/aab47b.
- [82] V. G. Dubrovskii *et al.*, “Simultaneous Selective Area Growth of Wurtzite and Zincblende Self-Catalyzed GaAs Nanowires on Silicon,” *Nano Lett.*, vol. 21, no. 7, pp. 3139–3145, Apr. 2021, doi: 10.1021/acs.nanolett.1c00349.
- [83] F. Glas, “Vapor fluxes on the apical droplet during nanowire growth by molecular beam epitaxy,” *physica status solidi (b)*, vol. 247, no. 2, pp. 254–258, 2010, doi: 10.1002/pssb.200945456.
- [84] F. Oehler *et al.*, “Measuring and Modeling the Growth Dynamics of Self-Catalyzed GaP Nanowire Arrays,” *Nano Lett.*, vol. 18, no. 2, pp. 701–708, Feb. 2018, doi: 10.1021/acs.nanolett.7b03695.
- [85] A. Ghukasyan *et al.*, “Phase Diagram for Twinning Superlattice Te-Doped GaAs Nanowires,” *Nano Lett.*, vol. 22, no. 3, pp. 1345–1349, Feb. 2022, doi: 10.1021/acs.nanolett.1c04680.
- [86] R. E. Algra *et al.*, “Twinning superlattices in indium phosphide nanowires,” *Nature*, vol. 456, no. 7220, Art. no. 7220, Nov. 2008, doi: 10.1038/nature07570.
- [87] F. M. Ross *et al.*, “Sawtooth Faceting in Silicon Nanowires,” *Phys. Rev. Lett.*, vol. 95, no. 14, p. 146104, Sep. 2005, doi: 10.1103/PhysRevLett.95.146104.
- [88] T. Akiyama *et al.*, “Structural stability and electronic structures of InP nanowires: Role of surface dangling bonds on nanowire facets,” *Phys. Rev. B*, vol. 73, no. 23, p. 235308, Jun. 2006, doi: 10.1103/PhysRevB.73.235308.
- [89] M. Rosini *et al.*, “Surface Effects on the Atomic and Electronic Structure of Unpassivated GaAs Nanowires,” *ACS Nano*, vol. 4, no. 10, pp. 6021–6031, Oct. 2010, doi: 10.1021/nn1015488.
- [90] E. Bellet-Amalric *et al.*, “Controlling the shape of a tapered nanowire: lessons from the Burton-Cabrera-Frank model,” *Nanotechnology*, vol. 31, no. 27, p. 274004, Apr. 2020, doi: 10.1088/1361-6528/ab849e.

- [91] V. G. Dubrovskii, “Theory of diffusion-induced selective area growth of III-V nanostructures,” *Phys. Rev. Mater.*, vol. 7, no. 2, p. 026001, Feb. 2023, doi: 10.1103/PhysRevMaterials.7.026001.
- [92] M. R. Lorenz *et al.*, “Band Gap of Gallium Phosphide from 0 to 900 K and Light Emission from Diodes at High Temperatures,” *Phys. Rev.*, vol. 171, no. 3, pp. 876–881, Jul. 1968, doi: 10.1103/PhysRev.171.876.
- [93] A. De *et al.*, “Predicted band structures of III-V semiconductors in the wurtzite phase,” *Phys. Rev. B*, vol. 81, no. 15, p. 155210, Apr. 2010, doi: 10.1103/PhysRevB.81.155210.
- [94] B. C. da Silva *et al.*, “Optical Absorption Exhibits Pseudo-Direct Band Gap of Wurtzite Gallium Phosphide,” *Sci Rep*, vol. 10, no. 1, Art. no. 1, May 2020, doi: 10.1038/s41598-020-64809-4.
- [95] S. Assali *et al.*, “Direct Band Gap Wurtzite Gallium Phosphide Nanowires,” *Nano Lett.*, vol. 13, no. 4, pp. 1559–1563, Apr. 2013, doi: 10.1021/nl304723c.
- [96] B. C. da Silva *et al.*, “Wurtzite Gallium Phosphide via Chemical Beam Epitaxy: Impurity-Related Luminescence vs Growth Conditions,” *ACS Omega*, vol. 7, no. 48, pp. 44199–44206, Dec. 2022, doi: 10.1021/acsomega.2c05666.
- [97] D. Gupta *et al.*, “Stacking defects in GaP nanowires: Electronic structure and optical properties,” *Journal of Applied Physics*, vol. 126, no. 8, p. 084306, Aug. 2019, doi: 10.1063/1.5110039.
- [98] P. J. Dean *et al.*, “The optical properties of Be, Mg and Zn-diffused gallium phosphide,” *Journal of Luminescence*, vol. 4, no. 3, pp. 201–230, Nov. 1971, doi: 10.1016/0022-2313(71)90073-1.
- [99] P. J. Dean *et al.*, “Optical Properties of Excitons Bound to Neutral Acceptors in GaP,” *Phys. Rev. B*, vol. 4, no. 6, pp. 1926–1944, Sep. 1971, doi: 10.1103/PhysRevB.4.1926.
- [100] D. G. Thomas *et al.*, “Bound Excitons in GaP,” *Phys. Rev.*, vol. 131, no. 6, pp. 2397–2404, Sep. 1963, doi: 10.1103/PhysRev.131.2397.
- [101] R. Sauer *et al.*, “Multiple bound excitons in GaP,” *Phys. Rev. B*, vol. 19, no. 12, pp. 6502–6512, Jun. 1979, doi: 10.1103/PhysRevB.19.6502.
- [102] W. T. Masselink *et al.*, “Theory of the Exciton Bound to an Isoelectronic Trap in GaP,” *Phys. Rev. Lett.*, vol. 51, no. 6, pp. 509–512, Aug. 1983, doi: 10.1103/PhysRevLett.51.509.
- [103] H. W. Seo *et al.*, “Nitrogen-doped gallium phosphide nanobelts,” *Applied Physics Letters*, vol. 82, no. 21, pp. 3752–3754, May 2003, doi: 10.1063/1.1578521.
- [104] H. W. Seo *et al.*, “Nitrogen-doped gallium phosphide nanowires,” *Chemical Physics Letters*, vol. 378, no. 3, pp. 420–424, Sep. 2003, doi: 10.1016/j.cplett.2003.07.004.
- [105] A. Belabbes *et al.*, “Electronic bands of III-V semiconductor polytypes and their alignment,” *Phys. Rev. B*, vol. 86, no. 7, p. 075208, Aug. 2012, doi: 10.1103/PhysRevB.86.075208.
- [106] F. Bechstedt *et al.*, “Structure, energetics, and electronic states of III–V compound polytypes,” *J. Phys.: Condens. Matter*, vol. 25, no. 27, p. 273201, Jun. 2013, doi: 10.1088/0953-8984/25/27/273201.

- [107] P. J. Dean, “Absorption and Luminescence of Excitons at Neutral Donors in Gallium Phosphide,” *Phys. Rev.*, vol. 157, no. 3, pp. 655–667, May 1967, doi: 10.1103/PhysRev.157.655.
- [108] B. Gil *et al.*, “Model calculation of nitrogen properties in III-IV compounds,” *Phys. Rev. B*, vol. 33, no. 4, pp. 2701–2712, Feb. 1986, doi: 10.1103/PhysRevB.33.2701.
- [109] A. A. Kopylov *et al.*, “Shallow impurity states and the free exciton binding energy in gallium phosphide,” *Solid State Communications*, vol. 26, no. 11, pp. 735–740, Jun. 1978, doi: 10.1016/0038-1098(78)90731-7.

Appendix A: Structural Characterization Data

High resolution transmission electron microscopy (HRTEM) was used to study the crystal structure of the Te-doped GaP nanowires (NWs). We studied several NWs to verify the crystal structure, as presented in our model. Figure A.1a-d show consecutively higher magnification images of a typical NW. The polytypic regions are identifiable as dark bands in the low magnification TEM images (Figure A.1a, b) as a result of diffraction contrast. Figure A.1d demonstrates the transition from WZ to mixed WZ/ZB at the onset of a polytypic region. The transition from WZ to mixed WZ/ZB is evident by studying HRTEM images wherein the atomic stacking sequence can be assessed. It is well known that WZ has a two-layer (ABAB...) stacking sequence while ZB has a three-layer (ABCABC...) stacking sequence where A, B, and C represent one bilayer (one III-V atomic pair).

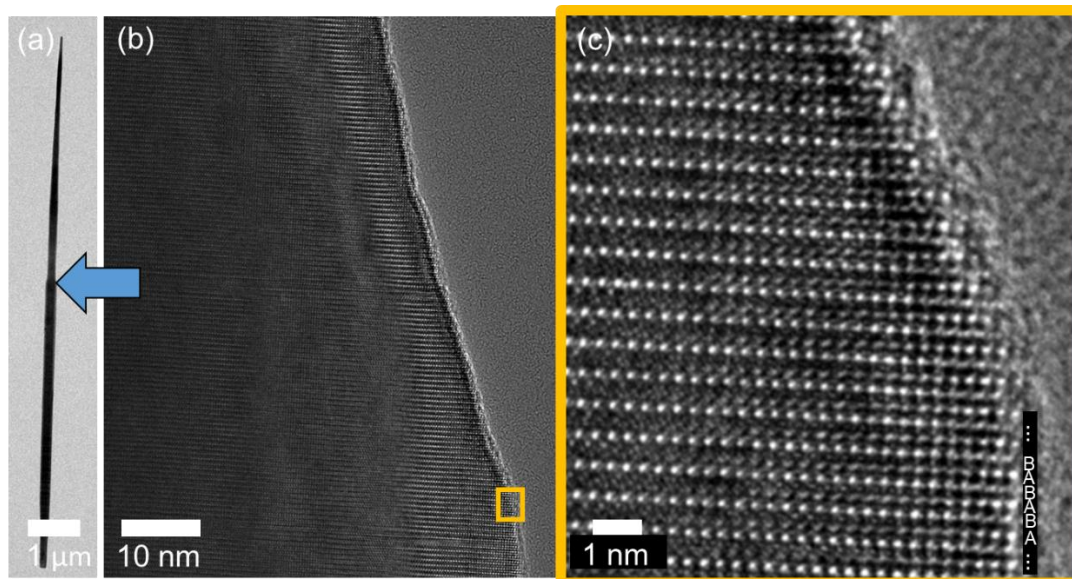


Figure A.2: High resolution transmission electron microscope images (300 kV) showing the wurtzite (WZ) structure at the transition region at progressively higher magnification at the indicated positions. (a) A typical nanowire with abrupt tapering. (b) The transition region is characterized by rapid diameter tapering. (c) The WZ (AB stacking) is evident. Bright spots indicate the positions of the atomic columns.

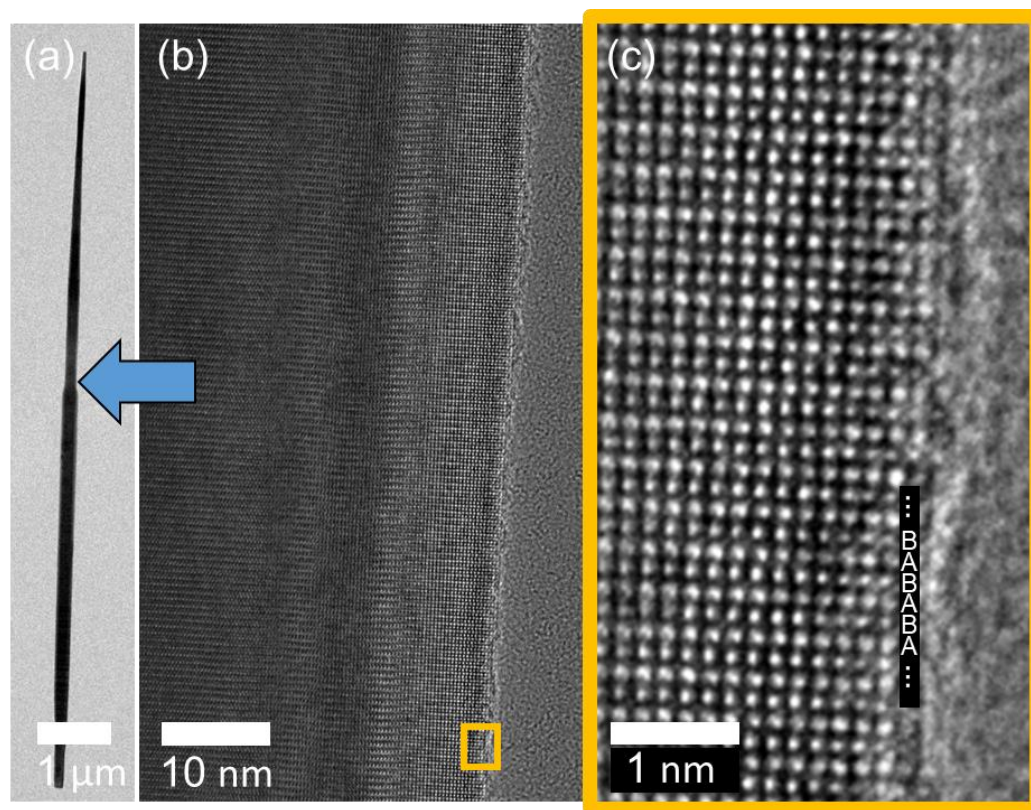


Figure A.3: High resolution transmission electron microscope images (300 kV) showing the wurtzite (WZ) structure after the transition region at progressively higher magnification at the indicated positions. (a) A typical nanowire with abrupt tapering. (b) The WZ (AB stacking), as evident in (c). Bright spots indicate the positions of the atomic columns.

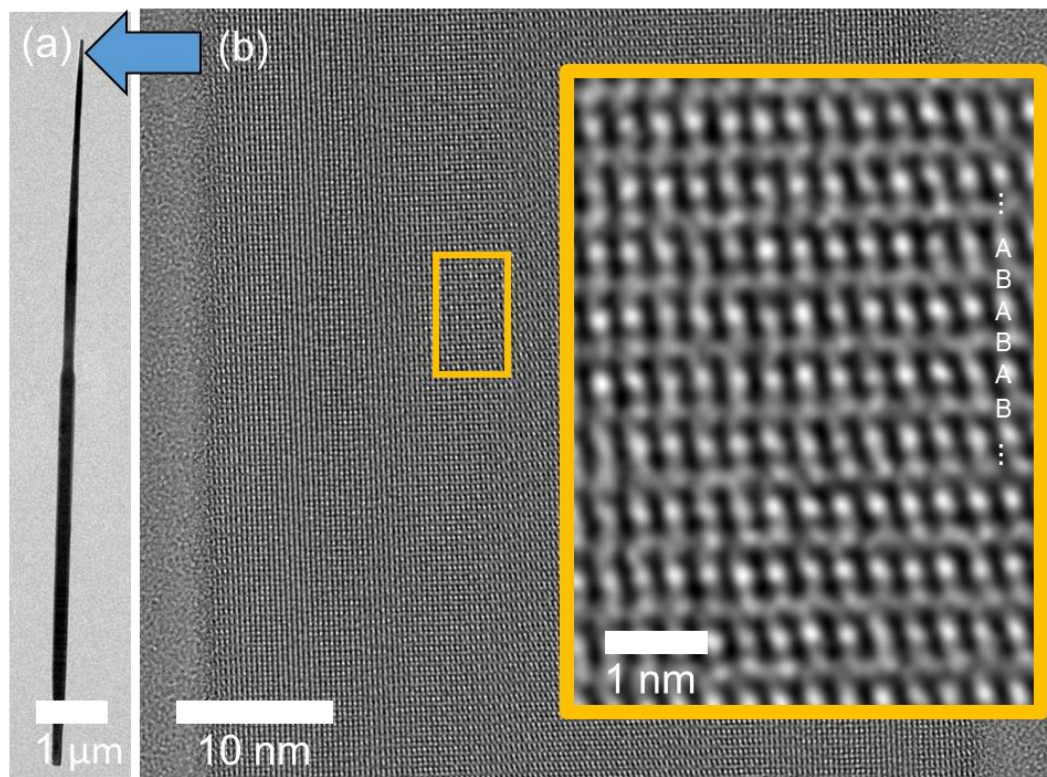


Figure A.5: High resolution transmission electron microscope images (300 kV) showing the wurtzite (WZ) structure near the tip at progressively higher magnification at the indicated positions. (a) A typical nanowire with abrupt tapering. (b) The WZ (AB stacking), as evident in the inset. Bright spots indicate the positions of the atomic columns.

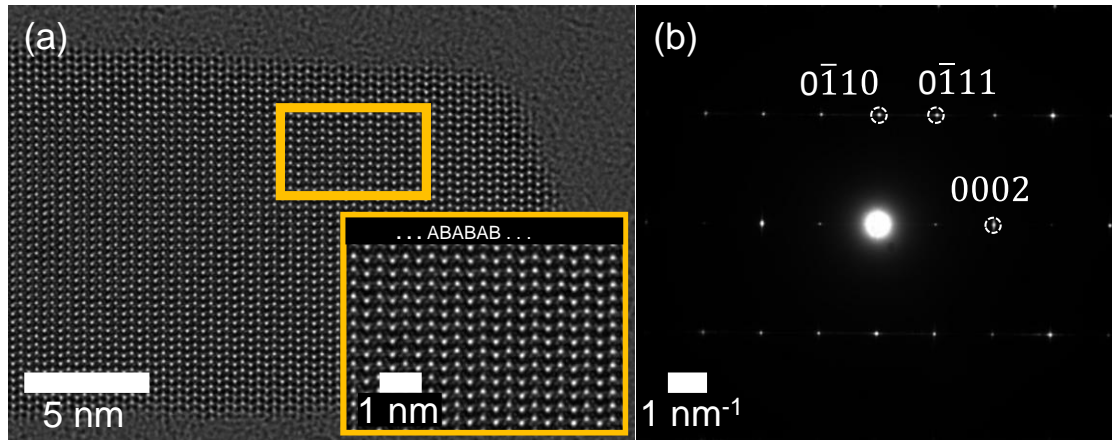


Figure A.6: Structural characterization of a nanowire (NW) tip. (a) High resolution transmission electron microscope image (300 kV) showing the wurtzite (WZ) structure at the tip. Bright spots indicate the positions of atomic columns. The inset shows the AB stacking sequence more clearly. (b) Selective area electron diffraction pattern of the NW tip indicating the WZ structure.

Our model also explains the origin of observed diameter oscillations along the Te-doped segment of the GaP NWs. Quantitative measurements of a NW diameter were conducted directly from TEM images using the pixel counting tool in Inkscape. Repetitive diameter measurements were made along the length of each assessed NW. Figure A.7 shows the two NWs (NW1 and NW2) analyzed for our model. The polytypic regions were found to correspond to a localized increase in the NW diameter. The diameter is defined as the width of the NW projection perpendicular to the growth direction in the TEM images. Since the planar defects appear perpendicular to the growth direction, it was convenient to align the pixel measurement tool parallel to the visible defects. The edges of the NW were determined by locating brighter pixels corresponding to the carbon grid.

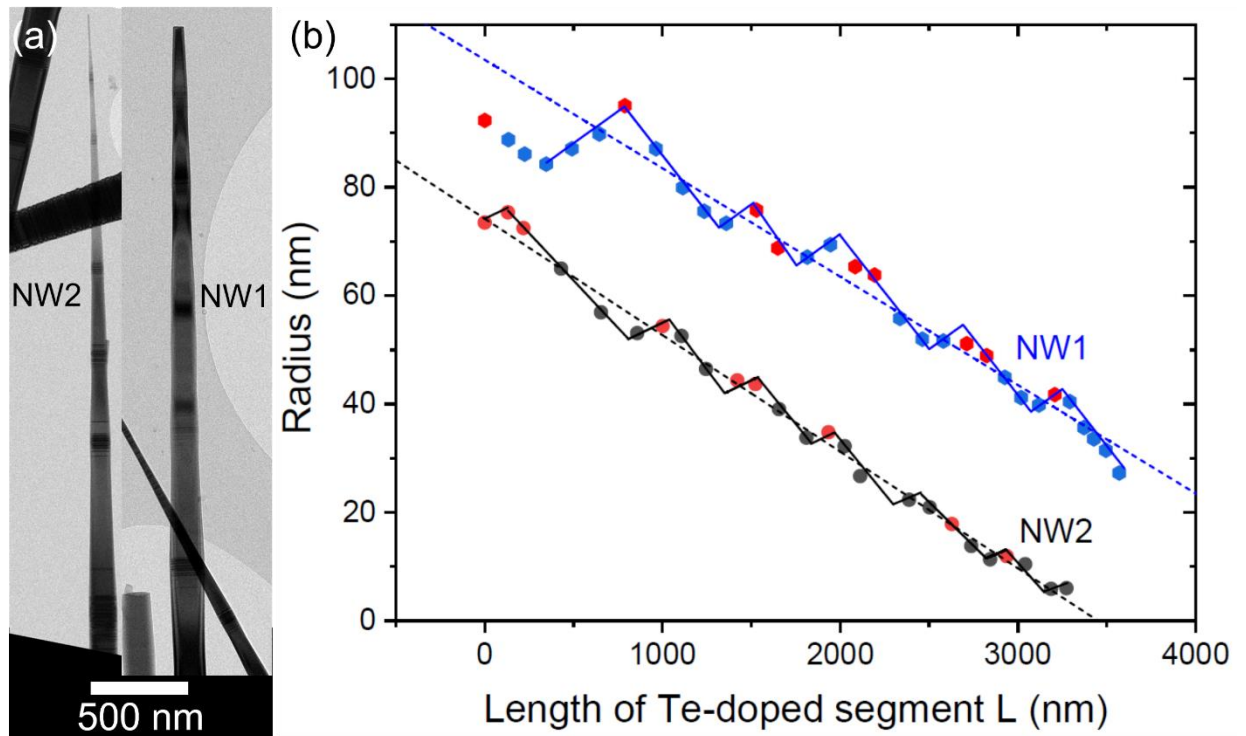


Figure A.7: Mapping nanowire (NW) diameter oscillations. (a) Bright field transmission electron microscope image (120 kV) of two NWs selected for the study of the diameter oscillations. (b) Corresponding measured NW diameters versus the length of Te-doped segments (symbols), with the polytypic wurtzite (WZ)/zincblende (ZB) regions highlighted in red. The orientation of the NWs causes the polytypic regions to show up as dark bands in the bright field image.